Department of Physics and Astronomy

Heidelberg University

Master thesis

in Physics

submitted by

Paula Feltes

born in Cologne

2022

Electron Spin Resonance Spectroscopy on Quasi-One-Dimensional Quantum Spin Systems

This Master thesis has been carried out by Paula Feltes

at the

Kirchhoff Institute for Physics

under the supervision of

Prof. Dr. Rüdiger Klingeler

Elektronenspinresonanz-Spektroskopie an quasi-eindimensionalen Quantenspinketten

Die magnetischen Eigenschaften der Spinsysteme $Sr_2Ni(SeO_3)_2Cl_2$ und $PbCuSeO_4(OH)_2$ mit quasi-eindimensionalen magnetischen Wechselwirkungen wurden mittels Messungen der Elektronenspinresonanz (ESR) und der Magnetisierung untersucht. Die statische Suszeptibilität der Ni^{2+}-Verbindung ($S = 1$) zeigt einen Phasenübergang zu antiferromagnetischer Ordnung bei $T_N = 6\,\mathrm{K}$. In der geordneten Phase wird ein Spin-Flop Übergang bei $B_{\mathrm{SF}} = 8.4\,\mathrm{T}$ in der isothermen Magnetisierung beobachtet. Hochfrequenz-ESR Untersuchungen lassen sich durch ein Zwei-Untergitter Modell eines Antiferromagneten beschreiben. Der daraus gewonnene Parameter $\alpha = 1 - \chi_{\parallel}/\chi_{\perp} \approx 0.39(4)$ deutet auf ausgeprägte thermische bzw. Quantenfluktuationen hin. Die Resonanzsignale im Frequenz-Magnetfelddiagramm lassen sich durch uniaxiale Anisotropie mit Einzelionenanisotropie $D = 3.8(1)\,\mathrm{K}$, Nullfeldaufspaltung $\Delta = 272(2)\,\mathrm{GHz}$ und Landé-Faktor $g = 2.10(1)$ beschreiben. Auch orthorhombische Anisotropie mit $D = 5.10(4)\,\mathrm{K}$, $E = 0.55(4)\,\mathrm{K}$, zwei Nullfeldaufspaltungen $\Delta_1 = 258(3)\,\mathrm{GHz}$, $\Delta_2 = 286(4)\,\mathrm{GHz}$ und $g = 2.07(1)$ beschreiben die Resonanzzweige gut. Statische Suszeptibilitätsmessungen der Cu^{2+}-Verbindung ($S = 1/2$) zeigen zwei Phasenübergänge $T_{N1} = 4.3\,\mathrm{K}$ und $T_{N2} = 4.8\,\mathrm{K}$. X-Band ESR Messungen liefern Spektren mit sehr großen Linienbreiten ($\Delta B \approx 0.4\,\mathrm{T}$), die keine kritische Verbreiterung nahe der Ordnungstemperatur aufweisen. Die Spektren können bei niedrigen Temperaturen mit $g \approx 2.02$ durch die Ableitung einer einzelnen Lorentz Kurve beschrieben werden, entwickeln aber oberhalb von $130\,\mathrm{K}$ mit $g \approx 3.2$ eine zweite Absorptionslinie.

Electron Spin Resonance Spectroscopy on Quasi-One-Dimensional Quantum Spin Chains

The magnetic properties of the spin systems $Sr_2Ni(SeO_3)_2Cl_2$ and $PbCuSeO_4(OH)_2$ with quasi-one-dimensional magnetic interactions were investigated by electron spin resonance (ESR) and magnetisation measurements. The static susceptibility of the Ni^{2+} compound ($S = 1$) shows a phase transition to antiferromagnetic order at $T_N = 6\,\mathrm{K}$. In the ordered phase, a spin-flop transition is observed at $B_{\mathrm{SF}} = 8.4\,\mathrm{T}$ in the isothermal magnetisation. High-frequency ESR studies can be interpreted by means of a two-sublattice model of an antiferromagnet. The obtained parameter $\alpha = 1 - \chi_{\parallel}/\chi_{\perp} \approx 0.39(4)$ indicates pronounced thermal or quantum fluctuations. The resonance signals in the frequency vs. magnetic field diagram can be described by uniaxial anisotropy with single-ion anisotropy $D = 3.8(1)\,\mathrm{K}$, zero-field splitting (ZFS) $\Delta = 272(2)\,\mathrm{GHz}$ and Landé factor $g = 2.10(1)$. Orthorhombic anisotropy with $D = 5.10(4)\,\mathrm{K}$, $E = 0.55(4)\,\mathrm{K}$, two ZFS $\Delta_1 = 258(3)\,\mathrm{GHz}$, $\Delta_2 = 286(4)\,\mathrm{GHz}$ and $g = 2.07(1)$ also describes the resonance branches well. Static susceptibility measurements of the Cu^{2+} compound ($S = 1/2$) feature two phase transitions at $T_{N1} = 4.3\,\mathrm{K}$ and $T_{N2} = 4.8\,\mathrm{K}$. X-band ESR spectroscopy reveals spectra with very broad linewidths ($\Delta B \approx 0.4\,\mathrm{T}$) that do not show critical broadening near the ordering temperature. At low temperatures, the spectra can be described by the derivative of a single Lorentz curve with $g \approx 2.02$, but a second absorption peak develops above $130\,\mathrm{K}$ with $g \approx 3.2$.

Contents

1 Introduction **3**

2 Theoretical Background **5**
2.1 Magnetic Moment of an Electron 5
2.2 Ground State of an Ion 5
2.3 Crystal Field Theory 6
2.3.1 Orbital Quenching 8
2.4 Electron Spin Resonance 8
2.4.1 Effective Hamiltonian 9
2.4.2 Resonance Condition 11
2.5 Magnetic Order and Antiferromagnetism 12
2.5.1 Magnetic Susceptibility and Magnetisation 12
2.5.2 Antiferromagnetic Resonances 14

3 Measurement Technique **17**
3.1 Vibrating Sample Magnetometer 17
3.1.1 Sample Preparation 17
3.2 High-Frequency Electron Spin Resonance 17
3.2.1 Sample Preparation 19
3.3 X-Band Electron Spin Resonance 19
3.3.1 Sample Preparation 20

4 Antiferromagnetic $S = 1$ Chain $Sr_2Ni(SeO_3)_2Cl_2$ **21**
4.1 Crystal Structure 21
4.2 Static Magnetic Susceptibility and Isothermal Magnetisation 23
4.3 High-Frequency Electron Spin Resonance 26
4.3.1 Frequency Dependence 26
4.3.2 Analysis of the Frequency vs. Field Diagram 29
4.3.3 Theoretically Predicted Frequency vs. Field Diagram 39
4.3.4 Discussion of the Frequency vs. Field Diagram 41
4.3.5 Temperature Dependence 43

5 Antiferromagnetic $S = \frac{1}{2}$ Chain $PbCuSeO_4(OH)_2$ **47**
5.1 Crystal Structure 47
5.2 Magnetic Properties 49
5.3 X-Band ESR Measurements and Analysis 51

6 Summary **63**

A Appendix **67**
A.1 Analysis of HF-ESR Data of $Sr_2Ni(SeO_3)_2Cl_2$ by means of an Anisotropic g-factor 67

B Bibliography **71**

1 Introduction

Quasi-low-dimensionality in magnetic compounds refers to systems in which the interactions between magnetic ions are restricted to less than three dimensions. In such systems the magnetic coupling strength between magnetic moments along certain crystallographic directions is much stronger compared to others and thus the dimensionality is effectively reduced. Quasi-low-dimensional systems may be of two-dimensional, one-dimensional or zero-dimensional nature thereby forming layers, chains or point-like magnets and quantum magnets [1]. Focussing on spin chains, the system can be treated as one-dimensional if the intrachain interaction J is three to four orders of magnitudes stronger than the interchain interaction $J^{'}$ [2]. Low-dimensionality together with a low spin number, i.e. $S = 1/2$ or $S = 1$, enhances quantum effects and long-range order (LRO) is suppressed by strong quantum fluctuations [3].

Low-dimensional quantum materials with interacting magnetic ions have attracted the interest of various scientific communities because novel ground states, such as the Bose-Einstein condensate [4], superfluidity [5] and quantum spin liquids [6], which do not occur in three-dimensional systems, can emerge. Theorists predicted many new phenomena, some of which have been verified experimentally. In 1983, for example, Haldane studied one-dimensional Heisenberg chains in which the spins are not restricted to a certain orientation but can point in any direction. Nearest neighbouring (NN) spins are coupled via antiferromagnetic (AFM) interactions, meaning that they prefer an antiparallel alignment. Haldane predicted that chains with integer spin feature an energy gap between the ground state and the first excited state, the so-called Haldane gap, while half-integer spin chains are not gapped [7]. His research was awarded with the Nobel prize in 2016 together with Kosterlitz and Thouless [8]. The Haldane conjecture was first experimentally confirmed in NENP [9], a nickel based $S = 1$ spin chain similar to the compound investigated in chapter 4. The spin chain examined in this thesis does not belong to the Haldane phase but it is attributed to a phase called XY AFM [10], bordering the Haldane phase. Compounds assigned to this phase develop AFM long range order in the xy-plane.

While quantum fluctuations are particularly pronounced in low-dimensional systems, thereby suppressing the tendency towards LRO, ordering can also be suppressed by competing interactions that cannot be simultaneously satisfied, which leads to magnetic frustration in the system [11]. In a spin chain this may be realised by two competing exchange interactions: a ferromagnetic (FM) coupling J_1 between NN ions which prefer a parallel alignment and an AFM coupling J_2 between next-nearest neighbours (NNN) which tends to align spins antiparallel [1]. If $|J_1| \sim |J_2|$,

the two competing couplings cannot be satisfied simultaneously and the system is frustrated [12]. Such a behaviour is demonstrated by the natural single crystal linarite $PbCuSO_4(OH)_2$ [13, 14]. The compound $PbCuSeO_4(OH)_2$ studied in this thesis (c.f. chapter 5) has a similar structure as linarite with sulfur ions replaced by selenium ions and is expected to exhibit a similar frustration.

Elementary spin excitations in magnetic materials are spin waves whose quanta are called magnons. In electron spin resonance (ESR) spectroscopy magnons with wave vector $\vec{q} = 0$ can be detected. The associated resonance branches are called antiferromagnetic resonance (AFMR) modes in case of an AFM ordered system and ferromagnetic resonance (FMR) modes if the examined compound orders ferromagnetically [15]. The resonance frequency vs. field diagram obtained from measured spectra summarises the magnetic field dependence of the magnon modes and provides information on, for example the magnetic anisotropy, the g-factor and the spin configuration in the investigated compound. Here, particular focus is placed on the magnetic anisotropy which is a crucial property to classify the ground state of the system [16].

This thesis is structured as follows: An overview of the theoretical concepts to understand electron spin resonance of antiferromagnetically ordered systems is given in chapter 2. Moreover, the experimental techniques used to investigate the samples are introduced in chapter 3: This includes vibrating sample magnetometry as well as X-band and high frequency electron spin resonance. The experimental results of the two investigated spin chains are presented in chapters 4 and 5. In chapter 4 the integer spin ($S = 1$) chain $Sr_2Ni(SeO_3)_2Cl_2$ is discussed. Starting with the crystal structure and magnetic properties obtained from susceptibility and magnetisation measurements, the discussion proceeds with analysing the frequency vs. field diagram obtained from HF-ESR spectra by comparing three different models. Furthermore, the temperature dependence of HF-ESR data is presented. In the following (chapter 5), the half-integer spin ($S = 1/2$) chain $PbCuSeO_4(OH)_2$ is introduced by presenting its crystal structure and susceptibility measurements. Additionally, the correction of the X-band ESR spectra is described and the temperature dependence of these spectra is analysed and discussed. Finally, chapter 6 provides a summary of this thesis.

2 Theoretical Background

In this chapter an overview of the theoretical background which is required to understand the results discussed in chapter 4 and chapter 5 is provided. The focus is placed on the physical concepts relevant for the investigated samples which show antiferromagnetic behaviour. Further information can be found in e.g. [17, 18, 19] on which this chapter is based.

2.1 Magnetic Moment of an Electron

An electron has an intrinsic spin angular momentum $\vec{S}$ which induces the magnetic moment

$$\vec{\mu}_S = -g_S \mu_B \frac{\vec{S}}{\hbar} \tag{2.1}$$

where μ_B is the Bohr magneton and $g_S = 2$ if quantum electrodynamic corrections are neglected. In an atom, electrons bound to the nucleus have an additional magnetic moment which is proportional to the orbital angular momentum $\vec{L}$

$$\vec{\mu}_L = -g_L \mu_B \frac{\vec{L}}{\hbar} \tag{2.2}$$

with $g_L = 1$. The orbital and spin angular momentum are coupled weakly via the spin-orbit interaction. This results in the magnetic moment

$$\vec{\mu}_J = -g_J \mu_B \frac{\vec{J}}{\hbar} \tag{2.3}$$

where g_J is the Landé-factor and the total angular momentum is defined as $\vec{J} = \vec{L} + \vec{S}$. The absolute value is quantised and can take values between $|L - S|$ and $|L + S|$.

2.2 Ground State of an Ion

Electrons in an ion fill the atomic shells according to the aufbau principle. Completely filled shells have no unpaired electrons which results in $S = L = 0$. In only partly filled shells the electrons can combine to give non-zero S and L. To find the

combination of S and L that minimises the energy, Hund's rules can be applied. They are empirical rules which are listed in order of decreasing importance [20]:

- Hund's first rule: States with maximum total spin S respecting the Pauli principle have the lowest energy
- Hund's second rule: The energy is minimised by maximising the total orbital angular momentum L which is permitted by the first rule
- Hund's third rule: The total angular momentum J takes values depending on the filling of the shells with

$$J = \begin{cases} |L - S| & \text{if the shell is less than half-filled} \\ L + S & \text{if the shell is more than half-filled.} \end{cases} \tag{2.4}$$

The third rule works well for rare earth ions but it does not hold for transition metal ions [18], such as nickel and copper. This can be explained by crystal field theory which will be introduced in the next section.

2.3 Crystal Field Theory

Magnetic ions in a crystal can be affected by an electric field, the crystal field (CF), arising from its immediate surrounding. The CF depends on the shape of the electronic orbitals of the centering ion and its neighbouring atoms involved in bonds. Moreover, the symmetry of the local environment of the central ion determines the properties of the CF [18]. The magnetic transition metal ions Ni^{2+} and Cu^{2+}, discussed in chapter 4 and chapter 5, respectively, have unpaired electrons in the $3d$-orbital. They form a covalent bond with p-orbitals of oxygen and chlorine ions. Depending on the orientation of the d- and p-orbitals with respect to each other, the energy levels occupied by the electrons change because overlapping orbitals increase the electrostatic repulsion between the bonding electrons [18]. Figure 2.1 shows the splitting of energy levels for a $3d$-ion in different environments. A free ion, as shown in fig. 2.1 (a), is spherically symmetric and the five energy levels are degenerate. In an octahedral crystal field with cubic symmetry (c.f. fig. 2.1 (b)), the energy levels split up into the t_{2g}- and e_g-levels, separated by the energy difference Δ. This leads to the single-ion anisotropies $D = E = 0$, meaning that there is no preferential orientation for the spin [17]. For a distorted octahedron the symmetry becomes tetragonal and the energy levels split up even further. One has to distinguish between two different cases: 1) The octahedron can be distorted in a way that one axis is longer than the other two axes. This can be reached by uniaxial elongation or biaxial compression and is shown in fig. 2.1 (c). The resulting anisotropy is of uniaxial nature with the single-ion anisotropies $D > 0$ and $E = 0$. The spins align preferentially along a certain axis, the so-called easy axis, which can be observed as two absorption signals in an electron spin resonance measurement [17]. 2) An octahedron with three differently sized axes demonstrates orthorhombic anisotropy with single-ion anisotropies

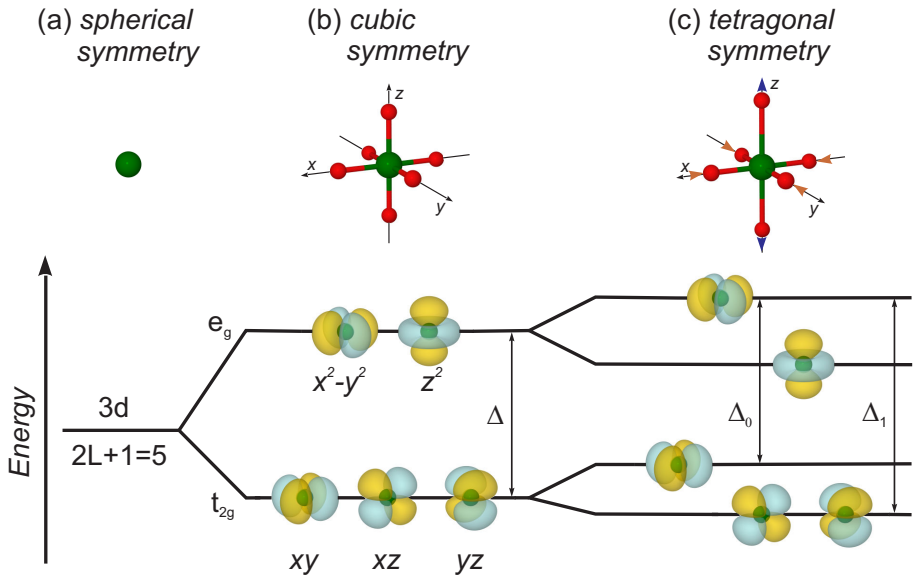


Figure 2.1: Energy level splitting of the respective orbitals of 3*d*-ions for different crystal field symmetries. (a) A free ion with spherical symmetry demonstrates five degenerate states. (b) Cubic symmetry in an octahedron splits the energy levels into the t_{2g}- and e_g-orbitals. (c) A distortion of the octahedron yields tetragonal symmetry with further splitting of the energy levels. Figure is taken from [13].

$D, E > 0$. There is the easy axis (energetically favoured), the second-easy axis and the hard axis. Spins aligned parallel to the hard axis increase the energy of the system. ESR spectroscopy reflects the anisotropy as three absorption peaks at different magnetic field strengths at the same frequency [17]. The appearance of several resonance features will be explained in more detail in section 2.4.2.

The filling of the orbitals depends on the strength of the CF compared to the pairing energy which is defined as the Coulomb energy cost of putting two electrons in the same orbital. In the weak-field case, the CF energy is lower than the pairing energy. The electrons will first occupy each orbital singly before orbitals become doubly occupied [18]. This is shown as an example for Ni^{2+} in fig. 2.2. The eight electrons in the 3*d*-shell fill the energetically lower t_{2g}-levels completely while the energetically

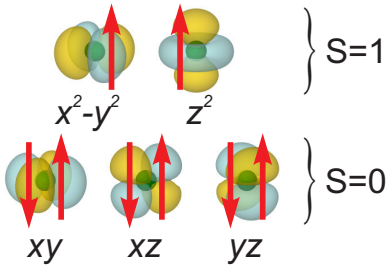


Figure 2.2: Electron configuration of Ni^{2+} in an octahedral crystal field with cubic symmetry. Figure is taken from [13].

higher e_g-levels have two unpaired electrons resulting in a total spin $S = 1$. Cu^{2+} has one additional electron in the $3d$-shell which leads to one unpaired electron in the e_g-level and to a total spin $S = 1/2$. In the strong-field case with $E_{\mathrm{CF}} > E_{\mathrm{pairing}}$, electrons will doubly occupy the lower t_{2g}-orbitals before filling the e_g-orbitals at higher energy [18].

2.3.1 Orbital Quenching

The expected magnetic ground state for the discussed transition metal ions are

Ion	Shell	S	L	J
Ni^{2+}	$3d^8$	1	3	4
Cu^{2+}	$3d^9$	1/2	2	5/2

following Hund's rules. Experiments have shown that the predicted value for the effective magnetic moment

$$\mu_{eff} = g_J \mu_B \sqrt{J(J+1)} \tag{2.5}$$

is not correct because the CF interaction is much stronger than the spin-orbit interaction for $3d$-ions. This implies that Hund's third rule cannot be applied as it is based on the assumption that the spin-orbit interaction is the predominant energy term after the Coulomb energy. In fact, $3d$-ions have a ground state with $L = 0$ so that $J = S$ and the orbital is said to be quenched [18].

2.4 Electron Spin Resonance

Electron spin resonance (ESR) is a widely used spectroscopy technique that probes the magnetic moment of electrons via resonant absorption of electromagnetic radiation in the microwave regime. During a measurement, microwaves at fixed frequency irradiate the investigated material while the external magnetic field is swept at a constant rate. Transitions between different electronic energy levels can be excited which is observed as an absorption peak in the detected spectrum. From the observed transitions, information about the magnetic anisotropy, the g-factor and the zero-field splitting (ZFS) of the material can be gained.

One distinguishes between X-band ESR at low frequencies between 9 and 10 GHz and high-frequency electron spin resonance (HF-ESR) where microwaves from 40 GHz to 1 THz can be accessed. Furthermore, HF-ESR is operated at higher external magnetic fields than X-band ESR. The advantage of X-band ESR devices is the application of a cavity resonator, possible due to the fixed operating frequency, which

increases the signal to noise ratio of the recorded spectra. For some materials the limited frequency range prevents one from finding absorption peaks because zero-field splittings can be on the order of 100 GHz and a HF-ESR setup is required. Moreover, an anisotropic g-factor can be better resolved by HF-ESR because the energy difference between g_x, g_y and g_z grows with the external magnetic field and microwave frequency [21].

2.4.1 Effective Hamiltonian

The interactions in a spin system, which are relevant for an ESR experiment, can be described by the effective Hamiltonian

$$\mathcal{H} = \mathcal{H}_{EZI} + \mathcal{H}_{CFI} + \mathcal{H}_{EEI} \tag{2.6}$$

with the electronic Zeeman interaction $\mathcal{H}_{EZI}$, the crystal field interaction $\mathcal{H}_{CFI}$ and the electron-electron interaction $\mathcal{H}_{EEI}$. These interactions will be discussed in the following. Nuclear Zeeman interaction, quadrupolar interactions and hyperfine coupling are not considered in eq. (2.6) because these interactions can be neglected in the compounds investigated within this work.

Zeeman Interaction

The Zeeman effect describes the coupling of a magnetic moment $\vec{\mu}$ to an external magnetic field $\vec{B}$. This coupling can split the energy levels of states which are degenerate at zero magnetic field. In ESR experiments, the energy difference between two levels for which transitions are allowed is limited by the microwave frequency and the strength of the applied field. Therefore, energy levels with only a small degeneracy at zero magnetic field are relevant. This is taken into account by introducing an effective spin $\vec{S}_{eff}$ such that the energy levels have a $(2S_{eff}+1)$-fold degeneracy and the electronic Zeeman interaction can be described by the Hamiltonian [17]

$$\mathcal{H}_{EZI} = \mu_B \vec{B} \cdot \mathbf{g}_{eff} \cdot \vec{S}_{eff} \tag{2.7}$$

where $\mathbf{g}_{eff}$ is the effective g-tensor. The label "eff" will be dropped from now on due to notation. Th effective g-tensor is usually symmetric and can be written in diagonal form with the components g_x, g_y and g_z. In this case, the Hamiltonian simplifies to

$$\mathcal{H}_{EZI} = \mu_B(g_x B_x S_x + g_y B_y S_y + g_z B_z S_z). \tag{2.8}$$

Assuming a magnetic field applied along the z-axis, the energy difference between two Zeeman levels is given by [18]

$$\Delta E = g_z \mu_B |\Delta m_s| B_z \tag{2.9}$$

where Δm_s defines the difference between the spin quantum numbers of the Zeeman energy levels.

Crystal Field Interaction

The crystal field interaction arises from an electric field induced by the neighbouring atoms of the magnetic ion, as introduced in section 2.3. It can be treated as a second order perturbation to the Zeeman energy term and reads [22]

$$\begin{aligned}\mathcal{H}_{CFI} &= \vec{S} \cdot \mathbf{D} \cdot \vec{S} \\ &= D_{xx}S_x^2 + D_{yy}S_y^2 + D_{zz}S_z^2. \end{aligned} \tag{2.10}$$

Here, $\mathbf{D}$ is the real, symmetric anisotropy tensor with three orthogonal eigenvectors. The second equality in eq. (2.10) holds because the anisotropy tensor can be transformed to diagonal form by choosing the coordinate axes x, y and z parallel to the eigenvectors. S_x^2, S_y^2 and S_z^2 are the spin operators for the x-, y- and z-direction, respectively. Subtracting a constant does not change the physical properties of the Hamiltonian. Hence, eq. (2.10) can be reduced to [17]

$$\mathcal{H}_{CFI} = DS_z^2 + E\left(S_x^2 - S_y^2\right) \tag{2.11}$$

with uniaxial anisotropy D and rhombic anisotropy E.

Exchange Interaction

The interaction between two electrons with spin $\vec{S}_i$ and $\vec{S}_j$ can be written as [23]

$$\begin{aligned}\mathcal{H}_{SS} &= \vec{S}_i \cdot \mathbf{J}_{ij} \cdot \vec{S}_j \\ &= J_{ij}\vec{S}_i \cdot \vec{S}_j + \vec{S}_i \cdot \mathbf{D}_{ij} \cdot \vec{S}_j + \vec{d}_{ij} \cdot \left(\vec{S}_i \times \vec{S}_j\right) \end{aligned} \tag{2.12}$$

with the interaction strength J_{ij}, the symmetric traceless tensor $\mathbf{D}_{ij}$ and the polar vector $\vec{d}_{ij}$. The first term describes an isotropic spin-spin contribution to the magnetic interaction while the second and third term denote an anisotropic and antisymmetric contribution, respectively. In general, the isotropic part is the dominant coupling and the electron-electron interaction simplifies to

$$\mathcal{H}_{EEI} = J_{ij}\vec{S}_i \cdot \vec{S}_j \tag{2.13}$$

which implies antiferromagnetic coupling for $J_{ij} > 0$ and ferromagnetic coupling for $J_{ij} < 0$.

2.4.2 Resonance Condition

Electron spin resonance occurs when an oscillating magnetic field, perpendicular to the external magnetic field, induces transitions between stationary states of a spin system. Neglecting the crystal field interaction, the energy difference between two states is determined by the Zeeman effect and reads [17]

$$\Delta E = h\nu = g\mu_B B|\Delta m_s| \tag{2.14}$$

with the Planck constant h and the resonance frequency ν. Here, g is a linear combination of the components of the effective g-tensor introduced in eq. (2.7).

The allowed transitions in an ESR experiment are restricted by the selection rules $\Delta S = 0$ and $\Delta m_s = 1$. For a system with $S = 1$ there are three different Zeeman levels corresponding to $m_s = \pm 1$ and $m_s = 0$ and hence two transitions with $\Delta m_s = 1$ are possible. As shown in fig. 2.3 (a) the resonance condition in eq. (2.14), neglecting CF interaction, is fulfilled at the same magnetic field for the two allowed transitions $m_s = -1 \rightarrow m_S = 0$ and $m_s = 0 \rightarrow m_S = 1$. Including the effect of CF interaction with uniaxial anisotropy, c.f. fig. 2.3 (b), the energy of the Zeeman levels is shifted by the zero-field splitting Δ and the transition $m_s = -1 \rightarrow m_S = 0$ occurs at a different magnetic field than the transition $m_s = 0 \rightarrow m_S = 1$. Hence, two absorption peaks can be observed during the experiment. Accounting for the CF interaction becomes more complex for orthorhombic anisotropy with two different ZFS which yields three observable resonance features.

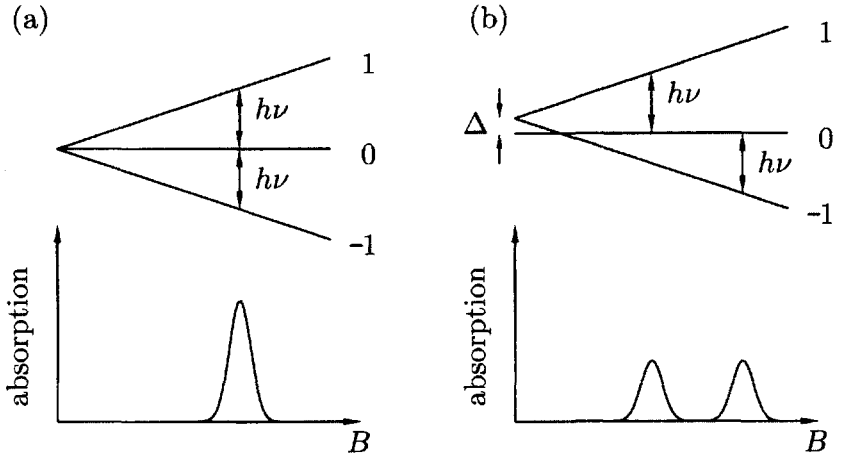


Figure 2.3: ESR transitions for a spin system with $S = 1$ and $m_S \in \{-1, 0, 1\}$, such as Ni^{2+}. CF interaction is neglected in (a) resulting in a single absorption line. Including CF energy in (b), the energy levels of $m_S = -1$ and $m_S = 1$ are raised by the zero-field splitting Δ with respect to the energy state $m_S = 0$. This leads to two distinct ESR lines. Figure is taken from [18].

2.5 Magnetic Order and Antiferromagnetism

Atoms in a paramagnetic material have unpaired electrons which lead to a finite total spin and hence non-zero magnetic moments. These moments point in random directions because the magnetic interaction between neighbouring atoms is weak. Only if an external magnetic field is applied, the magnetic moments align along the direction of the field yielding a finite magnetisation in the material.

If the magnetic interactions between neighbouring ions are strong enough, the system can develop long-range magnetic order. It is ferromagnetic (FM) in the case of parallel aligned moments with a finite magnetisation at zero-field or antiferromagnetic (AFM) if the magnetic moments prefer an antiparallel orientation. Due to the antiparallel alignment the magnetic moments cancel each other, yielding no spontaneous magnetisation without an external field. The investigated compounds in this thesis demonstrate AFM order below the Néel temperature T_N.

2.5.1 Magnetic Susceptibility and Magnetisation

An antiferromagnet can be treated as a system with two sublattices for which the spins within one sublattice all point in the same direction but the different sublattices are oriented in such a way that their total magnetic moments cancel each other. This description allows for a mean-field approach which considers a single spin and replaces the exchange interaction between this spin and its nearest neighbours by an effective interaction. This results in the Curie-Weiss law [24]

$$\chi = \frac{C}{T - \Theta} \tag{2.15}$$

which describes the temperature dependence of the susceptibility of an antiferromagnet well above its ordering temperature T_N. The parameter C is the Curie constant and the Weiss temperature Θ determines the ordering behaviour of the system. For an antiferromagnet $\Theta < 0$, while $\Theta > 0$ implies ferromagnetic correlations. If $\Theta = 0$ the material is paramagnetic. For temperatures below T_N the direction of the external magnetic field is important as shown in fig. 2.4 (a) for an antiferromagnet with uniaxial anisotropy. The spins in a uniaxial AFM favour the orientation along the easy axis. If the magnetic field is applied parallel to this direction, both sublattices are already saturated at $T = 0$. Hence, there is no reorientation of the spins and $\chi_{\parallel} = 0$. Upon increasing the temperature, thermal fluctuations start to play a role and the parallel susceptibility increases until it equals $\chi_{\perp}$ at $T = T_N$. An external field applied perpendicular to the easy axis reorients the spins in such a way that the net magnetisation takes a finite value. This effect is temperature independent. Therefore, the perpendicular susceptibility $\chi_{\perp}$ is constant for $T < T_N$.

A similar anisotropy effect can be observed in the field dependence of the magnetisation. If the field is applied perpendicular to the easy axis, the sublattice magneti-

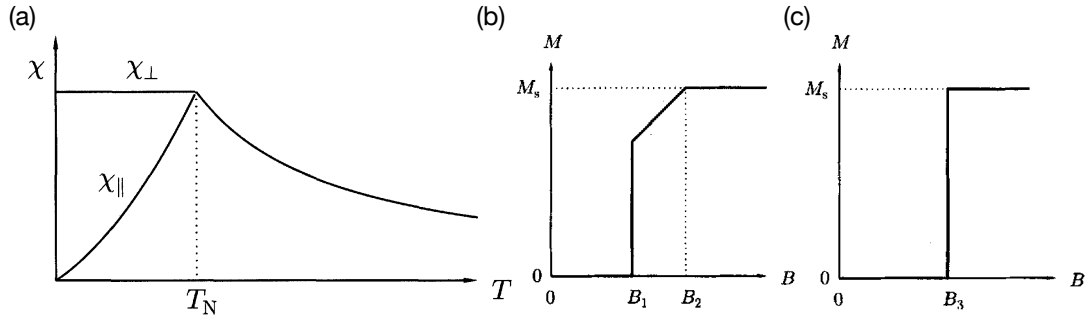


Figure 2.4: (a): Magnetic susceptibility χ of an antiferromagnet with uniaxial anisotropy. Below the ordering temperature T_N, the susceptibility for fields applied parallel to the easy axis $\chi_\parallel$ decreases upon cooling whereas the susceptibility for fields applied perpendicular to the easy axis $\chi_\perp$ is temperature independent. (b) and (c): Magnetisation of an uniaxial AFM as a function of a magnetic field applied parallel to the easy axis. A system with small anisotropy energy (b) experiences a spin-flop transition at B_1 before the saturation magnetisation is reached at B_2. In an antiferromagnet with strong anisotropy effect (c) a spin-flip transition occurs. Figures taken from [18].

sations tilt in the direction of the external field until all magnetic moments point in the same direction as the magnetic field. The magnetisation is saturated. For an external field parallel to the easy axis, two different cases have to be distinguished. The first one, shown in fig. 2.4 (b), features a small anisotropy energy. The magnetic moments remain in AFM order until the applied field equals the spin-flop (SF) field B_1. A transition from the AFM phase to the SF phase occurs and results in a jump in the magnetisation. The spin configurations of the respective phases are shown in fig. 2.5. Above B_1 the magnetisation increases continuously until it reaches its saturation value at B_2. The second case holds for systems with a strong preference of the spin orientation in easy axis direction. Instead of a spin-flop transition, a spin-flip transition occurs at B_3. As shown in fig. 2.4, the magnetisation is instantaneously saturated because the magnetisation of one sublattice suddenly reverses.

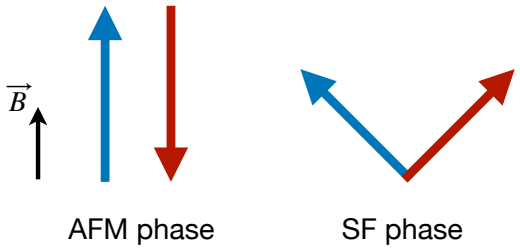


Figure 2.5: Spin configuration in the antiferromagnetic (AFM) and spin-flop (SF) phase. Figure adapted from [15].

2.5.2 Antiferromagnetic Resonances

Elementary spin excitations in magnetic materials are spin waves whose quanta are called magnons. In an antiferromagnetic system with two sublattice magnetisations of the same magnitude but oriented opposite to each other, mean-field theory predicts a uniform precession of the two sublattice magnetisations about an external magnetic field. The precession frequency equals the Larmor frequency

$$\vec{\nu}_L = -\frac{\gamma}{2\pi}\vec{B} \tag{2.16}$$

and resonance phenomena occur if an oscillation magnetic field equalling the Larmor frequency is applied perpendicular to the static field. The resonance frequencies depend on the strength as well as the direction of the applied magnetic field as can be seen from eq. (2.16). They can be obtained from the effective Hamiltonian [25]

$$\mathcal{H} = -g\mu_B \sum_i \left(\vec{B}\cdot\vec{S}_i + J\vec{S}_i\cdot\vec{S}_{i+1} - D\,(S_i^z)^2 - E\{(S_i^x)^2 - (S_i^y)^2\}\right) \tag{2.17}$$

with the uniform nearest neighbour interaction strength J, the axial anisotropy D and the transverse anisotropy E. For $D > 0$ and $E = 0$ the Hamiltonian describes a system with uniaxial anisotropy which prefers the alignment of spins along the z-axis, the easy axis. A magnet with orthorhombic anisotropy satisfies $D > E > 0$. As in the uniaxial case, the spins favour an orientation parallel to the z-axis. The x-direction corresponds to the second-easy axis whereas spins aligned parallel to the y-axis, the hard axis, increase the energy of the system. This convention is used for the following parts of this thesis.

Applying mean-field approximation, the free energy F of the system reads [25]

$$\begin{aligned} F = A\vec{M}_1\cdot\vec{M}_2 - (\vec{M}_1+\vec{M}_2)\cdot\vec{B} + K\left\{(M_1^z)^2 + (M_2^z)^2\right\} \\ + L\left\{(M_1^x)^2 + (M_2^x)^2 - (M_1^y)^2 - (M_2^y)^2\right\} \end{aligned} \tag{2.18}$$

where $\vec{M}_1$ and $\vec{M}_2$ are the sublattice magnetisations. The parameters A, K and L are proportional to J, D and E, respectively, where the exact proportionality can be found in [25].

The resonance frequencies are derived by solving the Landau-Lifshitz equation [15]

$$\frac{\mathrm{d}\vec{M}_{1,2}}{\mathrm{d}t} = \gamma\vec{M}_{1,2}\times\vec{H}_{eff1,2} \tag{2.19}$$

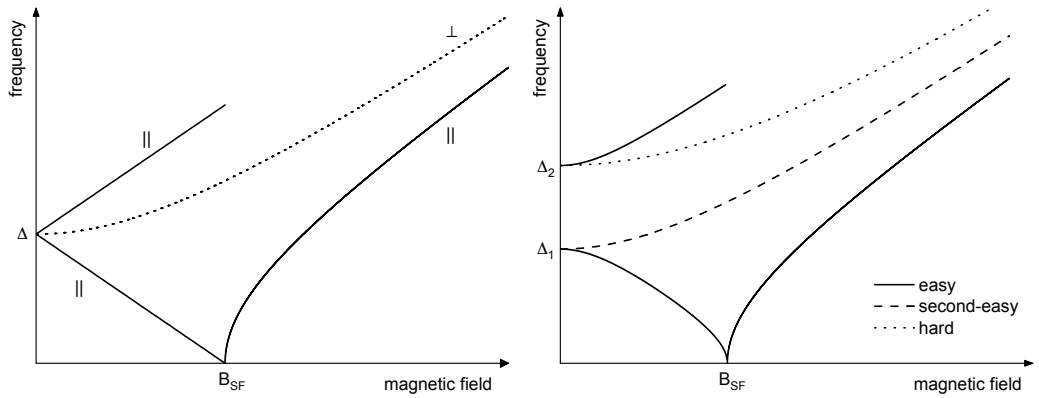
where γ is the gyromagnetic ratio and the effective fields acting on the sublattice magnetisations $\vec{M}_{1,2} = \hat{z}\,M_{1,2z} + (\hat{x}\,m_{1,2x} + \hat{y}\,m_{1,2y})\,\exp(\mathrm{i}\omega t)$ are given by [25]

$$\vec{H}_{eff_{1,2}} = \frac{\partial F}{\partial\vec{M}_{1,2}}. \tag{2.20}$$

The solutions are obtained by numerical computations and can be found for example in [15] for uniaxial anisotropy and [26] for orthorhombic anisotropy. They are given in chapter 4 and will not be written explicitly in this chapter. Instead, the field dependence of the resonance frequencies is described qualitatively by means of frequency vs. field diagrams shown in fig. 2.6.

For uniaxial anisotropy in (a) there is one zero-field splitting Δ where three resonance branches merge into a common signal. The solid branches with linear field dependence correspond to resonances in the AF phase for fields $B < B_{\mathrm{SF}}$ and parallel to the easy axis. At $B = B_{\mathrm{SF}}$ a transition to the spin-flop phase occurs and only one resonance mode for parallel fields is observed. The dotted branch depicts the resonance mode for a magnetic field applied perpendicular to the easy axis. It has two-fold degeneracy since both axes perpendicular to the easy axis are equivalent.

A material with orthorhombic anisotropy, shown in (b), features two ZFS at Δ_1 and Δ_2. The resonance branches in the AF phase for $B < B_{\mathrm{SF}}$ and parallel to the easy axis (solid lines) do not show a linear field dependence and are gapped by the energy $\Delta_2 - \Delta_1$. As in the uniaxial case, a transition to the spin-flop phase occurs at $B = B_{\mathrm{SF}}$ and only one resonance mode for parallel fields is observed. There are two distinct branches for magnetic fields perpendicular to the easy axis. The dashed branch corresponds to fields parallel to the second-easy axis with ZFS Δ_1, whereas the dotted line depicts magnetic fields parallel to the hard axis with ZFS Δ_2.



(a) Uniaxial anisotropy (b) Orthorhombic anisotropy

Figure 2.6: Field dependence of the predicted resonance branches in materials with uniaxial and orthorhombic anisotropy.

3 Measurement Technique

In this chapter the measurement techniques and experimental devices used throughout this thesis are introduced. This includes a vibrating sample magnetometer (VSM), a high-frequency electron spin resonance (HF-ESR) spectrometer and an X-band ESR spectrometer.

3.1 Vibrating Sample Magnetometer

Magnetisation and susceptibility measurements were carried out using a commercial physical property measurement system (PPMS) from *Quantum Design*. Magnetic fields up to 14 T can be applied in the temperature range from 1.8 K to 300 K. The vibrating sample magnetometer (VSM) option is a fast and sensitive DC magnetometer. The sample is being oscillated near a pickup coil while the induced voltage is detected synchronously. The system provides a high resolution of magnetisation changes due to a large oscillation amplitude and oscillation frequency.

3.1.1 Sample Preparation

Loose powder of $Sr_2Ni(SeO_3)_2Cl_2$ was filled inside a non-magnetic sample container. This capsule consists of a cylindric part in which the sample is filled and a stamp which is used to press the sample into the capsule and seal it. This preparation makes an additional fixing by eicosane unnecessary. The prepared capsule was mounted onto a brass holder which was attached to the end of a sample rod.

3.2 High-Frequency Electron Spin Resonance

High-frequency electron spin resonance (HF-ESR) measurements were performed using a home-built spectrometer whose setup is sketched in fig. 3.1. It can operate at frequencies ranging from 30 GHz to 1 THz with an external magnetic field applied between 0 and 16 T.

The microwaves are transmitted from a microwave vector network analyser (MVNA) via the harmonic generator (HG) and circular waveguides to the sample which is positioned in the centre of the applied magnetic field. After transmitting the sample, the radiation is reflected by two gold plated mirrors at the bottom of the sample rod

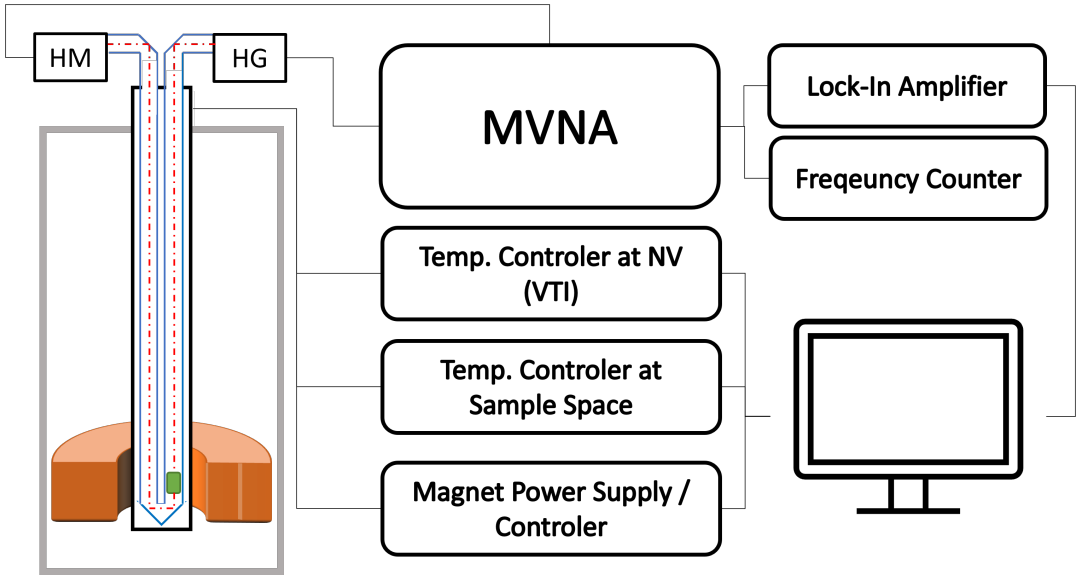


Figure 3.1: Schematic measurement setup of the HF-ESR spectrometer. A superconducting magnet (orange torus) is located inside a helium cryostat. The sample (green), positioned in the center of the external magnetic field, is inside circular waveguides (blue lines) which are surrounded by a vacuum jacket in order to maintain a constant temperature in the sample space. The red lines depict the pathway of the microwave radiation generated by the MVNA. More detailed explanation is provided in the text. The figure is taken from [27].

and propagates through the harmonic mixer (HM) and back to the MVNA where the amplitude and phase of the microwave signal are detected.

The phase sensitive MVNA from *AB millimètre* generates microwave radiation in a frequency range from 8 to 18 GHz. This fundamental frequency is multiplied by assembling different Schottky diodes at HG and HM to reach the above mentioned measurement frequencies. The MVNA is connected to an EIP 575B source locking microwave counter from *Phase Matrix* in order to stabilise the measurement frequency. Additionally, it is connected to a SR 830 DSP Lock-In Amplifier by *Stanford Research Systems* which amplifies the microwave signal and detects it.

The external magnetic field is generated by a commercial superconducting magnet provided by *Oxford Instruments*. It is placed inside a cryostat which is filled with liquid helium to cool the magnet. A helium flow from the cryostat into the sample space is operated via a needle valve. In order to obtain a reliable temperature control of the sample temperature, one thermometer and heater pair (*Oxford Instruments*) is placed at the needle valve as part of a variable temperature insert (VTI). Another thermometer and heater pair (*LakeShore*) is located close to the sample.

A desktop PC connected to all control units as well as the Lock-In Amplifier allows to observe and adjust the temperature and records the transmitted signal as a function of the external applied field.

3.2.1 Sample Preparation

Fixed powder of $Sr_2Ni(SeO_3)_2Cl_2$ in form of a pressed pellet was placed inside a brass ring. The bottom of the ring was covered with microwave transparent capton tape which does not contribute to the ESR signal. Four pieces of pressed pellet were fixed onto the bottom layer of kapton tape. In order to increase the absorption signal, the area of the ring that was not covered by the sample was masked by commercial aluminium foil (see fig. 3.2). To seal the brass ring, a second layer of kapton tape was applied on top of it.

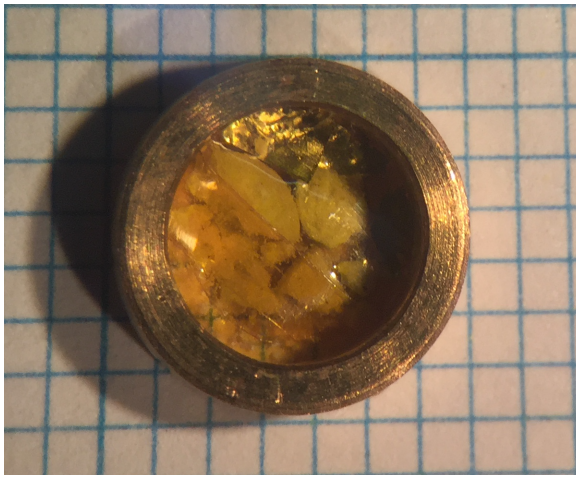


Figure 3.2: Probe ring with four pieces of pressed pellet of $Sr_2Ni(SeO_2)_2Cl_3$ and aluminium foil in the area not covered by the sample.

3.3 X-Band Electron Spin Resonance

X-band ESR spectroscopy was performed with a commercial *BRUKER ELEXSYS E500* X-band spectrometer at the Institute for Inorganic Chemistry Heidelberg. The setup works at a fixed microwave frequency of $f = 9.6\,\mathrm{GHz}$ with applied static magnetic fields up to 1.2 T which are generated by a water cooled electromagnet. Experiments can be performed at temperatures between 4 and 300 K. To reach low temperatures, a *Cryo Edge* cryostat with a compressor system is used. The temperature is controlled manually by means of a *Mercury iTC* by *Oxford Instruments*. Due to the fixed operating frequency, the coupling between the microwaves and the sample can be increased by application of a high sensitivity ER 4122SHQE continuous wave (CW) cavity resonator. Moreover, a small oscillating field is superimposed on the external static field. Therefore, the first derivative of the transmitted microwave signal is recorded instead of the direct signal. These modifications result in a high resolution and allow a precise investigation of the recorded spectra.

3.3.1 Sample Preparation

The powder sample of $PbCuSeO_4(OH)_2$ was prepared in a quartz glass tube by *Sigma Aldrich* and fixed with eicosane to prevent reorientation of crystallites during the measurement. The quartz tube was filled with argon gas and sealed with parafilm to avoid magnetic signals from oxygen molecules.

4 Antiferromagnetic $S = 1$ Chain $Sr_2Ni(SeO_3)_2Cl_2$

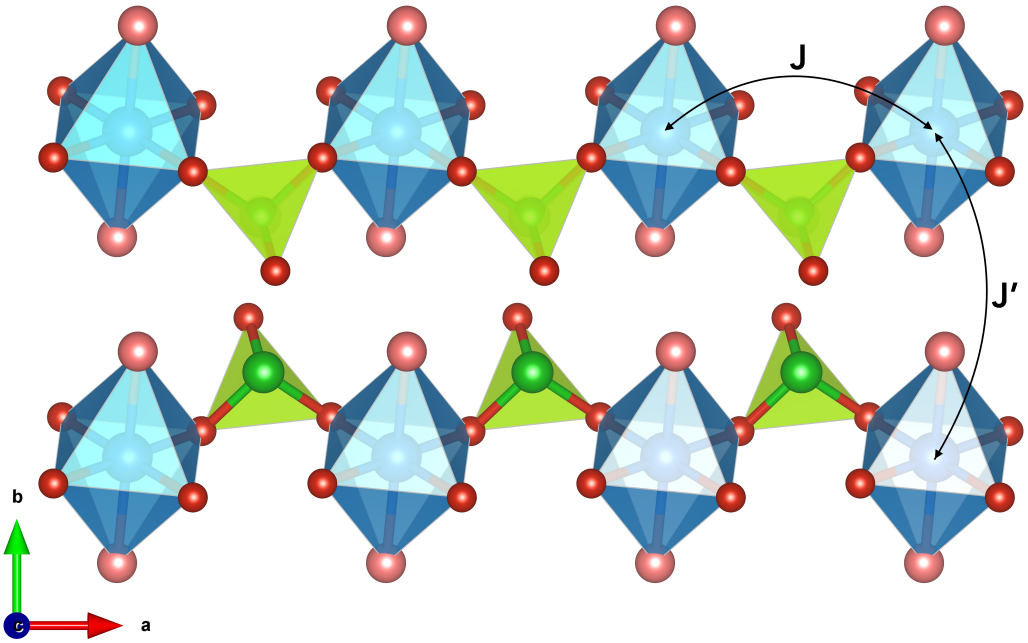
Strontium nickel selenite chloride, $Sr_2Ni(SeO_3)_2Cl_2$, is a uniform spin $S = 1$ chain system which has been placed in the easy-plane antiferromagnetic (XY-AFM) long-range ordered sector of the Sakai-Takahashi phase diagram [10]. This phase diagram classifies the quantum ground state of magnetic compounds depending on their strength of exchange interaction and axial anisotropy. $Sr_2Ni(SeO_3)_2Cl_2$ is the first compound to be assigned to the XY-AFM phase of the diagram, making it an interesting candidate for further experimental studies to gain deeper insight into the physics of this phase [10].

Measurements of the static magnetic susceptibility and specific heat reveal the evolution of long-range antiferromagnetic order below the Néel temperature $T_N = 6\,\mathrm{K}$ [10]. $Sr_2Ni(SeO_3)_2Cl_2$ was interpreted to demonstrate axial anisotropy $D = 4.86\,\mathrm{K}$ along the z-direction and transverse anisotropy $E = 0.60\,\mathrm{K}$ in the xy-plane [10]. The aim of this chapter is to probe this interpretation of orthorhombic anisotropy by means of high frequency ESR spectroscopy.

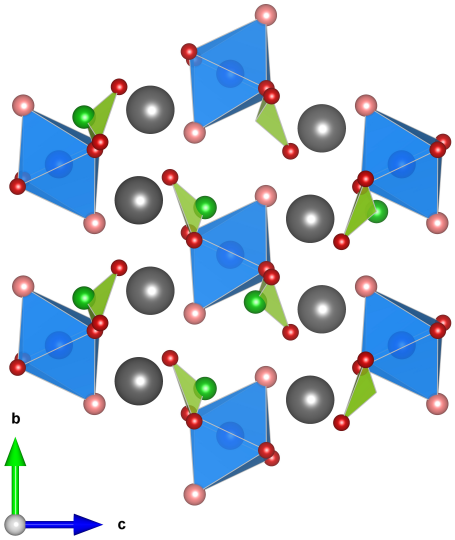
4.1 Crystal Structure

The magnetic ions of $Sr_2Ni(SeO_3)_2Cl_2$ are nickel ions in the oxidation state 2+ with ground state electron configuration $[Ar]3d^8$, resulting in spin $S = 1$ based on Hund's rules [28]. The angular momentum of Ni^{2+} is quenched to $L = 0$ and therefore the total angular momentum is given by $J = |L \pm S| = 1$. The compound crystallises in a monoclinic structure of space group $P2_1/n$ with $\beta = 92.53°$. The lattice constants are given as $a = 5.325\,\text{Å}$, $b = 6.436\,\text{Å}$ and $c = 12.197\,\text{Å}$. The crystal structure is displayed in fig. 4.1 with structural data taken from [10]. The Ni^{2+} ions are arranged in the centers of slightly tetragonally distorted octahedra shown in fig. 4.1 (a). The octahedra are formed by four oxygen ions (red) in the same plane as Ni ions and two chlorine ions (pink). The height $h = 4.890\,\text{Å}$ of the octahedra covers the distance Cl-Ni-Cl yielding $d_h = 2.445\,\text{Å}$ between Ni and Cl ions. The distances between Ni and O ions read $d_1 = 2.071\,\text{Å}$ and $d_2 = 2.057\,\text{Å}$. To be more specific, d_1 and d_2 do not differ much whereas d_h is about 19 % larger than d_2 and anisotropy in the g-factor is expected.

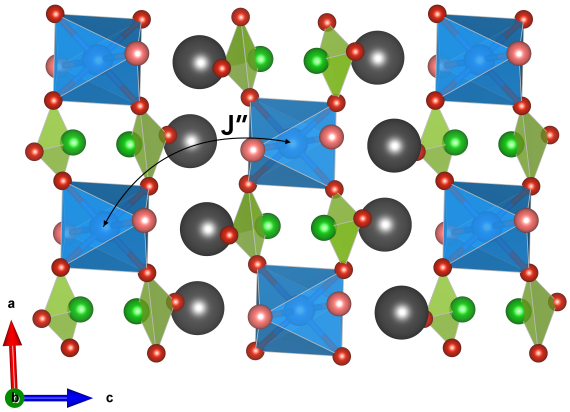
The octahedra are connected by SeO_3 pyramids, yielding spin $S = 1$ chains with antiferromagnetic intrachain exchange interaction $J = 9.75\,\mathrm{K}$ in a-direction. The



(a) Ni chains form along the a-axis with antiferromagnetic intrachain exchange interaction J mediated by SeO_3 pyramids. The interchain exchange interaction $J^{'}$ in b-direction is much weaker than J [10]. Explicit values are given in the text.



(b) View on the bc-plane emphasises the quasi one-dimensional structure of magnetic interactions in a-direction. Ferromagnetic interaction $J^{''}$ can be neglected compared to J [10].



(c) View on the ac-plane clarifies that the left- and right-tilted octahedra belong to distinct but equivalent spin chains.

Figure 4.1: Crystal structure of $Sr_2Ni(SeO_3)_2Cl_2$ in three different orientations. Nickel ions are represented by blue spheres in the center of octahedra. The octahedra are formed by four oxygen ions (red) and two chlorine ions (pink). Selenium ions (green) mediate magnetic interaction between the Ni ions along the a-axis. Strontium ions are coloured in dark grey. Crystallographic data taken from [10] and visualised with *VESTA* [29].

interchain exchange interaction $J^{'} = 0.8\,\mathrm{K}$ along the b-axis is much weaker than J. The exchange interaction $J^{''} = -0.35\,\mathrm{K}$ in the bc-plane (see fig. 4.1 (b)) is ferromagnetic and can be neglected compared to J. All exchange interaction parameters were estimated by DFT+U calculations in [10]. They confirm the quasi-1D structure of the magnetic interactions in $Sr_2Ni(SeO_3)_2Cl_2$. The quasi-1D structure is also highlighted in fig. 4.1 (b) which shows the bc-plane of the crystal structure. It is clearly visible that the magnetic-interaction-mediating SeO_3 pyramids do not connect the Ni^{2+} ions in b- or c-direction but only along the a-axis. Additionally, the view on the bc-plane reveals that the octahedra are tilted by 31.42° with respect to the b-axis in different orientations. Together with fig. 4.1 (c) it is clarified that the left- and right-tilted octahedra belong to distinct spin chains with equivalent magnetic exchange in a-direction.

4.2 Static Magnetic Susceptibility and Isothermal Magnetisation

The following measurements to characterise the magnetic properties of the compound were carried out on powder sample with a commercial Quantum Design PPMS using the vibrating sample magnetometer (VSM) option at fields ranging from 0 to 13.7 T. The aim of these measurements was to verify the ordering temperature $T_N = 6\,\mathrm{K}$ as well as the spin-flop field $B_{c1} = 9\,\mathrm{T}$ reported in [10].

The static magnetic susceptibility, $\chi = M/B$, measured at external field $B = 1\,\mathrm{T}$ in a temperature range from 2 to 300 K is shown in fig. 4.2 by black circles. It demonstrates a paramagnetic Curie-Weiss-like behaviour for high temperatures and reveals a correlation maximum at $T_{\max} \approx 13\,\mathrm{K}$. The system develops long-range magnetic order at $T_N = 6\,\mathrm{K}$. The phase transition from a disordered to an ordered state is revealed in the Fisher's specific heat $\partial(\chi T)/\partial T$, shown in the inset of fig. 4.2, as a peak at the ordering temperature. Susceptibility measurements published in [10] give similar results.

The temperature dependence of the static susceptibility was fitted to the Curie-Weiss-like law [24]

$$\chi(T) = \frac{C}{T - \Theta} + \chi_0 \tag{4.1}$$

with Curie constant C, Weiss temperature Θ and a temperature-independent term χ_0. The parameters C, Θ and χ_0 depend strongly on the chosen fit range of the Curie-Weiss fit. The best results were obtained for fitting the high temperature data between 200 and 275 K. The fit was not performed up to 300 K because of limited data quality at high temperatures. The quality of the susceptibility data and the reliability of the Curie-Weiss fit could be improved by measuring up to 400 K by means of the more sensitive SQUID magnetometer of the magnetic property measurement

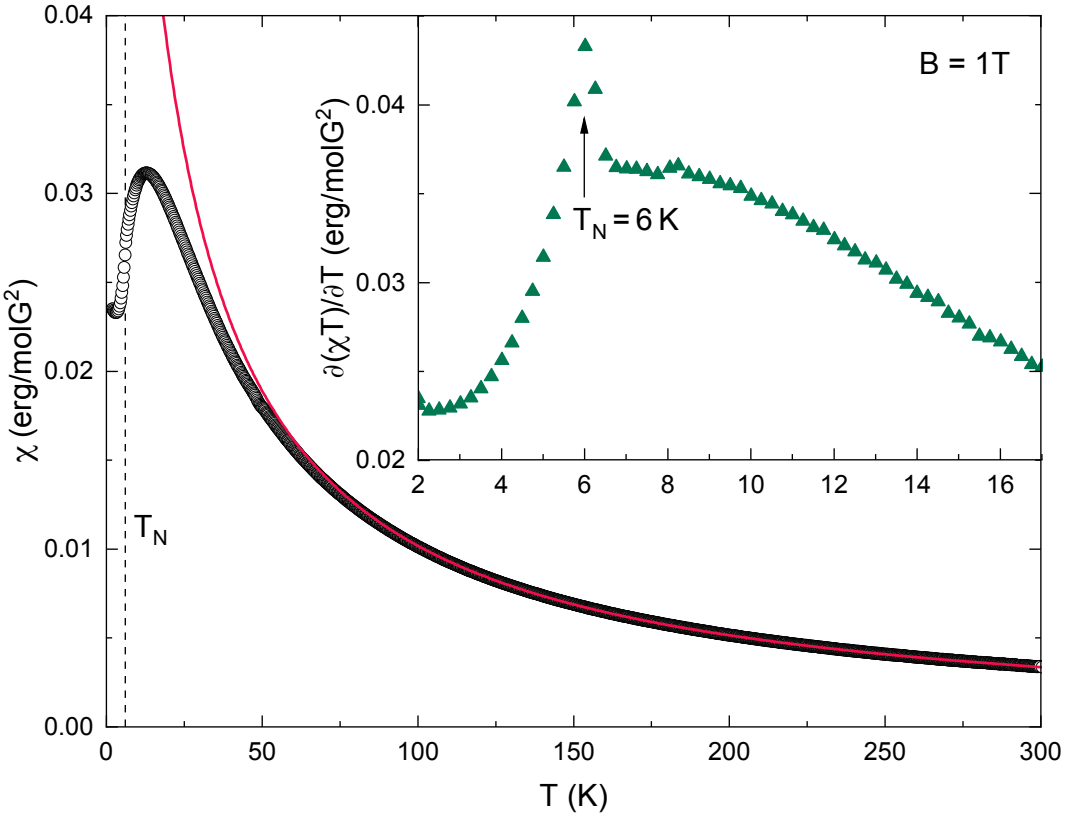


Figure 4.2: Temperature dependence of the static magnetic susceptibility $\chi = M/B$ (black circles) and Fisher's specific heat $\partial(\chi T)/\partial T$ (green triangles) for $Sr_2Ni(SeO_3)_2Cl_2$ measured at 1 T. The solid red line shows the Curie-Weiss fit based on eq. (4.1).

system (MPMS) by Quantum Design. It was refrained from doing that since the ordering temperature of the compound agrees with $T_N = 6\,\mathrm{K}$ reported in [10] and the verification of the ordering temperature was the goal of this measurement.

The Curie constant is determined as $C = 1.174(9)\,\mathrm{ergK/(molG^2)}$. It can be related to the effective magnetic moment of the Ni^{2+} ions μ_{eff} and their g-factor by [24]

$$C = \frac{N_A \mu_{eff}^2}{3k_B} = \frac{N_A (g\mu_B)^2 J(J+1)}{3k_B} \tag{4.2}$$

with Avogadro and Boltzmann constants N_A and k_B, respectively, and the Bohr magneton μ_B. Assuming a total angular momentum number $J = |L \pm S| = 1$ (quenched orbital momentum $L = 0$ and $S = 1$ for Ni^{2+} ions), yields the g-factor $g_{\mathrm{Curie}} = 2.2(1)$. It agrees with typically obtained g-factors for Ni^{2+} in an octahedral crystal field, ranging from $g = 2.15$ to $g = 2.2$ [30] as well as with $g = 2.26(1)$, published for $Sr_2Ni(SeO_3)_2Cl_2$ [10].

The negative Weiss temperature $\Theta = -11(6)\,\mathrm{K}$ implies a predominance of antifer-

romagnetic correlations which, however, are rather weak. At temperatures below $T = 100\,\mathrm{K}$ the Curie-Weiss fit and the static susceptibility start to deviate, implying the onset of short-ranged correlations.

The temperature independent term is determined as $\chi_0 = -4(2) \cdot 10^{-4}\mathrm{erg/molG}^2$ and can be attributed to a diamagnetic contribution, stemming for example from the sample holder and from the constituent ions [31].

The magnetic susceptibility $\mathrm{d}M/\mathrm{d}B$, measured at $T = 2\,\mathrm{K}$ and $T = 3\,\mathrm{K}$, is shown in fig. 4.3. At low fields the magnetic susceptibility decreases to a minimum at approximately 1.5 T after which it increases again. This convex curvature hints at paramagnetic impurities in the sample [10]. The slope of $\mathrm{d}M/\mathrm{d}B$ changes abruptly at the critical field $B_{c1} = 8.4\,\mathrm{T}$, implying a transition to a different phase. This kink is less pronounced at $T = 3\,\mathrm{K}$ but still clearly visible. Measurements at 1.46 K using pulsed magnetic fields up to 45 T, determined this feature at a slightly higher field of 9.0 T [10]. This deviation of 0.6 T might result from the different measurement techniques. Another explanation could be the temperature difference of the two measurements. Even though the magnetisation curves at 2 and 3 K show the same value of the critical field, there might be an effect between 1.46 and 2 K which influ-

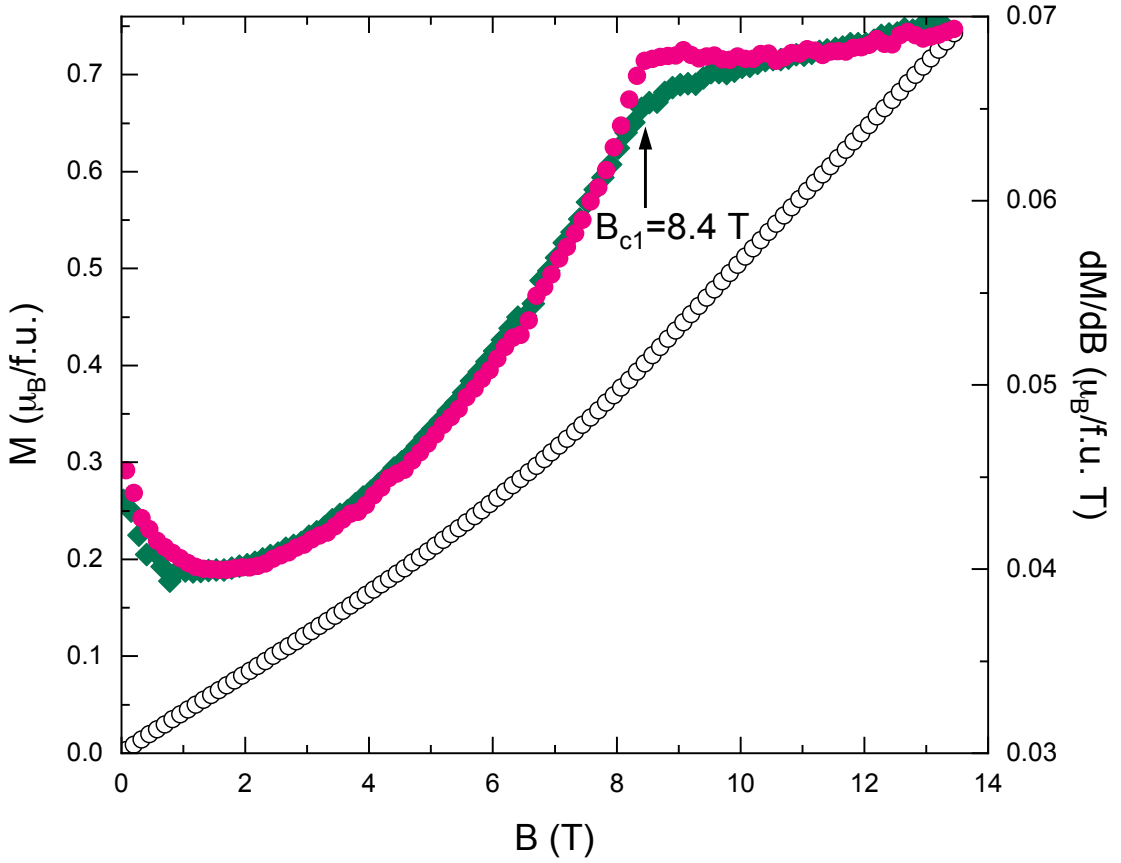


Figure 4.3: Magnetic susceptibility $\mathrm{d}M/\mathrm{d}B$ of $Sr_2Ni(SeO_3)_2Cl_2$ measured in static magnetic field up to 13.7 T at 2 and 3 K.

ences the position of the transition field. A big advantage of pulsed magnetic fields is the possibility to measure at elevated magnetic fields which cannot be accessed with static fields. The pulsed magnetic fields measurement in [10] reveals a second critical field at $B_{c2} = 23.7\,\mathrm{T}$ and the magnetisation saturation at $B_{\mathrm{sat}} = 31.0\,\mathrm{T}$. The critical fields B_{c1} and B_{c2} have been interpreted as the spin-flop and spin-flip field, respectively [10].

4.3 High-Frequency Electron Spin Resonance

HF-ESR measurements were performed on a fixed powder of $Sr_2Ni(SeO_3)_2Cl_2$ in magnetic fields up to 16 T at $T = 2\,\mathrm{K}$. Taking spectra at various fixed frequencies and sweeping over the magnetic field enables to construct the resonance frequency vs. field diagram. Comparing this phase diagram with theoretical predictions for models with various types of anisotropies, allows interpretation of the magnetic structure and anisotropy in the compound under investigation. Moreover, a temperature dependent measurement of resonance spectra at fixed frequency 213.8 GHz between 2 and 120 K provides information about the linewidth and the effective g-factor close to the ordering temperature as well as in the paramagnetic phase.

4.3.1 Frequency Dependence

HF-ESR spectra of $Sr_2Ni(SeO_3)_2Cl_2$ were recorded at fixed frequencies between 40 and 800 GHz while the external magnetic field was swept up to 16 T. Absorption signals were detected between 70 and 500 GHz. Selected spectra are shown in fig. 4.4 for frequencies ranging from 200 to 500 GHz. A background is subtracted from the spectra and they are normalised and offset for better visualisation.

Examining a fixed powder sample allows to detect several absorption features which belong to different antiferromagentic resonance (AFMR) branches. The different branches occur for different angles between the external magnetic field and the crystallographic axes, e.g. for magnetic fields parallel or perpendicular to the easy axis, at the same frequency. The differently coloured dots in fig. 4.4 represent AFMR corresponding to different resonance branches. With increasing frequency, the red dots shift to lower fields while green and blue dots shift to higher fields. The resonance signals are determined by visually reading off the position of the minimum in the recorded spectra or, if the signal is phase mixed, the feature is localised at the field value of the inflection point of the transmission. The different branches were identified by inspecting the frequency vs. field diagram in fig. 4.5.

Depending on the resonance mode, the absorption features show varying intensities. The blue resonances, for example, are rather weak, while the red and green signals demonstrate a large intensity. A noisy spectrum complicates the identification of the weaker signals even more because some resonance features might be hidden under the noise. Moreover, the observed resonance signals have a broad linewidth which

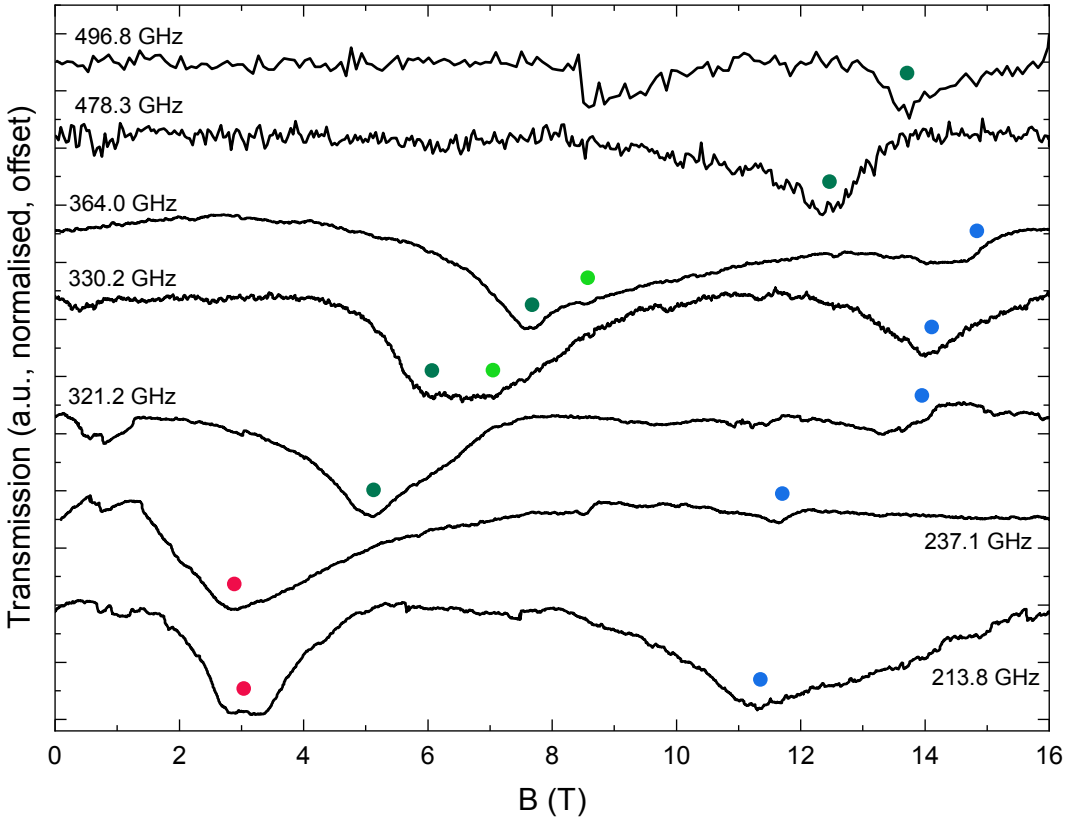


Figure 4.4: Resonance spectra of $Sr_2Ni(SeO_3)_2Cl_2$ obtained in HF-ESR measurements at microwave frequencies between 100 GHz and 500 GHz. Observed resonances are marked by different coloured dots which represent different resonance branches. The different branches were identified by inspecting the frequency vs. field diagram in fig. 4.5.

is typical for powder samples. Especially the spectrum recorded at 330.2 GHz (c.f. fig. 4.4) demonstrates broad absorption features. Those marked by two green dots at around 6 and 7 T provide a good example of the difficulties encountered while interpreting the HF-ESR data: The resonance position is usually determined by reading off the minimum in the recorded spectrum. Here, the minimum cannot be clearly localised because it is more than 1 T broad. It was decided to deal with this by identifying one signal at the beginning and one signal at the end of the minimum, as depicted in fig. 4.4.

The frequency vs. field diagram is constructed by plotting all observed resonance signals in one diagram, which is shown in fig. 4.5. The different colours coincide with the colours used in fig. 4.4. It is striking that resonance features have been detected only for magnetic fields larger than 2 T. The lowest frequency for which resonance signals have been observed is 70 GHz even though measurements have been performed down to 40 GHz.

The small, grey symbols with a linear field dependence and no offset at $B = 0\,\mathrm{T}$

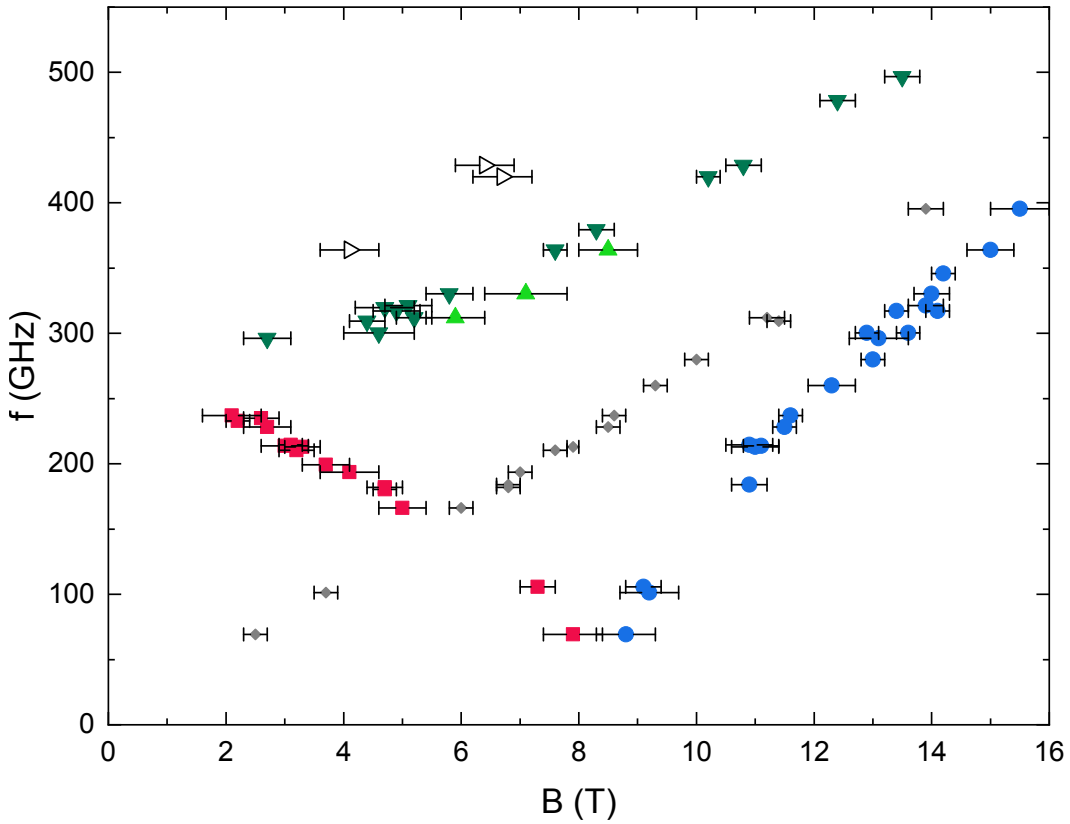


Figure 4.5: Field dependence of observed resonance signals in $Sr_2Ni(SeO_3)_2Cl_2$. HF-ESR measurements were performed in a frequency range between 40 GHz and 800 GHz at 2 K. Different colours correspond to different resonance branches as observed in fig. 4.4.

correspond to a paramagnetic impurity. The resonance branch represented by red data points decreases with increasing magnetic fields. This decrease is approximately linear for $2\,\mathrm{T} < B < 6\,\mathrm{T}$, whereas the resonance frequency drops significantly for $B > 6\,\mathrm{T}$. It approaches another branch (represented in blue) near 8 T suggesting that both branches meet at the spin-flop field B_{SF} at zero frequency. The blue resonance branch is visible for $B > 8\,\mathrm{T}$ and shows increasing resonance frequencies with increasing applied fields. The data points represented by light and dark green triangles are observed for $f > 300\,\mathrm{GHz}$. The corresponding features appear at resonance fields close to each other (compare fig. 4.4). Therefore they are attributed to resonance branches in two different ways. The first interpretation identifies light and dark green signals as resonances in the same branch. The second interpretation attributes the light and dark green absorption features to two individual resonance branches. This is discussed in more detail in section 4.3.2. Three resonance features, shown by empty, black triangles, were detected at frequencies above all other resonance frequencies at the corresponding magnetic field. They were not attributed to a resonance branch and therefore neglected in the fitting process of the observed branches because their signal is very weak.

4.3.2 Analysis of the Frequency vs. Field Diagram

Three different interpretations of the field dependence of antiferromagnetic resonances in $Sr_2Ni(SeO_3)_2Cl_2$ are presented in figs. 4.6 to 4.8. They assume a two-sublattice antiferromagnet with uniaxial anisotropy, orthorhombic anisotropy with $D \approx E$ and orthorhombic anisotropy with $D \gg E$, respectively. D is the axial anisotropy whereas E denotes the transverse anisotropy. Table 4.1 gives an overview of the different magnetic anisotropies assumed and the observed resonance branches corresponding to the theoretically predicted branches for the different models. For clearer distinction, they are named Model 1 for fig. 4.6, Model 2 for fig. 4.7 and Model 3 for fig. 4.8 from now on. The explicit field dependence of the resonance frequencies corresponding to the observed resonance branches stated in table 4.1 as well as the theoretically expected resonance branches is discussed below.

	Magnetic Anisotropy	Observed Branches
Model 1 (fig. 4.6)	Uniaxial, D	f_{AF^-}, f_{SF}, $f_{\perp}$
Model 2 (fig. 4.7)	Orthorhombic, $D \approx E$	f_{AF^-}, f_{SF}, $f_{2^{\mathrm{nd}}\mathrm{easy}}$
Model 3 (fig. 4.8)	Orthorhombic, $D \gg E$	f_{AF^-}, f_{SF}, $f_{2^{\mathrm{nd}}\mathrm{easy}}$, f_{hard}

Table 4.1: Summary of the three models assuming different magnetic anisotropy to interpret the recorded frequency vs. field diagram. The different observed branches correspond to different resonance modes as discussed below.

First of all, the resonance features showing linear field dependence without zero-field splitting, represented by a grey line in figs. 4.6 to 4.8, will be discussed. They can be described by

$$f_{PM}(B) = \frac{\gamma_{PM}}{2\pi} \cdot \frac{g_{PM}\, B}{2} \tag{4.3}$$

for all fits discussed in this section. The prefactor is defined as

$$\frac{\gamma_i}{2\pi} = g_i \cdot 13.996 \frac{\mathrm{GHz}}{\mathrm{T}}. \tag{4.4}$$

These resonance features can be attributed to a paramagnetic (PM) impurity in the sample with $g_{\mathrm{PM}} = 1.98(1)$ and will therefore be omitted in all subsequent discussions, i.e. it will not be explicitly discussed in any of the models.

Model 1: Uniaxial Anisotropy

The experimental data in fig. 4.6 are fitted by a two-sublattice antiferromagnetic mean-field model assuming uniaxial anisotropy in the system. This yields resonance branches in different modes for external fields along the easy axis and perpendicular

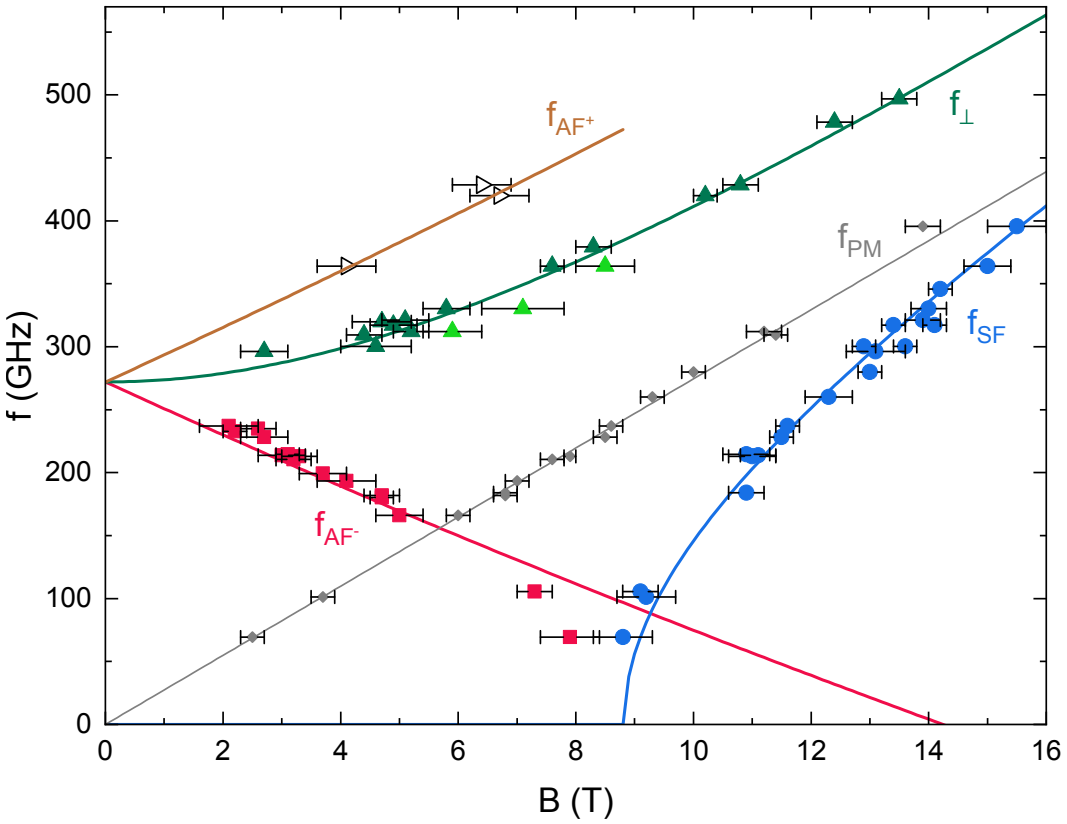


Figure 4.6: Model 1: Frequency vs. field diagram of $Sr_2Ni(SeO_3)_2Cl_2$ constructed from HF-ESR data recorded at $T = 2\,\mathrm{K}$. Assuming a two-sublattice AFM with uniaxial anisotropy, the observed branches are attributed to f_{AF^-}, f_{SF} and $f_\perp$. The branch f_{AF^+} is a theoretical expectation from obtained fit parameters while f_{PM} describes a paramagnetic impurity in the sample.

to it. Their field dependence can be expressed under the assumption of $B_A \ll B_E$ with the exchange field B_E and the anisotropy field B_A. For an external field B parallel to the easy axis and with an anisotropic g-factor the AFMR frequencies read [32, 33]

$$f_{\mathrm{AF}^\pm}(B) = \frac{\gamma_\parallel}{2\pi}\left(\sqrt{\Delta^2 + \left(\frac{g_\parallel B}{4}(1-\alpha)\right)^2} \pm \frac{g_\parallel B}{4}(1+\alpha)\right) \quad \text{for} \quad B \le B_{SF} \tag{4.5}$$

$$f_{\mathrm{SF}}(B) = \frac{\gamma_\parallel}{2\pi}\sqrt{\left(\frac{g_\parallel B}{2}\right)^2 - \Delta^2} \quad \text{for} \quad B \ge B_{SF} \tag{4.6}$$

where $\Delta = \sqrt{2B_E B_A + B_A^2}$ is the zero-field splitting. The abbreviations AF and SF denote the different spin configurations as explained in fig. 2.5. The parameter α is defined as $\alpha = 1 - \frac{\chi_\parallel}{\chi_\perp}$ [34]. Since for the parallel susceptibility $\chi_\parallel = 0$ is predicted for a perfect antiferromagnet at $T = 0\,\mathrm{K}$ (c.f. fig. 2.4), $\alpha = 1$ is sometimes referred

to as the zero-temperature solution of AFMR [32]. Most compounds examined in experiments do not match the theoretical prediction of $\chi_{\parallel} = 0$ and the consideration of α is necessary [35].

When the external field is applied perpendicular to the easy axis, the resonance branch is described by [35, 36]

$$f_{\perp}(B) = \frac{\gamma_{\perp}}{2\pi}\sqrt{\left(\frac{g_{\perp}B}{2}\right)^2 + \Delta^2}. \tag{4.7}$$

In fig. 4.6 the light green as well as the dark green coloured absorption features are attributed to the resonance branch $f_{\perp}$ and included in the fit. Assuming an isotropic g-factor simplifies eqs. (4.5) to (4.7); more specifically the g-factor and thus the gyromagnetic ratio reduce to $g_{\parallel} = g_{\perp} = g_{\text{iso}}$ and $\gamma_{\parallel} = \gamma_{\perp} = \gamma_{\text{iso}}$, respectively. The fit parameters obtained for a two-sublattice model with uniaxial anisotropy considering an isotropic g-factor are summarised in table 4.2 and the fitted curves are represented in fig. 4.6 by solid lines. Attempts to improve the results by accounting for anisotropic g-values yielded two g-values that agree with each other within the error bars (c.f. appendix A). Therefore, the following analysis is limited to an isotropic g-factor.

	α	g_{iso}	Δ_{iso} [T]
Model 1	0.38(4)	2.10(1)	9.3(1)

Table 4.2: Model 1: Fit parameters for a two-sublattice AFM model of $Sr_2Ni(SeO_3)_2Cl_2$ with uniaxial anisotropy.

Model 1 yields $\alpha \approx 0.4$, suggesting that $\chi_{\parallel} \neq 0$. Such a small α parameter is the reason why f_{AF^-} and f_{SF} do not coincide at B_{SF} for zero-frequency but f_{AF^-} intersects the field axis at $B \approx 14\,\text{T}$.

The g-value of 2.10(1) is smaller than $g = 2.26(1)$ found in [10] and also smaller than typically measured values for Ni^{2+} ions in an octahedral crystal field [10]. Nevertheless, it agrees with $g_{\text{Curie}} = 2.2(1)$ obtained from a Curie-Weiss fit of the static magnetic susceptibility of $Sr_2Ni(SeO_3)_2Cl_2$.

The spin-flop field can be calculated from Δ as $B_{\text{SF}} \approx 8.9(3)\,\text{T}$. The zero-field splitting can be converted to GHz using the relation

$$\Delta_{\text{iso}}\,[\text{GHz}] = \frac{\gamma_{\text{iso}}}{2\pi}\Delta\,[\text{T}] = 272(2)\,\text{GHz}. \tag{4.8}$$

It can be seen in fig. 4.6 that three resonance branches merge into a common resonance feature at Δ_{iso}. The brown line with linear field dependence corresponds to the resonance mode f_{AF^+}. It is the theoretical expectation of this resonance branch obtained from the above mentioned fit parameters and eq. (4.5) and does not stem from the fitting directly. The data points represented by empty black triangles were

not considered during the fitting process because the corresponding resonance features are very weak. Nevertheless, they agree with f_{AF^+} within the error bars and thus confirm the theoretically expected branch f_{AF^+}.

The zero-field splitting is related to the exchange and anisotropy fields B_E and B_A but these fields cannot be extracted directly from Δ. For uniaxial anisotropy, the exchange interaction can be estimated from the saturation field via [37]

$$g\mu_B B_{\mathrm{sat}} = 2k_B SzJ \tag{4.9}$$

where z denotes the number of nearest neighbours and J is the exchange interaction. Applying the definition of the exchange field as a function of J [15]

$$B_E = \frac{2k_B SzJ}{\gamma\hbar}, \tag{4.10}$$

a relation between saturation and exchange field can be established:

$$g\mu_B B_{\mathrm{sat}} = \gamma\hbar B_E \tag{4.11}$$

$$\Rightarrow B_E = B_{\mathrm{sat}} = 31\,\mathrm{T} \tag{4.12}$$

with $B_{\mathrm{sat}} = 31\,\mathrm{T}$ taken from [10]. The knowledge of B_{sat} also enables to estimate the exchange parameter as

$$J = 10.90(4)\,\mathrm{K} \tag{4.13}$$

by use of eq. (4.9). The anisotropy field can be calculated using $\Delta = \sqrt{2B_E B_A + B_A^2}$, which yields

$$B_{A,\mathrm{iso}} = 1.35(1)\,\mathrm{T} \tag{4.14}$$

for an isotropic g-factor. As stated above, eqs. (4.5) to (4.7) are simplified expressions for the resonance branches under the assumption that $B_A \ll B_E$. This condition is fulfilled with

$$\frac{B_{A,\mathrm{iso}}}{B_E} = 0.04 \tag{4.15}$$

and the results are consistent with the above assumption.

Moreover, the anisotropy field is related to the uniaxial anisotropy D. This relation can be established via [38]

$$B_A = \frac{C_1}{2B_E} \tag{4.16}$$

$$\Rightarrow C_{1,\mathrm{iso}} = 83.7(6)\,\mathrm{T}^2. \tag{4.17}$$

The parameter C_1 is defined by [38]

$$C_1 = \frac{2k_B^2 zJD}{(g\mu_B)^2} \tag{4.18}$$

$$\Rightarrow D_{\text{iso}} = 3.8(1)\,\text{K} \tag{4.19}$$

with $z = 2$ nearest neighbors. This value is about 1 K smaller than the uniaxial anisotropy reported in [10].

Model 2: Orthorhombic Anisotropy with D ≈ E

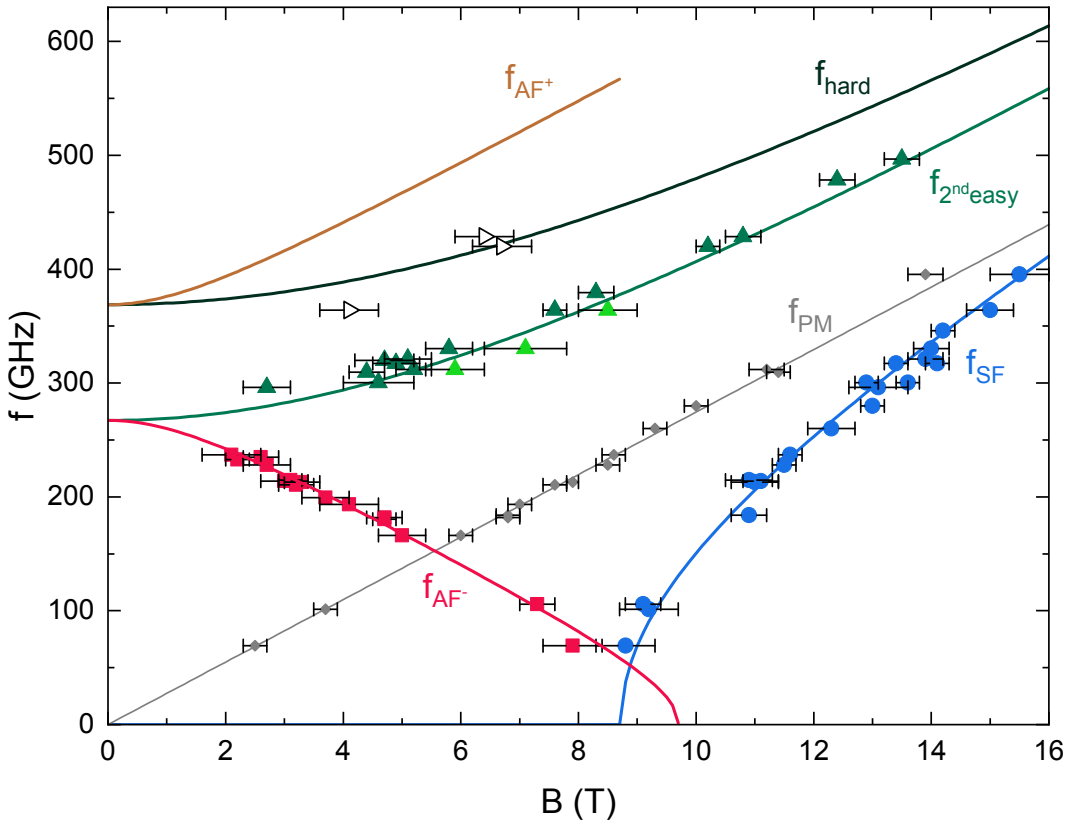


Figure 4.7: Model 2: Frequency vs. field diagram of $Sr_2Ni(SeO_3)_2Cl_2$ constructed from HF-ESR data recorded at $T = 2\,\text{K}$. Assuming a two-sublattice AFM with orthorhombic anisotropy, the three observed resonance branches are attributed to f_{AF^-}, f_{SF} and $f_{2^{\text{nd}}\text{easy}}$. The lines labelled as f_{AF^+} and f_{hard} are theoretical expectations from obtained fit parameters while f_{PM} describes a paramagnetic impurity in the sample.

For the analysis shown in fig. 4.7, i.e. Model 2, a two-sublattice antiferromagnet with orthorhombic anisotropy is assumed. This requires a distinction between three external field directions. The following equations are taken from [26] and are valid

for $B_{A1}, B_{A2} \ll B_E$ with the anisotropy fields B_{A1}, B_{A2} and the exchange field B_E. Along the easy axis the resonance frequencies are given as

$$f_{\mathrm{AF}^{\pm}}(B) = \frac{\gamma_{\mathrm{easy}}}{2\pi\sqrt{2}} \Bigg[(1+\alpha)^2 B_{\mathrm{easy}}^2 + C_1 + C_2 \pm \Big\{ \left(1-\alpha^2\right)^2 B_{\mathrm{easy}}^4 + 2\,(1+\alpha)^2 B_{\mathrm{easy}}^2 \,(C_1 + C_2) + (C_1 - C_2)^2 \Big\}^{\frac{1}{2}} \Bigg]^{\frac{1}{2}} \tag{4.20}$$

for $B \leq B_{SF}$ and with $\alpha = 1 - \chi_{\parallel}/\chi_{\perp}$. The parameters C_1 and C_2 define the anisotropy constants along the second-easy and the hard axis, respectively. For $B \geq B_{SF}$ the field dependence of the resonance frequency becomes much simpler, reading

$$f_{\mathrm{SF}}(B) = \frac{\gamma_{\mathrm{easy}}}{2\pi} \left[B_{\mathrm{easy}}^2 - C_1 \right]^{\frac{1}{2}}. \tag{4.21}$$

A similar relation is found for fields applied along the second-easy axis

$$f_{2^{\mathrm{nd}}\mathrm{easy}}(B) = \frac{\gamma_{2^{\mathrm{nd}}\mathrm{easy}}}{2\pi} \left[B_{2^{\mathrm{nd}}\mathrm{easy}}^2 + C_1 \right]^{\frac{1}{2}} \tag{4.22}$$

and hard axis

$$f_{\mathrm{hard}}(B) = \frac{\gamma_{\mathrm{hard}}}{2\pi} \left[B_{\mathrm{hard}}^2 + C_2 \right]^{\frac{1}{2}}. \tag{4.23}$$

The light green as well as the dark green coloured absorption features, are attributed to the resonance branch $f_{2^{\mathrm{nd}}\mathrm{easy}}$ and included in the fit.

In all equations $B_i = \frac{g_i}{2} B$ (i = easy, 2^{nd}easy, hard) is the modified magnetic field depending on the direction of the applied external magnetic field B [39]. For an isotropic g-factor the AFMR frequencies are simplified with $g_{\mathrm{easy}} = g_{2^{\mathrm{nd}}\mathrm{easy}} = g_{\mathrm{hard}} = g_{\mathrm{iso}}$, $\gamma_{\mathrm{easy}} = \gamma_{2^{\mathrm{nd}}\mathrm{easy}} = \gamma_{\mathrm{hard}} = \gamma_{iso}$ and $B_{\mathrm{easy}} = B_{2^{\mathrm{nd}}\mathrm{easy}} = B_{\mathrm{hard}} = B_{\mathrm{iso}}$.

In the description of the resonance modes by means of Model 2 (fig. 4.7) the observed resonance features have been assigned to f_{AF^-}, f_{SF} and $f_{2^{\mathrm{nd}}\mathrm{easy}}$ only, implying that the branches f_{AF^+} and f_{hard}, expected based on the assumed model considering orthorhombic anisotropy, were not observed. An anisotropic g-factor was not considered because without the observation of the resonance branch f_{hard}, the component of the g-factor parallel to the hard axis cannot be determined. The fit parameters for an isotropic g-factor are summarised in table 4.3.

The resonance branches f_{AF^-} and f_{SF} intersect each other at finite frequency instead of merging at zero frequency which can be attributed to $\alpha = 0.81 < 1$. This suggests that $\chi_{\parallel} \neq 0$. The spin-flop branch f_{SF} starts at the spin-flop field $B_{\mathrm{SF}} \approx 8.7(2)\,\mathrm{T}$.

The two zero-field splittings can be calculated from $f_{2^{\mathrm{nd}}\mathrm{easy}}(B = 0)$ for Δ_1 and

	α	g_{iso}	C_1 [T^2]	C_2 [T^2]
Model 2	0.81(9)	2.09(1)	83(1)	159(22)

Table 4.3: Model 2: Fit parameters for a two-sublattice AFMR model of $Sr_2Ni(SeO_3)_2Cl_2$ with orthorhombic anisotropy and $D \approx E$.

$f_{\mathrm{hard}}(B = 0)$ for Δ_2. The results are

$$\Delta_1 = \frac{\gamma_{\mathrm{iso}}}{2\pi}\sqrt{C_1} = 267(2)\,\mathrm{GHz} \tag{4.24}$$

$$\Delta_2 = \frac{\gamma_{\mathrm{iso}}}{2\pi}\sqrt{C_2} = 369(26)\,\mathrm{GHz} \tag{4.25}$$

and can be seen as branches merging into one resonance in fig. 4.7. It should be noted that Δ_2 is 100 GHz larger than Δ_1. The higher zero-field splitting corresponds to the branches f_{AF^+} and f_{hard}, which however have not been detected. Despite thorough search, no resonance features have been observed for frequencies $f > 370\,\mathrm{GHz}$ at low fields.

The branches f_{AF^+} and f_{hard} are calculated based on the fit parameters in table 4.3. The resonance features without attribution to a resonance branch at $f \approx 400\,\mathrm{GHz}$ agree with f_{hard} whereas the resonance signal at 4 T and 360 GHz is neither well described by f_{hard} nor f_{AF^+}. Moreover, no observed features lie on the simulated branch f_{AF^+}.

Additionally, C_2 and Δ_2 have a large uncertainty. This is associated with the fact that the branches f_{AF^+} and f_{hard}, corresponding to resonance features parallel to the easy and hard axis, respectively, were not detected and therefore not included in the fit. Both branches are important to determine a reliable result for the parameter C_2 as the corresponding resonance frequencies are given in terms of C_2 (compare eqs. (4.20) and (4.23)). Without f_{AF^+} and f_{hard} considered in the fitting process, only f_{AF^-} is used for determining of C_2, thus yielding an inaccurate value with large uncertainty.

To justify the approximation $B_{A1}, B_{A2} \ll B_E$, the exchange and anisotropy fields are calculated from C_1 and C_2. The exchange field is defined in eq. (4.10) [15]. For orthorhombic anisotropy, it can be related to the second critical field via [16]

$$g\mu_B B_{c2} = 2k_B SzJ = g\mu_B B_E, \tag{4.26}$$

yielding

$$B_E = B_{c2} = 23.7\,\mathrm{T} \tag{4.27}$$

with B_{c2} from [10]. Additionally, the exchange parameter

$$J = 8.32(4)\,\mathrm{K} \tag{4.28}$$

can be estimated using eq. (4.26). The anisotropy fields can be expressed as [38]

$$B_{A1} = \frac{C_1}{2B_E} = 1.75(2)\,\mathrm{T} \qquad \text{and} \qquad B_{A2} = \frac{C_2}{2B_E} = 3.3(5)\,\mathrm{T} \tag{4.29}$$

With these values, the ratio between anisotropy und exchange field reads

$$\frac{B_{A1}}{B_E} = 0.07 \qquad \text{and} \qquad \frac{B_{A2}}{B_E} = 0.14 \tag{4.30}$$

thus questioning the validity of the approximation $B_{A1}, B_{A2} \ll B_E$, especially for B_{A2}.

Furthermore, the uniaxial and transverse anisotropies D and E can be obtained from C_1, C_2 and g, provided that the exchange interaction J is known. The relation between C_1, C_2 and the anisotropy constants K_1, K_2 is defined as [26]

$$C_1 = 2AK_1 \qquad \text{and} \qquad C_2 = 2AK_2 \tag{4.31}$$

with the anisotropy constants K_1 for the second-easy axis and K_2 for the hard axis restricted to $K_1 < K_2$. The molecular field constant A of the sublattice is given as [38]

$$A = \frac{2zJ}{N\left(g\mu_B\right)^2} \tag{4.32}$$

where N is the number of magnetic ions per unit cell. The anisotropy constants are given by the relations [38]

$$K_1 = (D - E)\,\frac{N}{2} \tag{4.33}$$

$$K_2 = (D + E)\,\frac{N}{2} \tag{4.34}$$

for $S = 1$ and D, $E > 0$. With these expressions the anisotropy constants can be estimated as

$$D = (C_1 + C_2)\,\frac{\left(g\mu_B\right)^2}{4zJk_B^2} = 7.2(3)\,\mathrm{K} \tag{4.35}$$

$$E = (C_2 - C_1)\,\frac{\left(g\mu_B\right)^2}{4zJk_B^2} = 2.2(3)\,\mathrm{K} \tag{4.36}$$

with $z = 2$ nearest neighbours. They do not match $D = 4.86\,\mathrm{K}$ and $E = 0.60\,\mathrm{K}$ found in [10].

Model 3: Orthorhombic Anisotropy with $\mathbf{D} \gg \mathbf{E}$

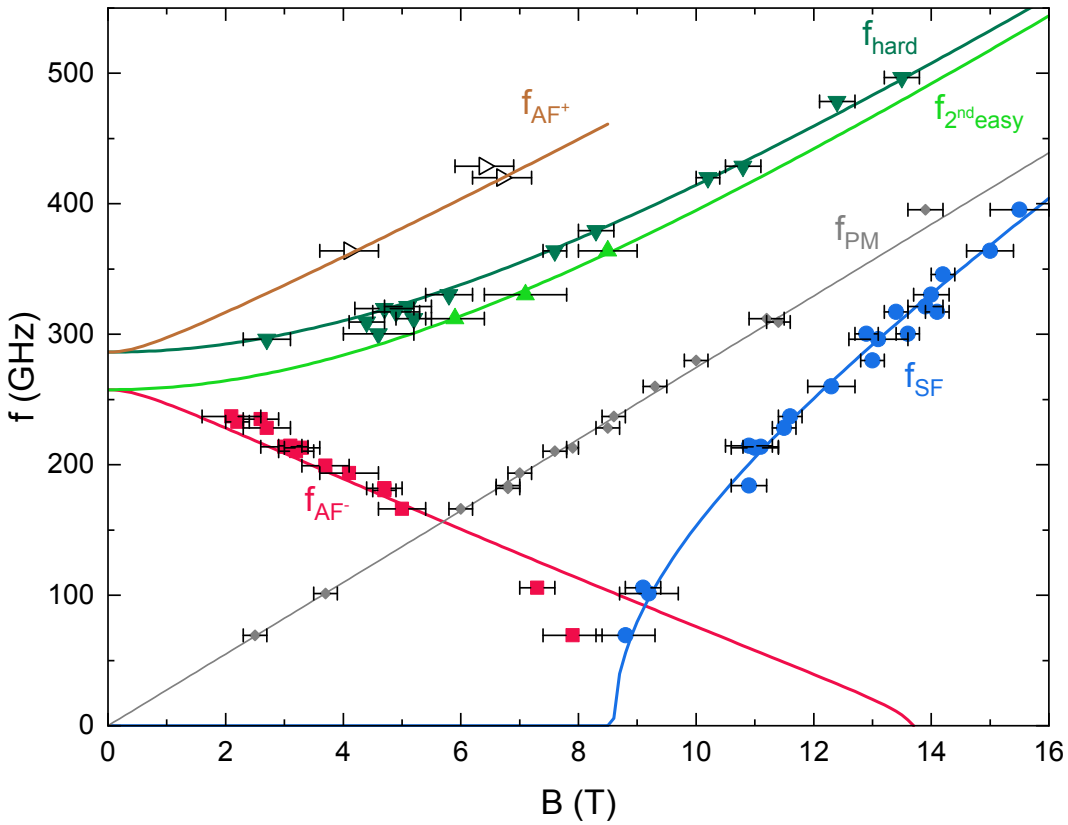


Figure 4.8: Model 3: Frequency vs. field diagram of $Sr_2Ni(SeO_3)_2Cl_2$ constructed from HF-ESR data recorded at $T = 2\,\mathrm{K}$. Assuming a two-sublattice AFM with orthorhombic anisotropy, the four resonance branches are attributed to f_{AF^-}, f_{SF}, $f_{2^{\mathrm{nd}}\mathrm{easy}}$ and f_{hard}. The branch f_{AF^+} is a theoretical prediction from obtained fit parameters while f_{PM} describes a paramagnetic impurity in the sample.

In Model 3, shown in fig. 4.8, a two-sublattice antiferromagnet with orthorhombic anisotropy similar to Model 2 is assumed and the resonance branches can be described by the same eqs. (4.20) to (4.23) applied in Model 2. Nevertheless, the observed resonance features are attributed to different resonance branches predicted for orthorhombic anisotropy. The branch $f_{2^{\mathrm{nd}}\mathrm{easy}}$ in Model 2 includes three resonance features which have a very broad linewidth and can be interpreted as two resonance features at magnetic fields very close to each other. These resonance features are highlighted in figs. 4.6 to 4.8 by light green symbols. They are interpreted as an additional branch in Model 3. The observed resonance branches can hence be attributed to f_{AF^-}, f_{SF}, $f_{2^{\mathrm{nd}}\mathrm{easy}}$ and f_{hard}. The resulting fit parameters for an isotropic g-factor are listed in table 4.4. As in Model 1, attempts have been made to improve the fit by accounting for an anisotropic g-value. The result is three components of the g-value for the different directions which match each other within the error bars

	α	g_{iso}	C_1 [T^2]	C_2 [T^2]
Model 3	0.40(4)	2.07(1)	79(2)	98(3)

Table 4.4: Model 3: Fit parameters for a two-sublattice AFMR model of $Sr_2Ni(SeO_3)_2Cl_2$ with orthorhombic anisotropy and $D \gg E$.

and are referred to in appendix A. Therefore, further analysis is carried out assuming an isotropic g-factor $g_{\mathrm{iso}} = 2.07(1)$ for $Sr_2Ni(SeO_3)_2Cl_2$.

The parameter $\alpha = 0.40(4)$ is far below the zero temperature value and of similar size as for an antiferromagnet with uniaxial anisotropy implying that the parallel susceptibility $\chi_{\parallel} \neq 0$ at $T = 2\,\mathrm{K}$. $\alpha < 1$ is the reason why f_{AF^-} and f_{SF} do not merge at $B_{\mathrm{SF}} = 8.6(1)\,\mathrm{T}$ and zero frequency but intersect at $B \approx 9\,\mathrm{T}$ and finite frequency.

The parameters C_1 and C_2 are closer together than in Model 2 (c.f. table 4.3) with C_2 being significantly lower in Model 3. Moreover, the uncertainty of C_2 is much smaller now with the additional branch included in the fit. C_1 and C_2 result in the zero-field splittings

$$\Delta_1 = 258(3)\,\mathrm{GHz} \qquad \text{and} \qquad \Delta_2 = 286(4)\,\mathrm{GHz}, \tag{4.37}$$

calculated using eqs. (4.24) and (4.25). These values are very close to each other, which makes it hard to resolve $f_{2^{\mathrm{nd}}\mathrm{easy}}$ and f_{hard} individually.

The theoretically predicted branch f_{AF^+} agrees with the resonance features at approximately (6.5 T, 420 GHz) and (4 T, 360 GHz) which were not attributed to a resonance branch before the fit.

To justify the approximation $B_{A1}, B_{A2} \ll B_E$, the exchange and anisotropy fields are calculated from C_1 and C_2. Following the same steps as in eqs. (4.29) and (4.30) with $B_E = 23.7\,\mathrm{T}$ and $J = 8.24(4)\,\mathrm{K}$ yields

$$B_{A1} = 1.67(3)\,\mathrm{T} \qquad \text{and} \qquad B_{A2} = 2.06(5)\,\mathrm{T} \tag{4.38}$$

for the anisotropy fields and

$$\frac{B_{A1}}{B_E} = 0.07 \qquad \text{and} \qquad \frac{B_{A2}}{B_E} = 0.09 \tag{4.39}$$

for the ratios between anisotropy and exchange fields. Therefore, the approximation $B_{A1}, B_{A2} \ll B_E$ is valid when assuming orthorhombic anisotropy with $D \gg E$ in $Sr_2Ni(SeO_3)_2Cl_2$.

Proceeding as in eqs. (4.35) and (4.36), the axial and transverse anisotropies can be determined as

$$D = 5.20(4)\,\mathrm{K} \qquad \text{and} \qquad E = 0.55(4)\,\mathrm{K}. \tag{4.40}$$

These values agree with $D = 4.86\,\mathrm{K}$ and $E = 0.60\,\mathrm{K}$ found in [10].

4.3.3 Theoretically Predicted Frequency vs. Field Diagram

It is possible to estimate values for the antiferromagnetic exchange interaction $J > 0$, the axial anisotropy $D > 0$ as well as the transverse anisotropy $E > 0$ from the observed features in the isothermal magnetisation. The field dependence of the magnetisation has been probed in [10] using pulsed magnetic fields up to 45 T. The magnetic susceptibility $\mathrm{d}M/\mathrm{d}B$ reveals two transition features at $B_{\mathrm{c1}} = 9.0\,\mathrm{T}$, $B_{\mathrm{c2}} = 23.7\,\mathrm{T}$ and the saturation field at $B_{\mathrm{sat}} = 31.0\,\mathrm{T}$. Kozlyakova et al. [10] used these features to estimate the values $J = 9.02\,\mathrm{K}$, $D = 4.86\,\mathrm{K}$ and $J = 0.60\,\mathrm{K}$. Reviewing the calculations stated in their publication revealed the necessity of adjusting the applied equations by accounting for the number of nearest neighbours. These changes lead to slightly different results for J, D and E.

First of all, as discussed in section 4.2, a measurement of the magnetisation in static magnetic fields up to 13.7 T was carried out in our laboratory. Probing the sample in static fields gives a smaller value of the first transition feature with $B_{\mathrm{c1}} = 8.4\,\mathrm{T}$ as compared to the results reported in [10]. This field value will be used in the following calculations.

Interpreting B_{c1} as a spin-flop transition [10], allows to express the critical field in terms of J, D and E as

$$(g\mu_B B_{c1})^2 = 4k_B^2 SzJ\,(D - E) \tag{4.41}$$

with the Bohr magneton μ_B, the Boltzmann constant k_B, the number of nearest neighbours z and spin S of the system. Equation (4.43) follows from the zero of the spin-flop branch for orthorhombic anisotropy in the system, $B_{\mathrm{SF}} = \sqrt{C_1}$ [38]. The second critical field and the saturation field can be written in terms of J and D as [16]

$$g\mu_B B_{c2} = 2k_B SzJ \tag{4.42}$$

$$g\mu_B B_{sat} = 2k_B S\,(zJ + D) = g\mu_B B_{c2} + 2k_B SD. \tag{4.43}$$

J, D and E are given in units of Kelvin in all three equations. Using $S = 1$, $z = 2$ and $g_{\mathrm{Curie}} = 2.2(1)$ yields the following values

$$\begin{aligned} J &= 8.37(4)\,\mathrm{K} \\ D &= 5.16(2)\,\mathrm{K} \\ E &= 0.33(4)\,\mathrm{K} \end{aligned} \tag{4.44}$$

which are in the same order of magnitude as the values obtained in [10]. The largest deviation is found for the transverse anisotropy E, being almost 50 % smaller than the published value.

Applying eqs. (4.31), (4.32) and (4.34) the parameters C_1, C_2 can be obtained as

$$C_1 = 81(1)\,\mathrm{T}^2 \qquad \text{and} \qquad C_2 = 92(1)\,\mathrm{T}^2 \tag{4.45}$$

Using eqs. (4.24) and (4.25) yields the zero-field splittings

$$\Delta_1 = 265(2)\,\mathrm{GHz} \qquad \text{and} \qquad \Delta_2 = 282(2)\,\mathrm{GHz}. \tag{4.46}$$

Applying eqs. (4.20) to (4.23) the resulting frequency dependence of the resonance branches is shown in fig. 4.9. Three different values $\alpha = 1$, $\alpha = 0.7$ and $\alpha = 0.4$ are assumed for the theoretical prediction of the resonance branches.

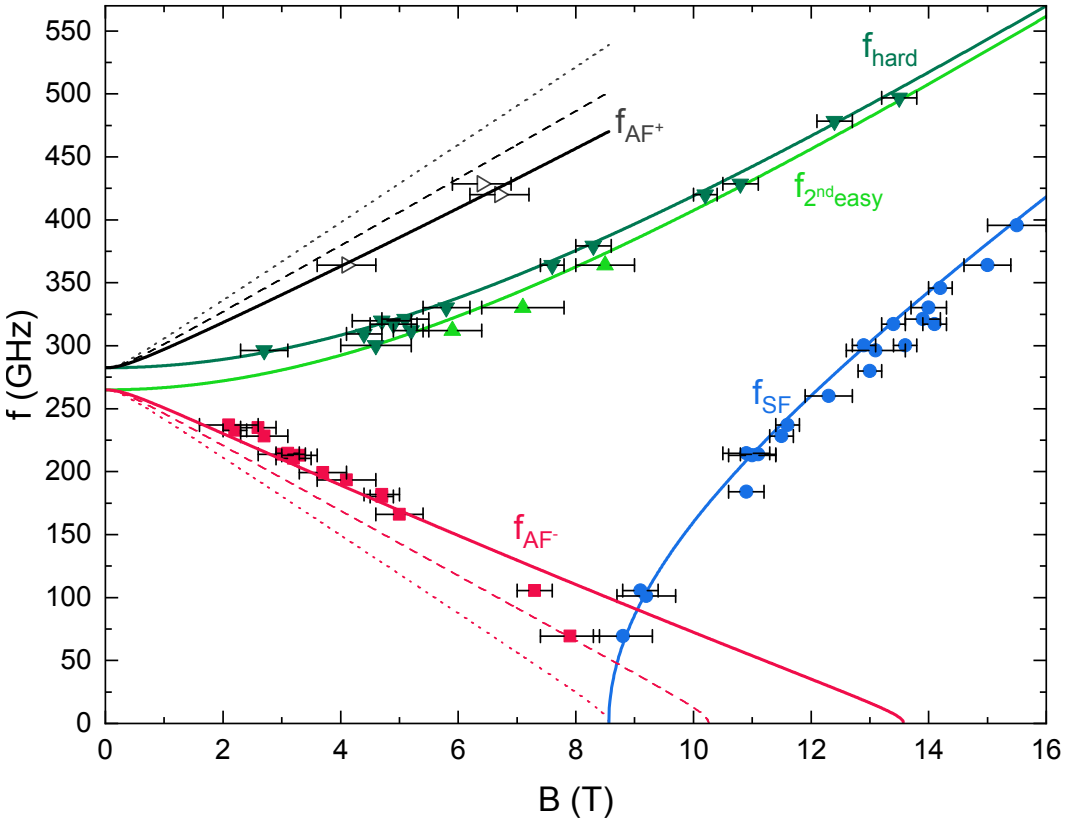


Figure 4.9: Theoretically predicted frequency vs. field diagram of $Sr_2Ni(SeO_3)_2Cl_2$ assuming orthorhombic anisotropy with $J = 8.37\,\mathrm{K}$, $D = 5.16\,\mathrm{K}$, $E = 0.33\,\mathrm{K}$ and $g = 2.2$. The dotted, dashed and solid lines for f_{AF^+} and f_{AF^-} represent different values of α with dotted: $\alpha = 1$, dashed: $\alpha = 0.7$, solid: $\alpha = 0.7$

There are three resonance branches for an external field parallel to the easy axis: f_{AF^+}, f_{AF^-} and f_{SF}. The two branches f_{AF^+} and f_{AF^-} describe the antiferromagnetic phase of the resonance modes and therefore exist only up to the spin-flop field $B_{\mathrm{SF}} = 8.4\,\mathrm{T}$ where f_{AF^-} and f_{SF} meet for zero frequency for a perfect antiferromagnet with $\alpha = 1$. The field dependence of f_{AF^+} and f_{AF^-} is approximately linear except in the vicinity of $B = 0\,\mathrm{T}$ for both branches and $B = B_{\mathrm{SF}}$ for f_{AF^-}. This emphasises the

importance of recording data points in these magnetic field areas. The parameter α has a large influence on the field dependence of f_{AF^+} and f_{AF^-}. The larger the value of α, the steeper the frequency increase (decrease) for f_{AF^+} (f_{AF^-}) with increasing magnetic fields.

The resonance branch $f_{2^{\mathrm{nd}}\mathrm{easy}}$, obtained for magnetic fields parallel to the second easy axis, and f_{AF^-} merge into a common feature at $\Delta_1 = 265\,\mathrm{GHz}$. f_{AF^-} and f_{hard} coincide for zero-field at $\Delta_2 = 282\,\mathrm{GHz}$. Δ_2 is not much larger than Δ_1, hence $f_{2^{\mathrm{nd}}\mathrm{easy}}$ and f_{hard} are very close to each other, almost merging for high magnetic fields. This implies that an experimental setup with a high resolution is required to verify that the resonance features belong to individual branches for $f > \Delta_1$ and to detect them if the existence of both branches has been confirmed.

The theoretically predicted branches f_{SF}, $f_{2^{\mathrm{nd}}\mathrm{easy}}$ and f_{hard} agree very well with the recorded resonance signals. Resonance features in the AF mode ($B < B_{\mathrm{SF}}$) agree best with the expected branches f_{AF^+} and f_{AF^-} for $\alpha = 0.4$ which agrees with the experimentally found value in Model 1 and Model 3.

4.3.4 Discussion of the Frequency vs. Field Diagram

The final results obtained from the different interpretations of magnetic anisotropy assumed for $Sr_2Ni(SeO_3)_2Cl_2$ in Model 1, Model 2 and Model 3 are summarised in table 4.5 for an isotropic g-value. Isotropic g-factors are typical for Ni^{2+} ions in a slightly distorted octahedral crystal field environment [36] although it remains to be argued whether the octahedra are actually only slightly distorted with the distance between Ni and Cl ions being 19 % larger than the distance between Ni and O ions. Nevertheless, the value of $g \approx 2.1$ is smaller than usually measured values around 2.2 for Ni^{2+} ions [30] but it agrees with the Curie-Weiss fit of the static susceptibility (c.f. fig. 4.2).

Comparing the frequency vs. field diagrams obtained from resonance spectra with the theoretically predicted diagram demonstrates that Model 2 (c.g. fig. 4.7) assumes the same orthorhombic anisotropy as the computated phase diagram (c.g. fig. 4.9). The second zero-field splitting Δ_2 in Model 2 is almost 100 GHz larger than the expected value, resulting in axial and transverse anisotropies D and E that are larger than the expected values in table 4.5. Additionally, the three resonance features that were not assigned to a particular resonance due to their weak signal do not agree with the resonance branches $f_{\mathrm{AF}+}$ and f_{hard} which are calculated from the obtained fit parameters. Therefore, it is concluded that $Sr_2Ni(SeO_3)_2Cl_2$ cannot be described by an orthorhombic two sublattice AFM with $D \approx E$ as assumed for Model 2, i.e. the phase diagram in fig. 4.7.

Model 1 in fig. 4.6 assumes uniaxial instead of orthorhombic anisotropy in the compound. Therefore, it features only one zero-field splitting $\Delta_1 = 272(2)\,\mathrm{GHz}$ which lies in between the two zero-field splittings of the theoretical prediction. Nevertheless, the uniaxial anisotropy D, estimated from Δ_1, is lower than the expected value but

	Model 1	Model 2	Model 3	Prediction
α	0.38(4)	0.81(9)	0.40(4)	0.4
g	2.10(1)	2.09(1)	2.07(1)	2.2(1)
Δ_1[GHz]	272(2)	267(2)	258(3)	265(2)
Δ_2[GHz]	-	369(26)	286(4)	282(2)
B_{SF}[T]	8.9(3)	8.7(1)	8.6(1)	8.4(1)
D[K]	3.8(1)	7.2(3)	5.10(4)	5.16(2)
E[K]	-	2.2(3)	0.55(4)	0.33(4)
J[K]	10.9(4)	8.32(4)	8.24(4)	8.37(4)

Table 4.5: Summary of the defining quantities of AFMR in $Sr_2Ni(SeO_3)_2Cl_2$ for Model 1, Model 2 and Model 3, assuming different magnetic anisotropies in the compound.

in the same order of magnitude. The measured resonance branch $f_{\mathrm{AF}-}$ shows similar behaviour as the theoretically predicted branch in the same mode when $\alpha = 0.4$ is assumed. The fit yields $\alpha = 0.38(4)$ which agrees with the value giving the best results of the computed phase diagram. The resonance branch $f_{\mathrm{AF}+}$, calculated from the obtained fit parameters agrees with the unidentified resonance signals at approximately (6.5 T, 420 GHz) and (4 T, 360 GHz) within the error bars, thus lending support to the interpretation of uniaxial anisotropy in $Sr_2Ni(SeO_3)_2Cl_2$.

Model 3 in fig. 4.8 assumes the same magnetic anisotropy as the theoretically predicted frequency vs. field diagram. The zero-field splittings Δ_1, Δ_2 as well as the axial and transverse anisotropies D and E agree with the prediction. The resonance branch $f_{\mathrm{AF}+}$, calculated from the obtained fit parameters matches with the three resonance signals not assigned to any resonance branch within the error bars. This confirms the interpretation of orthorhombic anisotropy with small transverse anisotropy E. Comparing Model 3 with the theoretically expected phase diagram shows that the computed branches with $\alpha = 0.4$, match the resonance branches obtained from experiment.

As a conclusion, both the uniaxial anisotropy as well as the orthorhombic anisotropy with small E describe the frequency vs. field diagram equally well. Both interpretations give $\alpha \approx 0.4 < 1$ emphasising the importance of $\chi_{\parallel} \neq 0$ in $Sr_2Ni(SeO_3)_2Cl_2$. Explanations for this might be quantum or thermal fluctuations. As measurements were performed at $T = 2\,\mathrm{K} = 1/3T_N$, especially thermal fluctuations are plausible. Moreover, resonance signals for $B < 2\,\mathrm{T}$ and $f < 70\,\mathrm{GHz}$ were not observed despite numerous measurements in this frequency and field range. Data points in these field and frequency ranges are particularly important to distinguish between uniaxial and orthorhombic anisotropy since these are the values for which $f_{\mathrm{AF}-}$ shows bending in-

stead of linear field dependence in orthorhombic anisotropy. This problem does not arise due to the measurement technique as previous measurements have been successfully performed at these values [36]. It can rather be attributed to the coupling properties of the compound to the microwave frequency.

The small transverse anisotropy in the case of the assumed orthorhombic anisotropy in Model 3, results in two resonance branches $f_{2^{\text{nd}}\text{easy}}$ and f_{hard} being very close to each other. This makes it very hard to resolve both branches individually, complicating the task to identify the type of magnetic anisotropy present in the compound. Since all measurements were performed on a powder sample and no single crystal measurements are available, the easy, second-easy and hard axis cannot be attributed to the crystallographic axes.

Assuming orthorhombic anisotropy in Model 3 yields values for the axial and transverse anisotropy that agree with D and E estimated from magnetisation measurements in [10]. Moreover, the zero-field splittings in the measured and theoretically predicted phase diagram agree. Therefore, the orthorhombic anisotropy with small E predicted by [10], can be confirmed.

As a conclusion, the coincidence of Model 3 and the theoretically predicted phase diagram supports the previous classification of $Sr_2Ni(SeO_3)_2Cl_2$ as a XY-AFM [10]. The found orthorhombic anisotropy features only a small transverse anisotropy E and can therefore also be well described by Model 1 which assumes uniaxial anisotropy.

4.3.5 Temperature Dependence

The temperature dependence of resonance signals was recorded at $f = 213.8\,\text{GHz}$ in a temperature interval ranging from 2 to 120 K. This frequency is below the first zero-field splitting for all three interpretations of the phase diagram mentioned above. Therefore, this measurement reveals information about the behaviour of the antiferromagnetic resonance modes below $\Delta 1$ as well as the characteristics of the compound at elevated temperatures in the disordered phase.

Selected spectra are shown in fig. 4.10 with resonance features in the antiferromagnetic and paramagnetic phase represented by green and grey spectra, respectively. The ordering temperature $T_N = 6\,\text{K}$ is highlighted by a red spectrum. The magnetic field was chosen to range from 0 T to 14 T for better visualisaton. Temperatures not shown demonstrate strong intensities due to phase and background correction effects and jumps in the transmission and are therefore left out for better visualisation as well.

The antiferromagnetic resonance mode occurs at 3 T with a broad linewidth larger than 1 T. Such broad features are typical for AFMR in the long-range ordered state of powder samples [39]. The position of the resonance field does not change with increasing temperature. This indicates that no internal fields, which influence the resonance signal, develop below T_N. Moreover, the intensity of the recorded signal decreases significantly for T approaching the ordering temperature, but it remains

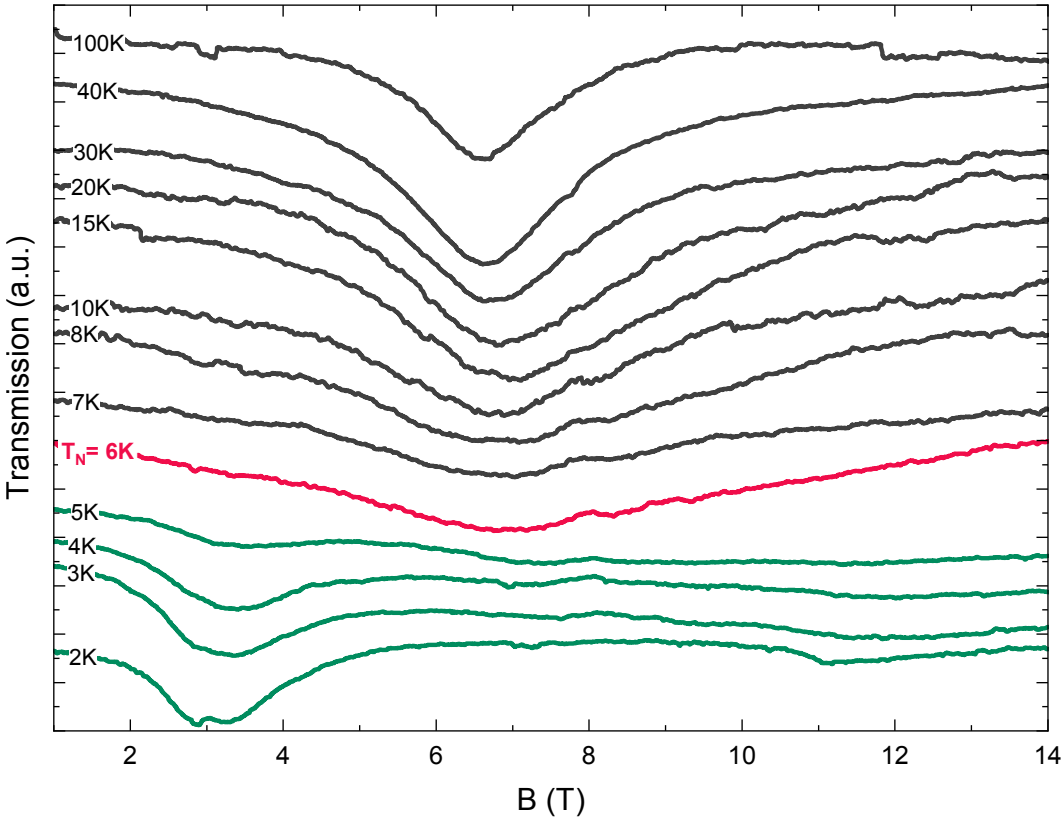


Figure 4.10: Temperature dependent ESR spectra in $Sr_2Ni(SeO_3)_2Cl_2$ for temperatures ranging from 2 to 100 K measured at $f = 213.8$ GHz.

visible until 5 K. The spin-flop mode can be observed at $B \approx 11$ T at 2 K. Its intensity is quite small already at the lowest measured temperature and the signal vanishes for larger T. The vanishing of these two resonance features at $T_N = 6$ K confirms that the recorded signals correspond to antiferromagnetic resonances in the ordered phase of the compound and do not originate from paramagnetic impurities [26].

For $T \geq T_N$ the resonance signal turns into a paramagnetic feature that covers almost the entire magnetic field range at the ordering temperature. Its temperature dependence of the resonance field, the effective g-factor and the linewidth is shown in fig. 4.11.

The absorption feature occurs at $T_N = 6$ K and $B_{\text{res}} = 7.2$ T. The resonance fields decrease exponentially with decreasing temperature until they fluctuate about $B_{\text{res}} = 6.6$ T at temperatures above 50 K. From the resonance field, the effective g-factor can be calculated via the paramagnetic resonance condition [37]

$$g_{eff} = \frac{213.8\,\text{GHz}}{B_{\text{res}} \cdot 13.996\,\text{GHz/T}}. \tag{4.47}$$

Since only one absorption feature was observed, it can be deduced that the compound has an isotropic g-factor. This is expected for Ni^{2+} ions in an octahedral crystal field with slight distortion [36] and is also reflected in the frequency vs. field diagram discussed above. The effective g-factor starts at $g = 2.12(1)$ for $T = T_N$ and demonstrates a strong increase with temperatures until $T = 50\,\mathrm{K} > 8T_N$. For higher temperatures it stays approximately constant at $g = 2.31(5)$. The high temperature value agrees with $g_{\mathrm{Curie}} = 2.2(1)$ determined by a Curie-Weiss fit of the static susceptibility.

The shift in the resonance field at lower temperatures implies the evolution of internal fields in the system and suggests the contribution of short-range correlations below 50 K [40]. This agrees with the results obtained from the Curie-Weiss fit of the static susceptibility in fig. 4.2 which deviates from the measured curve at temperatures below 100 K, thus inferring to the evolution of antiferromagnetic fluctuations [41]. The evolution of short-range order up to $T = 50\,\mathrm{K} > 8T_N$, i.e. well above the long-range AFM ordering temperature, could hint at rather two dimensional magnetic exchange interactions and magnetic frustration in $Sr_2Ni(SeO_3)_2Cl_2$ [39].

The temperature dependence of the linewidth ΔB, shown in the lower half of fig. 4.11, demonstrates an exponential increase with decreasing temperatures for T approaching the ordering temperature $T_N = 6\,\mathrm{K}$ at which it reaches its maximum value of $\Delta B = 10\,\mathrm{T}$. For $T \geq 50\,\mathrm{K}$ $\Delta B \approx 2\,\mathrm{T}$ does not show significant temperature dependence at least up to 120 K. This suggest that spin-lattice correlations are not relevant since they would give a linear contribution to the temperature behaviour of the linewidth [42]. The strong divergence that occurs upon cooling for $T \to T_N$, also referred to as critical broadening of the linewidth, hints at the evolution of spin-spin correlations and the presence of AFM fluctuations [41].

The highest achievable temperature in this measurement series was 120 K. This is not far above 100 K where the Curie-Weiss fit starts deviating from the static susceptibility data. Therefore, further investigation should include HF-ESR measurements up to room temperature to determine the spectroscopic g-factor of $Sr_2Ni(SeO_3)_2Cl_2$.

As a conclusion, the shift in the resonance field and thus in the g-value in the paramagnetic temperature regime as well as the broadening of the linewidth when T approaches T_N from high temperatures indicates the combination of exchange and anisotropic spin-spin interactions in this compound [42].

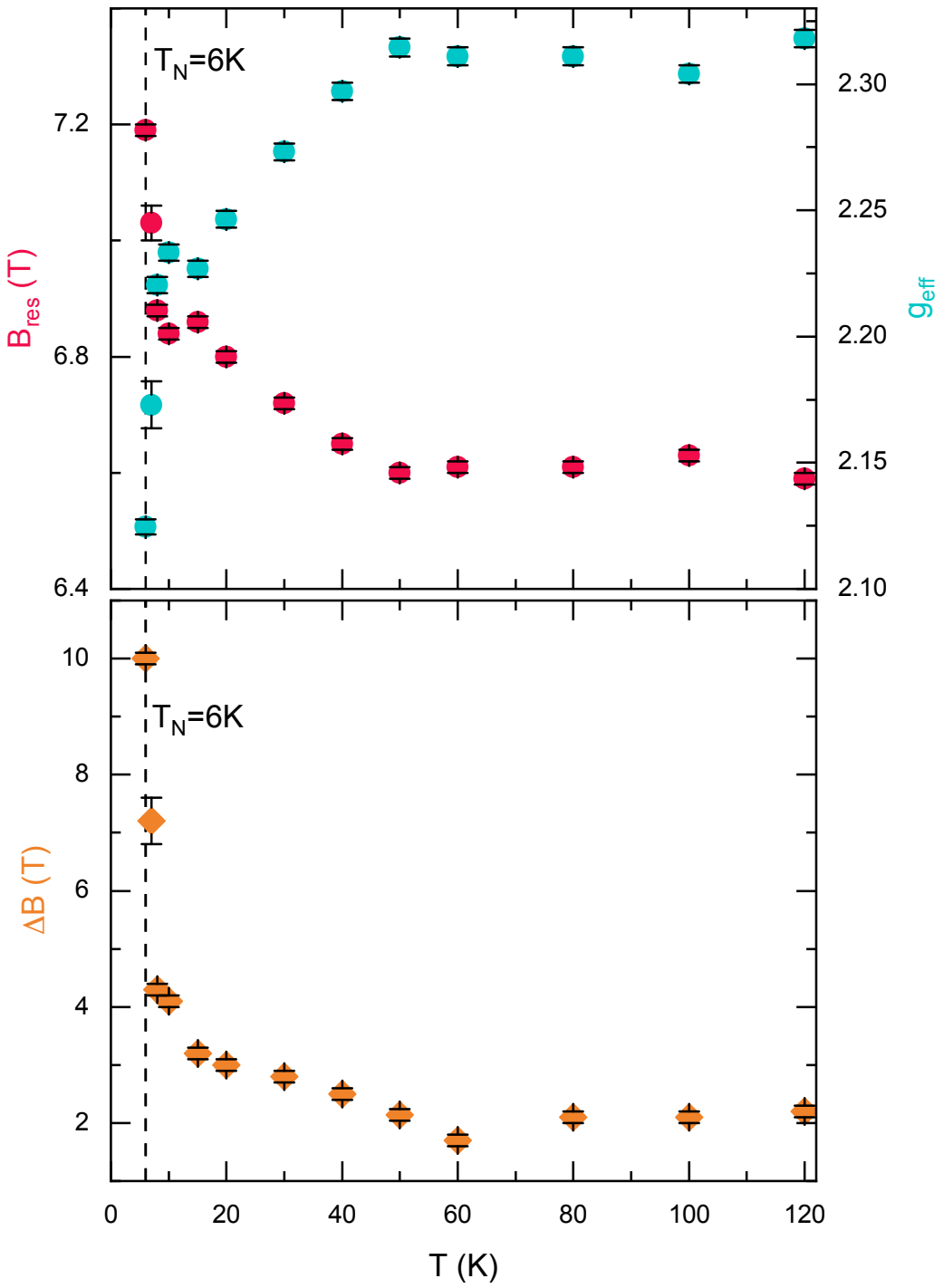


Figure 4.11: Temperature dependence of the resonance field B_{res}, the effective g-factor and the linewidth ΔB in $Sr_2Ni(SeO_3)_2Cl_2$ measured with HF-ESR at $f = 213.8\,\mathrm{GHz}$.

5 Antiferromagnetic $S = \frac{1}{2}$ Chain $PbCuSeO_4(OH)_2$

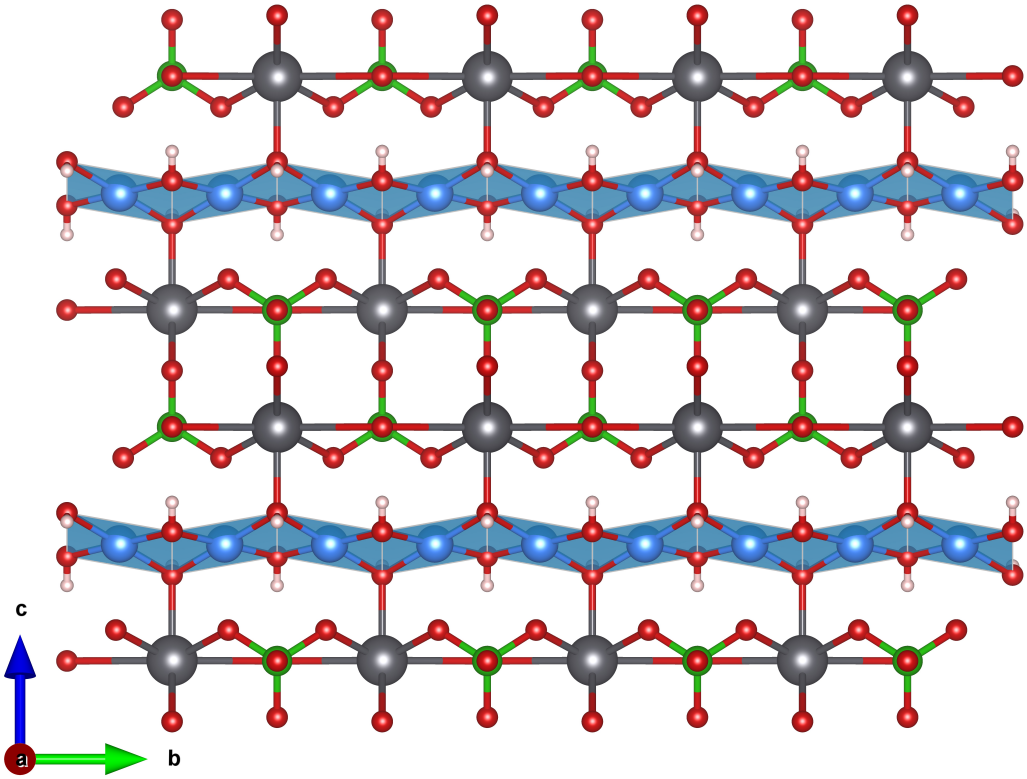
$PbCuSeO_4(OH)_2$ is a black powder which has been synthesised by our collaborators [43]. It is a structural analog of the natural mineral linarite $PbCuSO_4(OH)_2$ with sulphur replaced by selenium. The naturally occurring single crystal linarite is of bright blue colour and can be found for example in mines in the USA or in Germany [13]. It is a quasi-1D spin system with high frustration due to nearest-neighbour (NN) ferromagnetic and next-nearest-neighbour (NNN) antiferromagnetic exchange interactions [14]. Its magnetic properties have been studied extensively, e.g. by X-band ESR in [13, 14], revealing short-ranged correlations in the PM regime. HF-ESR has been performed in [44] with the result that significant biaxial anisotropy is present.

A first attempt to estimate the ferromagnetic NN J_1 and antiferromagnetic NNN J_2 exchange parameters in $PbCuSeO_4(OH)_2$ has been made by using the GGA+U approach accounting for strong Coulomb interaction on Cu sites [45]. This is based on considerations made for linarite $PbCuSO_4(OH)_2$ in [13, 14] and yields the values $J_1 = -103\,\mathrm{K}$, $J_2 = 54\,\mathrm{K}$ and $\alpha = |J_2/J_1| = 0.52$, predicting a strongly frustrated spin chain with an incommensurate singlet ground state.

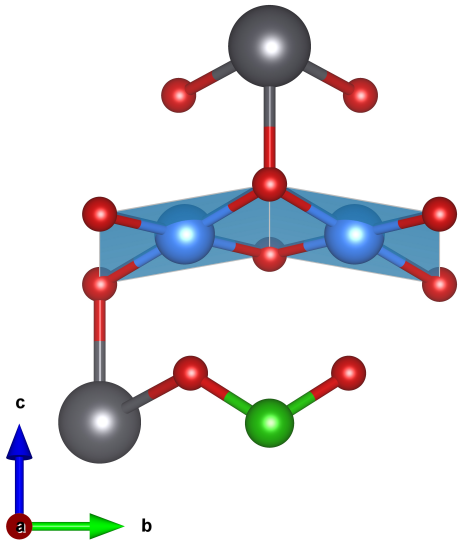
In this chapter, an X-band ESR study of the counterpart of linarite, $PbCuSeO_4(OH)_2$, is presented. Similar behaviour as reported in [13, 14] is expected but cannot be provided completely.

5.1 Crystal Structure

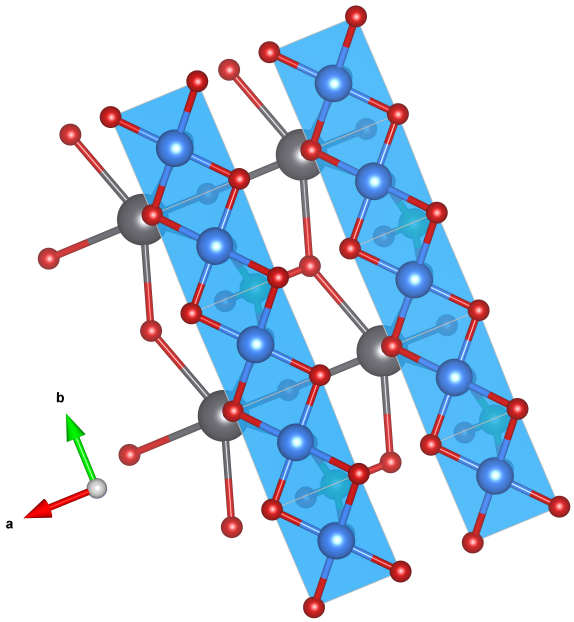
$PbCuSeO_4(OH)_2$ crystallises in a monoclinic structure of space group $P2_1/m$ with lattice constants $a = 4.748\,\text{Å}$, $b = 5.745\,\text{Å}$ and $c = 9.822\,\text{Å}$ [43]. The angle between the a- and c-axis is given by $\beta = 102.39°$. The magnetic Cu^{2+} ions, depicted by blue spheres in fig. 5.1, are surrounded by four oxygen ions (red) which are arranged in an almost perfect square with side lengths l_1 and l_2. The oxygen ions mediate magnetic exchange interactions between neighbouring Cu ions. The CuO_4 planes are tilted by $\delta = 159.0°$ with respect to adjacent planes, forming a zig-zag chain along the b-direction. This represents the quasi-1D Cu-spin chains which are well separated from each other in the c-direction by SeO_4 groups and Pb ions as shown in fig. 5.1(a). The distance between NN Cu ions along the b-axis is $2.873\,\text{Å}$. Together with oxygen ions, bound to Pb and Se, the CuO_4 planes form tetragonally distorted,



(a) Cu-chains run along the *b*-direction and are well separated from each other in *c*-direction by SeO_4 groups and Pb ions.



(b) Enlargement of the *bc*-plane to emphasise the tilted edge-sharing distorted octahedra.



(c) View on *ab*-plane clarifies 1D structure of the Cu-chains.

Figure 5.1: Crystal structure of $PbCuSeO_4(OH)_2$ in two different orientations. Cu ions are represented in blue, O ions are coloured red, while Pb and Se ions are grey and green, respectively. Crystallographic data are taken from [43] and visualised with *VESTA* [29].

edge-sharing octahedra whose axes do not correspond to the crystallographic axes. A close-up of two octahedra is given in fig. 5.1(b). There are three different distances between copper and oxygen ions given as $d_h = 2.483\,\text{Å}$, $d_1 = 1.994\,\text{Å}$ and $d_2 = 1.930\,\text{Å}$. It is important to note that d_h is 28.6 % larger than d_2 which indicates a strongly distorted octahedron and predicts magnetic anisotropy in the compound. Figure 5.1(c) highlights the one-dimensional structure of magnetic interactions in this compound. The Cu ions are directly connected by oxygen ions in b-direction while there is no direct bonding between these ions along the a-axis where the exchange path is considerably longer.

5.2 Magnetic Properties

The magnetic ions of $PbCuSeO_4(OH)_2$ are copper ions in the oxidation state 2+ with ground state electron configuration $[Ar]3d^9$, resulting in spin $S = \frac{1}{2}$ based on Hund's rules [28]. Cu^{2+} has a quenched orbital momentum $L = 0$ yielding the total angular momentum $J = |L \pm S| = \frac{1}{2}$.

Magnetic measurements discussed in this section to characterise the material have been performed by Daniel Knauer [46]. The static susceptibility $\chi = M/B$ and its inverse at 1 T are shown in fig. 5.2. The high temperature behaviour of the compound can be quantified according to the Curie-Weiss law [24]

$$\chi(T) = \frac{C}{T - \Theta} + \chi_0 \tag{5.1}$$

with the Curie constant C and Weiss temperature Θ. The temperature independent contribution χ_0 has been obtained by plotting $1/(\chi - \chi_0)$ and choosing χ_0 in such a way that the function is linear for a temperature range as large as possible. This procedure yields $\chi_0 = -5 \cdot 10^{-6}$ erg/molG. A negative value of χ_0 hints at contributions due to diamagnetism which is present in all materials [24]. A subsequent fit in the temperature range from 250 to 300 K gives $C = 0.48(1)\,\text{ergK}/(\text{molG}^2)$ and $\Theta = -4.5(4)\,\text{K}$. The negative Weiss temperature implies a predominance of antiferromagnetic correlations.

The Curie constant is defined as [24]

$$C = \frac{N_A \mu_{eff}^2}{3 k_B} \tag{5.2}$$

with the Avogadro and Boltzmann constants N_A and k_B, respectively. The effective magnetic moment is defined as $\mu_{eff} = g_J \mu_B \sqrt{J(J+1)}$, g_J is the Landé g-factor and μ_B the Bohr magneton [18]. Assuming a quenched angular orbital momentum $L = 0$, $S = 1/2$ for $PbCuSeO_4(OH)_2$, the high temperature g-factor can be estimated as $g = 2.27(3)$. This agrees with typically measured values of $g = 2.3$ [17].

The Curie-Weiss fit starts to deviate from the recorded data at $T = 50\,\text{K} \approx 10 T_N$

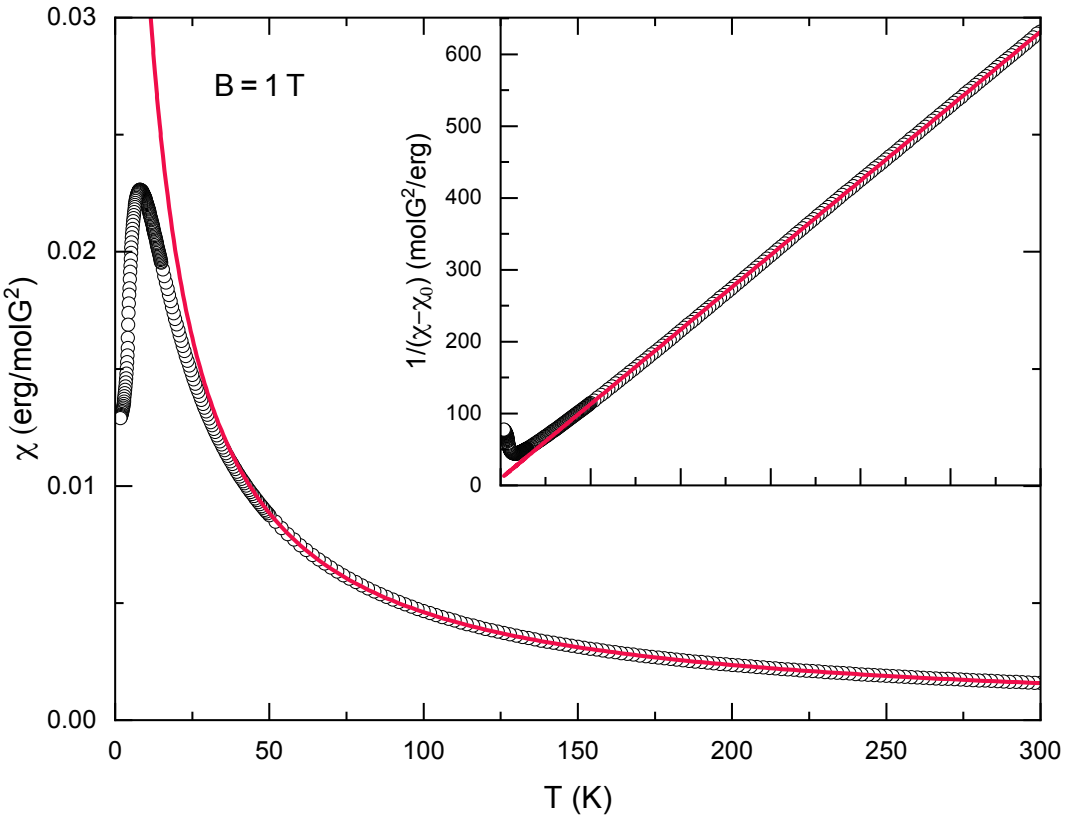


Figure 5.2: Static magnetic susceptibility and inverse susceptibility of $PbCuSeO_4(OH)_2$ (black circles) with a Curie-Weiss fit (red curve) and $\chi_0 = -5 \cdot 10^{-6}$ erg/molG, yielding the Curie constant C=0.48(1) K and Curie-Weiss temperature Θ=−4.5(4) K. Data were recorded by D. Knauer [46], according to a field-cooled protocol with an external field of 1 T.

which implies that short-range correlations become important in the high temperature regime.

The temperature dependence of the static susceptibility reveals a correlation maximum at $T_{\max} = 8.1\,\mathrm{K}$. Figure 5.3 shows Fisher's specific heat $\partial(\chi T)/\partial T$ up to 20 K. It demonstrates two features, one at $T_{N1} = 4.3\,\mathrm{K}$ and a weaker one at $T_{N2} = 4.8\,\mathrm{K}$ which hint at phase transitions to ordered states.

With the given values of the Weiss temperature as well as the ordering temperature, the frustration parameter of the compound can be estimated as [47]

$$f = \frac{|\Theta|}{T_N} \approx 1 \tag{5.3}$$

which either implies a non-frustrated system or e.g. competing interactions with opposite signs incidentally leading to a small value of $\Theta = \sum_i J_i$.

Isothermal magnetisation was measured in [45] and [46] at 2 K. In both cases its

derivative $\partial M/\partial B$, also referred to as magnetic susceptibility, shows a kink at 2.8 T which was interpreted as a spin-flop transition in [45]. The sample was also studied in pulsed magnetic fields, revealing the saturation magnetisation of $M_{\mathrm{sat}} \approx 1\mu_{\mathrm{B}}$ at $B_{\mathrm{sat}} \approx 19\,\mathrm{T}$ [43].

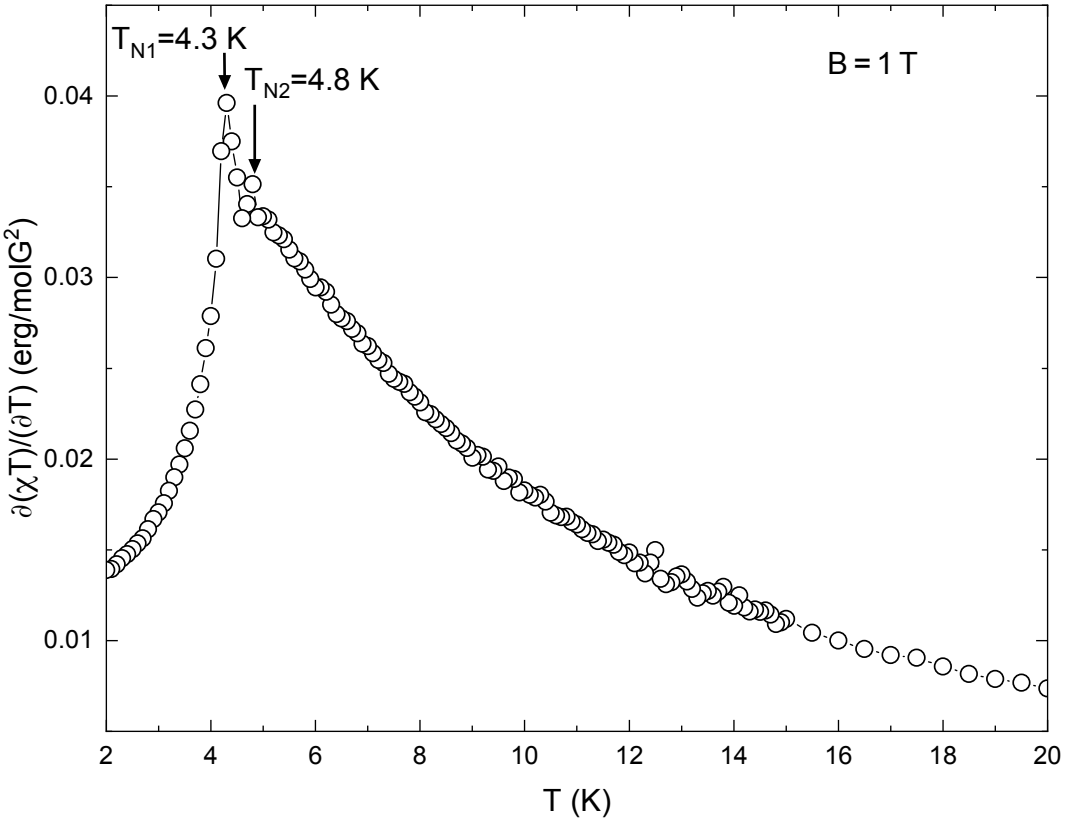


Figure 5.3: Fisher's specific heat $\partial(\chi T)/\partial T$ of $PbCuSeO_4(OH)_2$ obtained from data displayed in fig. 5.2. The measurement of the susceptibility, following a field-cooled protocol, were performed by D. Knauer [46].

5.3 X-Band ESR Measurements and Analysis

In this section results from X-band ESR measurements are presented. Spectra were recorded for 23 temperatures ranging from 5 to 200 K at 9.63 GHz microwave frequency in a Faraday configuration with the external magnetic field swept from 50 to 8050 G. From a fit to the resonance lines the intensity, resonance field and linewidth can be extracted. Examining the temperature dependence of these parameter gives insights to the correlation effects present in the paramagnetic regime of the compound.

Most samples investigated in a X-band ESR device produce a Lorentzian signal and

their absorption can be written as

$$A(B) = I \frac{\Delta B}{4\left(B - B_{\mathrm{res}}\right)^2 + \Delta B^2} \tag{5.4}$$

with intensity I, resonance field B_{res} and FWHM linewidth ΔB. The ESR signal follows the Lorentzian shape in the magnetic field range $B = B_{\mathrm{res}} \pm a$ with $a > \Delta B/2$. It is especially important that the measured spectra and theoretically predicted spectra agree well in this field region to get reliable information about the investigated material. Outside this field range the detected spectra resemble a Gaussian or exponential function and simulations may not necessarily have to agree perfectly with the measurement [48]. Due to several effects that depend on the skin depth of the sample and linewidth of the resonance signal, it is possible that the transmitted signal is an admixture of absorption A and dispersion D. This so-called phase mixing must be corrected because it changes the lineshape as well as the position of the resonance field and therefore the g-factor which is a crucial property obtained from ESR experiments [49, 50]. To account for phase mixing, the power absorbed by the sample from a magnetic microwave field as a function of the static field B is written as a linear combination of absorption and dispersion [51]

$$P(B) = \frac{1}{\sqrt{1+\phi^2}} \left[A(B) + \phi D(B)\right] \tag{5.5}$$

where the mixing parameter $0 \leq \phi \leq 1$ describes the fraction of dispersion added to the absorption. $\phi = 0$ represents symmetric spectra without phase mixing, while $\phi = 1$ denotes strongly phase mixed signals leading to asymmetric spectra. The inverse square root is needed for normalization [51]. Absorption and dispersion are connected via the Kramers-Kronig relations, yielding [52]

$$D(B) = -\frac{1}{\pi}\mathcal{P}\int_{-\infty}^{\infty} \frac{A(B')}{B' - B}\mathrm{d}B' = 2I\left(\frac{B - B_{\mathrm{res}}}{4(B - B_{\mathrm{res}})^2 + \Delta B_i^2}\right) \tag{5.6}$$

where the Cauchy principal value $\mathcal{P}$ denotes that only the principal part of the integral is considered. To improve the signal-to-noise ratio it is not the absorbed power but its derivative that is recorded during the experiment [53]. Furthermore, some materials may have an anisotropic g-factor or several magnetic sites, resulting in a complex spectrum for which more than one resonance line is required to describe it completely. Taking these considerations into account we arrive at [49, 51]

$$\left(\frac{\mathrm{d}P}{\mathrm{d}B}\right)_{\mathrm{tot}} = \sum_i \frac{1}{\sqrt{1+\phi_i^2}} \left[A_i'(B) + \phi_i D_i'(B)\right] = \sum_i \left(\frac{\mathrm{d}P}{\mathrm{d}B}\right)_i \tag{5.7}$$

where we sum over all resonance features i.

The recorded spectra of $PbCuSeO_4(OH)_2$ are very broad (see fig. 5.4), implying that the linewidth and resonance field are in the same order of magnitude. Therefore, it is

necessary to consider both circular components of the linearly polarized microwave magnetic field resulting in a Lorentzian absorption that also includes a resonance at reversed magnetic field $B = -B_{\mathrm{res}}$. This is considered by an additional term in the absorption [48, 53]

$$A_i(B) = I_i \left(\frac{\Delta B_i}{4(B - B_{\mathrm{res},i})^2 + \Delta B_i^2} + \frac{\Delta B_i}{4(B + B_{\mathrm{res},i})^2 + \Delta B_i^2} \right) \tag{5.8}$$

and dispersion [48]

$$D_i(B) = 2I_i \left(\frac{B - B_{\mathrm{res},i}}{4(B - B_{\mathrm{res},i})^2 + \Delta B_i^2} + \frac{B + B_{\mathrm{res},i}}{4(B + B_{\mathrm{res},i})^2 + \Delta B_i^2} \right) \tag{5.9}$$

where intensity I_i, resonance field $B_{\mathrm{res},i}$ and FWHM linewidth ΔB_i have to be determined. The subscript i denotes the corresponding resonance feature L_i.

Inserting eqs. (5.8) and (5.9) in eq. (5.7) the derivative of the power absorbed reads

$$\begin{aligned} \left(\frac{\mathrm{d}P}{\mathrm{d}B} \right)_i = \frac{2I_i}{\sqrt{1+\phi_i^2}} \Bigg[& \frac{-4\Delta B_i \left(B - B_{\mathrm{res},i}\right) + \phi_i \left(\Delta B_i^2 - 4 \left(B - B_{\mathrm{res},i}\right)^2 \right)}{\left(4 \left(B - B_{\mathrm{res},i}\right)^2 + \Delta B_i^2 \right)^2} \\ & + \frac{-4\Delta B_i \left(B + B_{\mathrm{res},i}\right) + \phi_i \left(\Delta B_i^2 - 4 \left(B + B_{\mathrm{res},i}\right)^2 \right)}{\left(4 \left(B + B_{\mathrm{res},i}\right)^2 + \Delta B_i^2 \right)^2} \Bigg]. \end{aligned} \tag{5.10}$$

Finally, including a linear background correction of the recorded spectra, the measured power absorbed by the sample reads

$$\left(\frac{\mathrm{d}P}{\mathrm{d}B} \right)_{\mathrm{measured}} = \sum_i \left(\frac{\mathrm{d}P}{\mathrm{d}B} \right)_i + c_1 B + c2. \tag{5.11}$$

This is the function used to fit the experimental data. The field range for which the fits are performed is adjusted in such a way that the distance from the start of the fit to the field position of the maximally absorbed power equals the distance from the field position of the minimum of the power absorbed to the end of the fitting range. By doing so, the aim is to obtain more reliable results from spectra with a broad linewidth. In the following, various fitting procedures including one and two resonance features with different numbers of parameters will be discussed.

At first glance, the recorded spectra look as if they can be well described by one symmetric Lorentzian without phase mixing. Having a look at fig. 5.4 reveals that this is not the case. It shows X-band spectra recorded at 5 K, 81 K and 201 K together with different fit curves using one Lorentzian feature. The dashed lines represent the magnetic field range in which experimental data are predicted to follow a Lorentzian lineshape ($B = B_{\mathrm{res}} \pm \Delta B/2$) and therefore should agree well with the simulations. The different fit curves are

- one symmetric Lorentzian without any background or phase correction:

$$\text{Fit } 1 = L_{1,\text{sym}} = \frac{\mathrm{d}A_1}{\mathrm{d}B} \tag{5.12}$$

- one symmetric Lorentzian with a constant offset:

$$\text{Fit } 2 = L_{1,\text{sym}} + c_2 = \frac{\mathrm{d}A_1}{\mathrm{d}B} + c2 \tag{5.13}$$

- one asymmetric Lorentzian with phase mixing but no background correction:

$$\text{Fit } 3 = L_{1,\text{pm}} = \frac{1}{\sqrt{1+\phi_1^2}}\left[\frac{\mathrm{d}A_1}{\mathrm{d}B} + \phi_1 \frac{\mathrm{d}D_1}{\mathrm{d}B}\right] \tag{5.14}$$

- one asymmetric Lorentzian with phase mixing and background correction in form of a constant offset:

$$\text{Fit } 4 = L_{1,\text{pm}} + c_2 = \frac{1}{\sqrt{1+\phi_1^2}}\left[\frac{\mathrm{d}A_1}{\mathrm{d}B} + \phi_1 \frac{\mathrm{d}D_1}{\mathrm{d}B}\right] + c2. \tag{5.15}$$

For all three temperatures it is noticeable that Fit 1 and Fit 3 are congruent and therefore Fit 3 cannot be seen. Especially emphasized in plots (b) and (c), it can be seen that Fit 1 yields a Lorentzian lineshape that overestimates the absorbed power. A similar behaviour is found for $T = 5\,\text{K}$ in plot (a), even though it is not as clearly visible because of the higher signal intensity. Using Fit 2 to fit the spectra leads to better results for all three temperatures. Following from this, it is important to include the offset $c_2 \approx -0.4$. It probably originates from internal effects and the measuring technique in the X-band device. Now, by also including phase correction via Fit 4 the fitting improves. This can be seen nicely in the insets representing the simulation together with its components $\mathrm{L_{1,pm}}$ and $\mathrm{c_2}$. The best agreement between measured spectrum and fitted curve is obtained for 81 K with a deviation between data and Fit 4 by approximately 4 %. Fit 4 deviates from the recorded spectrum at 5 K by less than 10 % and therefore describes the data acceptably well. At 201 K the deviation between measured data and Fit 4 is more than 20 % which implies that Fit 4 does not describe the lineshape at 201 K sufficiently. Therefore, as a next step, two Lorentzian features are fitted to the detected spectra.

Fitting the experimental data with one resonance feature has led to the conclusion that it is necessary to include a constant background. Accordingly, the different fit curves for two resonance features all consider an offset. More specifically, the considered fit curves are

- two symmetric Lorentzians with a constant offset:

$$\text{Fit } 5 = L_{(2,1),\text{sym}} + L_{(2,2),\text{sym}} + c_2 = \frac{\mathrm{d}A_1}{\mathrm{d}B} + \frac{\mathrm{d}A_2}{\mathrm{d}B} + c_2 \tag{5.16}$$

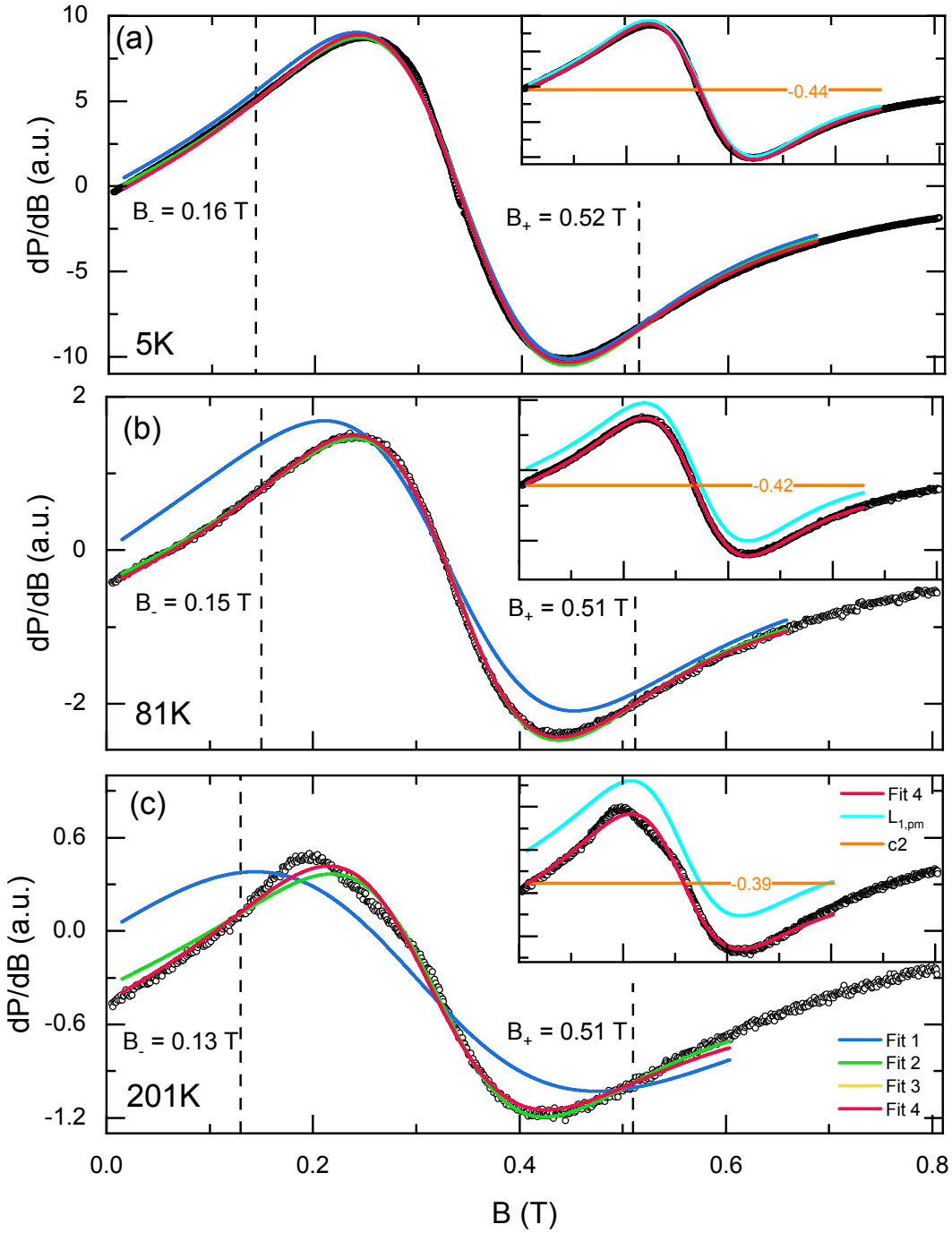


Figure 5.4: Experimental data from X-band ESR measurements of $PbCuSeO_4(OH)_2$ for (a) 5 K, (b) 81 K and (c) 201 K and comparison of different fits with one resonance feature. The dashed lines highlight the field range in which fitted curves and recorded spectra should agree well. Insets show the best fit curve obtained from Fit 4 and its individual components $L_{1,pm}$ and c_2.

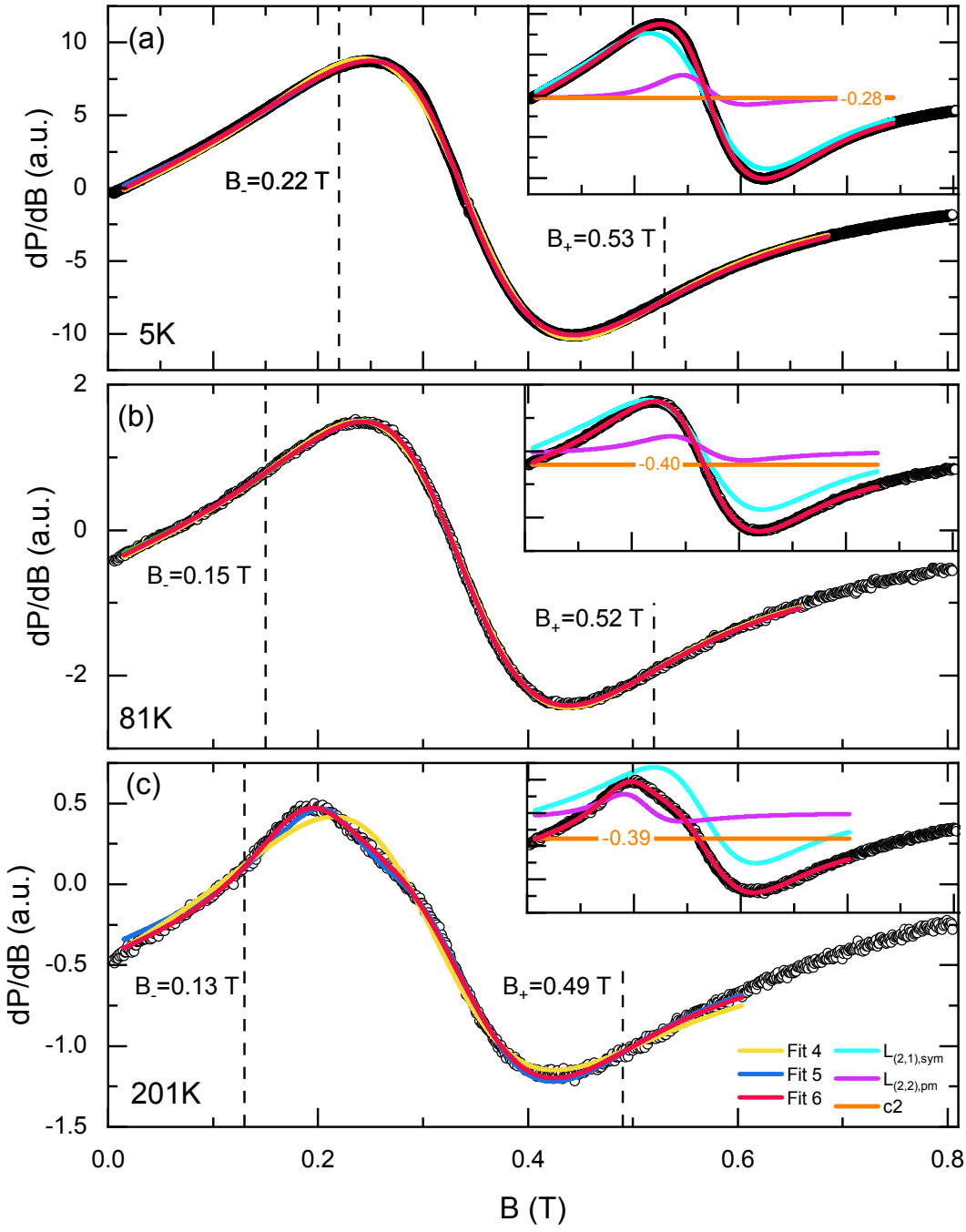


Figure 5.5: Experimental data from X-band ESR measurements of $PbCuSeO_4(OH)_2$ for (a) 5 K, (b) 81 K and (c) 201 K together with a comparison of different fits with two resonance features, obtained from Fit 5 and Fit 6. The dashed lines highlight the field range in which fitted curves and recorded spectra should agree well. Insets show the best fit curve Fit 6 and its individual components $L_{(2,1),sym}$, $L_{(2,2),pm}$, c_2.

- one symmetric Lorentzian feature and one asymmetric Lorentzian feature with an offset:

$$\begin{aligned} \text{Fit } 6 &= L_{(2,1),\text{sym}} + L_{(2,2),\text{pm}} + c_2 \\ &= \frac{\mathrm{d}A_1}{\mathrm{d}B} + \frac{1}{\sqrt{1+\phi_2^2}}\left[\frac{\mathrm{d}A_2}{\mathrm{d}B} + \phi_2 \frac{\mathrm{d}D_2}{\mathrm{d}B}\right] + c2. \end{aligned} \tag{5.17}$$

For 5 K and 81 K in fig. 5.5 (a) and (b) the contribution of phase mixing is very small. Hence, Fit 5 (blue) is almost covered completely by Fit 6 (red). At 201 K phase mixing is more important and Fit 6 provides a better simulation of the spectrum than Fit 5. The dashed lines represent the field range in which fited curves and recorded spectra should agree well. This is obeyed at all three temperatures in fig. 5.5. Spectra at 5 K and 81 K can even be described well by the fitted curves over the entire fit range. The deviation of Fit 4 from the recorded spectra is approximately 4 % at 5 K, 81 K and 201 K. This is a great improvement for the lineshape at 201 K. The yellow line depicts the fit curve obtained from Fit 4, yielding the best fit results when considering one resonance feature. In plots (a) and (b) it is barely visible since it is almost completely covered by Fit 6, encouraging the conclusion that recorded spectra at these temperatures can be described by one resonance feature. The insets show the best fit result when considering two resonance features, obtained from Fit 6, for each temperature together with the individual components of the fit. It is noteworthy that the intensity of the second resonance feature is significantly lower than that of the first resonance for all three temperatures.

Figure 5.6 shows a comparison of the best fit results when including one and two resonance features, namely Fit 4 and Fit 6. Fit 4 is almost completely covered by Fit 6 for temperatures between $T = 5\,\text{K}$ and $T = 102\,\text{K}$ while the two fit curves start to mismatch at $T \geq 132\,\text{K}$, with Fit 6 being in better agreement with the measured spectra. This supports the conclusion that Fit 4 is a reasonable fit option to describe the recorded spectra up to $T = 102\,\text{K}$ but more resonance features need to be considered to describe high temperature data to an acceptable level.

Fitting three Lorentzian features would have required four additional fit parameters, yielding in total 13 fit parameters to be determined by fitting the experimental data. It is already difficult to find reasonable parameters for the lower dimensional fit considering two Lorentzian features with 10 fit parameters. Therefore, it was refrained from accounting for three distinct resonance signals in the spectra.

The temperature dependence of the fit parameters for Fit 4 and for Fit 6 is summarised in fig. 5.7. L_1 (blue circles) describes the fit parameters of one resonance signal obtained from Fit 4 whereas $\text{L}_{2,1}$ and $\text{L}_{2,2}$ represent the parameters of the first and second absorption signal, respectively, considered in Fit 6. It should be noted that results from Fit 4 are not reliable for $T > 132\,\text{K}$ because the recorded spectra cannot be described sufficiently well for these temperatures with one absorption peak, as shown in fig. 5.6. This is indicated by empty symbols for this temperature range.

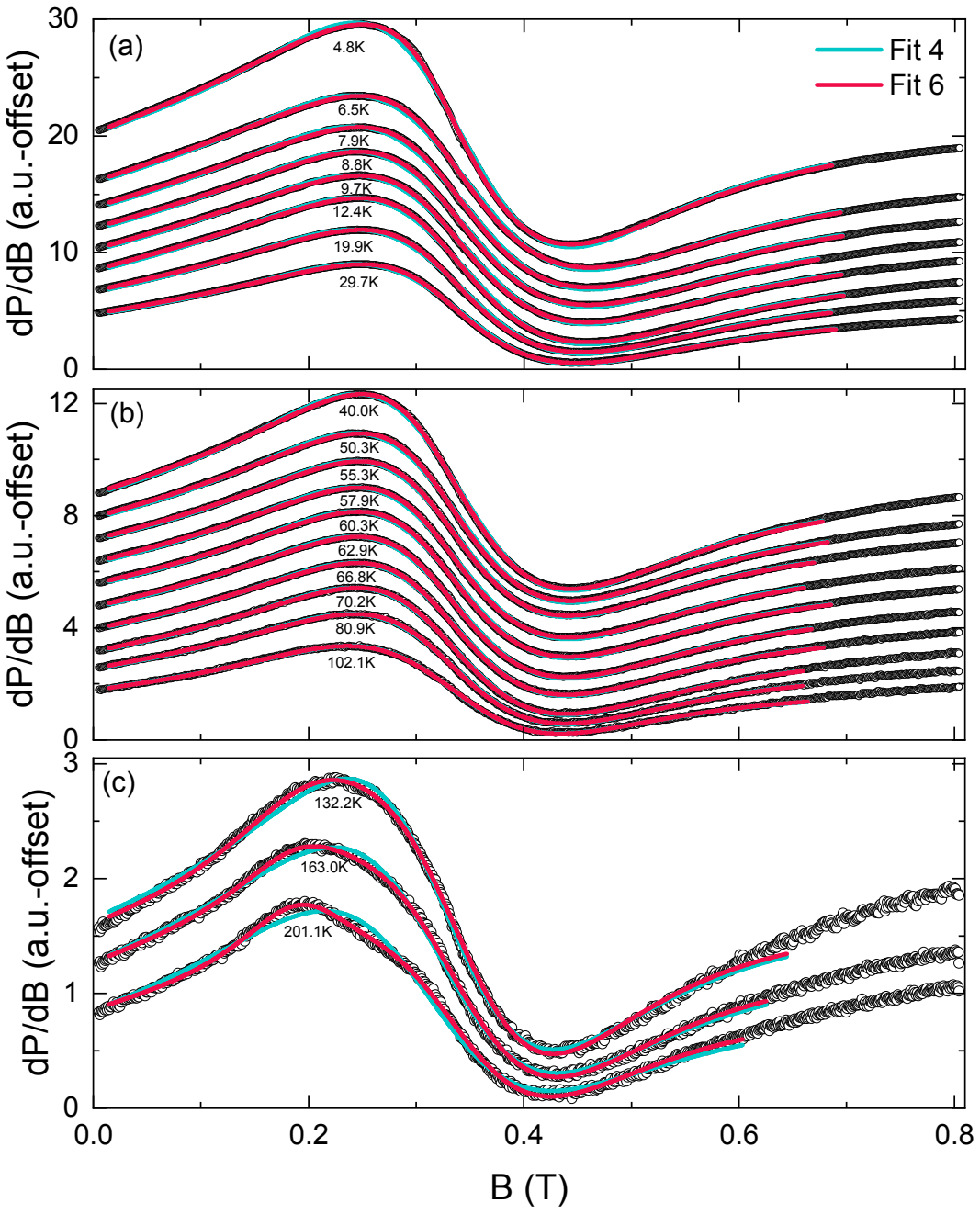


Figure 5.6: Experimental data from X-band ESR measurements on $PbCuSeO_4(OH)_2$ for all recorded temperatures (black circles) together with two different fit curves. Fit 4 represents one asymmetric Lorentzian feature with a constant offset while Fit 6 represents one symmetric and one asymmetric Lorentzian combined with a constant offset.

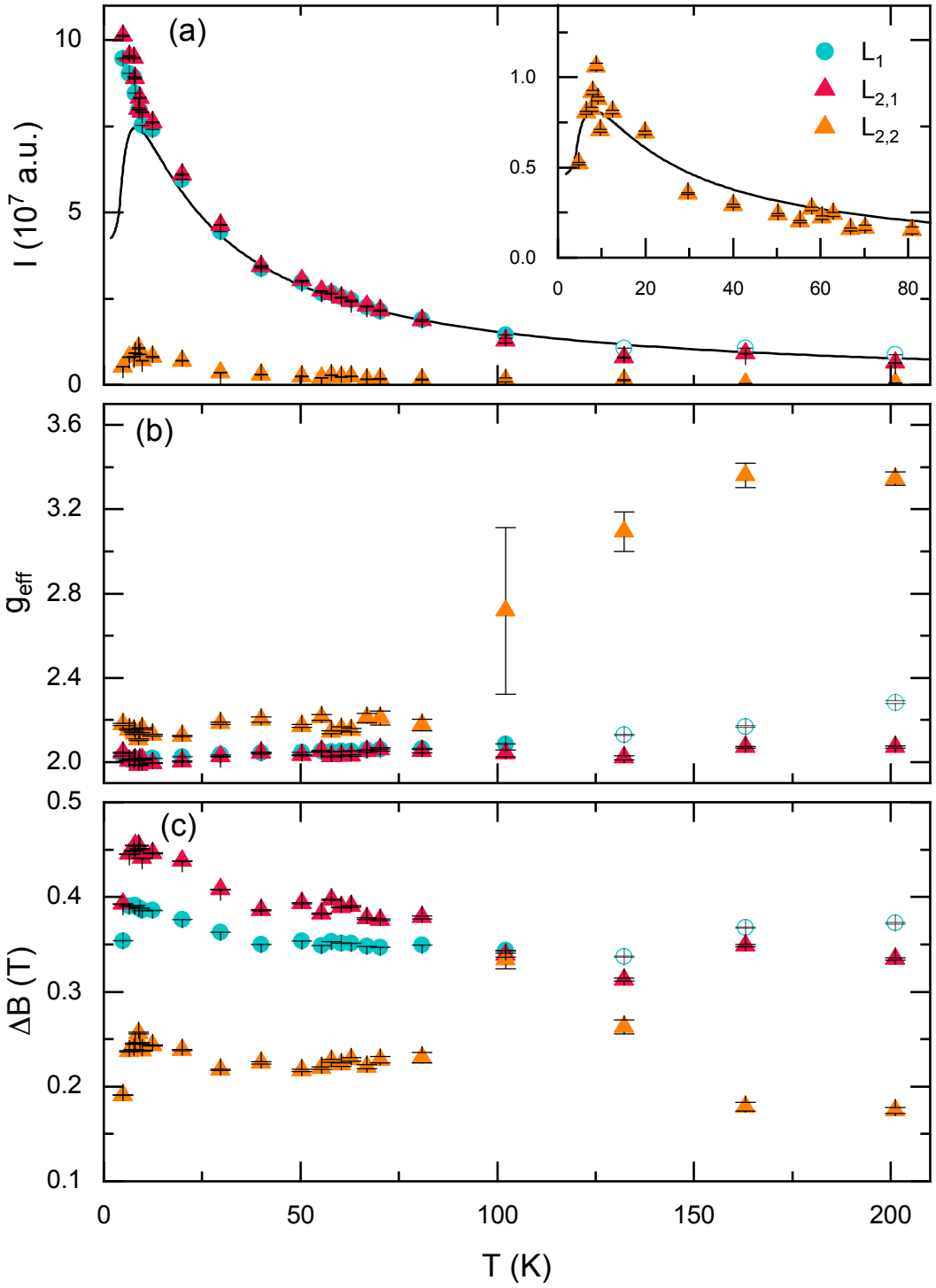


Figure 5.7: Comparison of the temperature dependence of the intensity, effective g-factor and linewidth in $PbCuSeO_4(OH)_2$ obtained by analysing X-band ESR data by means of the two different models Fit 4 and Fit 6. Blue circles L_1 describe the single resonance line of Fit 4 while red and orange triangles correspond to Fit 6. $L_{2,1}$ (red) and $L_{2,2}$ (orange) represent the parameters of the first and second absorption signal, respectively. The solid black line in (a) demonstrates the static susceptibility scaled to the intensity of the corresponding resonance features. The solid black line in (a) demonstrates the static susceptibility scaled to the intensity of the corresponding resonance features.

The intensity, which corresponds to the dynamic susceptibility χ_{ESR}, follows the same behaviour for L_1 and $L_{2,1}$: starting at $T = 5\,\mathrm{K}$ it decreases exponentially with increasing temperatures. $L_{2,2}$ has a much lower intensity, which has already been noted in fig. 5.5. In the inset its temperature dependence can be observed more closely: it shows a correlation maximum at $T \approx 9\,\mathrm{K}$. The intensity for both resonance features $L_{2,1}$ and $L_{2,2}$ can be scaled to the static susceptibility χ_{static} obtained from magnetisation measurements [46]. χ_{static} scaled to χ_{ESR} of L_1 is not shown as χ_{ESR} of L_1 and $L_{2,1}$ is almost the same. χ_{static} coincides well with χ_{ESR} of $L_{2,1}$ for temperatures above 20 K. For $L_{2,2}$ the static and dynamic susceptibility agree up to 80 K, as shown in the inset of fig. 5.7. While χ_{ESR} of $L_{2,2}$ agrees with χ_{static} also for lower temperatures, $L_{2,1}$ does not show a correlation maximum in χ_{ESR}. The consistency of the dynamic and static susceptibility for $T > 20\,\mathrm{K}$ implies that the compound is paramagnetic for high temperatures. The correlation maximum in χ_{ESR} of $L_{2,2}$ and its coinciding with the static susceptibility hint at a phase transition to an antiferromagnetically ordered state. The development of such an ordered state cannot be observed in χ_{ESR} of $L_{2,1}$.

The effective g-factor can be determined as

$$g = \frac{f\,[\mathrm{GHz}]}{13.996 B_{\mathrm{res}}\,[\mathrm{T}]} \tag{5.18}$$

from the resonance field B_{res}. It is approximately constant at $g_1 \approx g_{2,1} \approx 2.02$ for L_1 and for $L_{2,1}$. For $L_{2,2}$ it is approximately constant with $g_{2,2} \approx 2.2$ for temperatures below 100 K. These values differ from the components of the g-factor along the b- and c-axis of the single crystal sample of linarite where $g_b = 2.10$ and $g_c = 2.28$ were found [13, 14]. The third value of the anisotropic g-factor of linarite, $g_a = 2.34$ along the a-axis, was not detected for $PbCuSeO_4(OH)_2$. This indicates that the compound has octahedral symmetry instead of tetragonal symmetry as observed for its structural analog $PbCuSO_4(OH)_2$. Typical paramagnetic g-factors for Cu^{2+} in octrahedral crystal fields are [17]

$$\begin{aligned} g_{\parallel} &= 2 - \frac{8\lambda}{\Delta_0} \sim 2.1 \\ g_{\perp} &= 2 - \frac{2\lambda}{\Delta_1} \sim 2.4 \end{aligned} \tag{5.19}$$

with the spin-orbit parameter λ and the crystal field splittings Δ_0, Δ_1. The results of the g-factor of $PbCuSeO_4(OH)_2$ found by analysing the X-band ESR spectra can be attributed to $g_{2,1} \approx g_{\parallel}$ and $g_{2,2} \approx g_{\perp}$ below 100 K. For higher temperatures the g-factor of $L_{2,2}$ raises to a maximum of $g_2 = 3.36$ at 163.0 K. Such a high g-factor would imply $\lambda/\Delta_1 \sim -0.7$ which is unrealistic for $3d$-electrons that typically have values of $\lambda/\Delta_1 \sim -0.05$ [17]. A shift in the resonance field and thus in the g-factor usually hints at the development of internal magnetic fields in the compound [14]. In this case, with an unphysically high g-value, it is questionable whether the fit yields correct values for g at $T > 100\,\mathrm{K}$ and the shift of the resonance field cannot be

interpreted as internal magnetic fields developing. The second peak is clearly visible in the data above 160 K but its interpretation remains open.

The temperature dependence of the linewidth is shown in fig. 5.7 (c). All resonance features show the same behaviour for $T \leq 81\,\mathrm{K}$ with ΔB approximately constant for temperatures between 81 and 40 K. In this temperature range, L_1 has linewidth $\Delta B_1 \approx 0.35\,\mathrm{T}$, $L_{2,1}$ demonstrates $\Delta B_{2,1} \approx 0.4\,\mathrm{T}$ while $L_{2,2}$ has the smallest linewidth with $\Delta B_{2,2} \approx 0.2\,\mathrm{T}$. In the high temperature regime, the linewidth of the resonance signals in linarite is $\Delta B_{B\|b} \approx 0.1\,\mathrm{T}$ for fields applied along the b-axis and $\Delta B_{B\|a,c} \approx 0.7\,\mathrm{T}$ for fields parallel to the a- and c-axis [13]. The linewidth for fields applied along the a- and c-axis in linarite is larger than the linewidth in $PbCuSeO_4(OH)_2$. Nevertheless, the values are in the same order of magnitude.

Upon cooling, the linewidth increases slightly until it reaches its maximum at $T \approx 8\,\mathrm{K}$. This maximum is highest for $L_{2,1}$ with $\Delta B_{2,1} \approx 0.45\,\mathrm{T}$. The linewidth resulting from Fit 4 has a lower maximum with $\Delta B_1 \approx 0.39\,\mathrm{T}$ while $L_{2,2}$ has the smallest maximum at $\Delta B_{2,2} \approx 0.26\,\mathrm{T}$. Below 8 K, ΔB decreases again implying that a critical broadening of the linewidth, as expected for $T \to T_N$ and observed in [13, 14] for linarite, does not occur in $PbCuSeO_4(OH)_2$ for any of the fitting procedures. The critical broadening of the linewidth can be associated with the evolution of spin-spin correlations [41]. The absence of this critical behaviour could suggest that a resonance field of $B_{\mathrm{res}} \approx 0.4\,\mathrm{T}$ might be strong enough to suppress spin-spin correlations.

Another possibility to interpret the low temperature behaviour is that the system is already in its ordered phase, i.e. the actual sample temperature differs from the thermometer's one. Note that the experimental device faced a miscalibration of the thermometer well after the measurement and analysis of the recorded data. Therefore, it cannot be completely ruled out that the sample temperature presented here differs from the actual sample temperature.

Above 80 K the linewidth behaves differently for all resonance features. ΔB_1 stays approximately constant with a slight increase towards high temperatures. $\Delta B_{2,1}$ has a minimum at 163 K with $\Delta B_{2,1min} = 0.31\,\mathrm{T}$. $L_{2,2}$ has a maximum at 102 K with $\Delta B_{2,2max} = 0.33\,\mathrm{T}$ before it drops to $\Delta B_{2,2min} = 0.17\,\mathrm{T}$ at 200 K. The deviations in the temperature dependence of the linewidth occur at the same temperature at which g_2 starts to increase towards unphysically high values. Therefore, obtained fit parameters for $T \geq 102\,\mathrm{K}$ are not reliable for $L_{2,2}$. Furthermore, the g-factor and the linewidth of L_1 must be taken cautiously at the temperatures for which Fit 4, considering a single Lorentzian derivative, deviates from the recorded spectra because a second absorption peak must be included at $T > 130\,\mathrm{K}$.

In general, the linewidth of the resonance signals in $PbCuSeO_4(OH)_2$ is quite large, ranging from $\Delta B_{min} = 0.17\,\mathrm{T}$ for $L_{2,2}$ to $\Delta B_{max} = 0.45\,\mathrm{T}$ for $L_{2,1}$. Due to the limited field range, the X-band measurement cannot capture the complete ESR signal over the entire temperature range because the dominant absorption feature $L_{2,1}$ with $\Delta B \geq 0.31\,\mathrm{T}$ is too broad. This led to problems in the analysis of the recorded spectra, especially the background correction was found to be difficult and thus it cannot

be ensured that the position of the resonance field and the value of the linewidth are trustworthy. Consequently, it is necessary to study this compound in a HF-ESR setup which can sweep to magnetic fields far above 1 T. Another advantage of using HF-ESR is that anisotropic g-factors in high frequencies result in well separated resonance fields in contrast to low frequencies for which the resonance fields are close to each other and therefore hard to resolve. A second possibility to improve measurement results could be obtained by probing a single crystal. This would reduce the number of resonance features detected in the spectrum since a measurement would be restricted to a certain crystal axis depending on the orientation of the sample.

6 Summary

In this thesis, powder samples of two antiferromagnetic quantum spin chains were investigated by the application of high-frequency and X-band electron spin resonance spectroscopy as well as static magnetisation measurements. Both compounds, the spin-1 chain $Sr_2Ni(SeO_3)_2Cl_2$ and the spin-1/2 chain $PbCuSeO_4(OH)_2$, are very recently synthesised samples. Therefore, only few published experimental data are available so far and not much information about the physical properties of the two systems is known.

The first compound investigated is the $S = 1$ chain system $Sr_2Ni(SeO_3)_2Cl_2$. The temperature dependence of the static susceptibility measured at $B = 1\,\mathrm{T}$ reveals the development of an antiferromagnetically ordered state at $T_N = 6\,\mathrm{K}$. Measurements of the isothermal magnetisation at 2 and 3 K demonstrate a spin-flop transition at $B_{c1} = 8.4\,\mathrm{T}$. The observed ordering temperature T_N agrees with the previously reported value in [10], while the critical field B_{c1} is lower than the published value.

HF-ESR measurements were performed in a frequency range from 40 to 800 GHz. The frequency vs. field diagram was constructed from observed resonance features in the recorded spectra. The observed antiferromagnetic resonances were analysed by means of different two-sublattice AFM models with uniaxial and orthorhombic anisotropies, yielding distinct values for the axial and transverse anisotropy D and E, respectively: unixial anisotropy (Model 1) with $D = 3.8(1)\,\mathrm{K}$, orthorhombic anisotropy with $D = 7.2(3)\,\mathrm{K} \approx E = 2.2(3)\,\mathrm{K}$ in the same order of magnitude (Model 2) and orthorhombic anisotropy with $D = 5.10(4)\,\mathrm{K} \gg E = 0.55(4)\,\mathrm{K}$ (Model 3).

After comparing the three models, the second model can be excluded as it does not describe the measured resonance features reasonably well. Moreover, Model 2 predicts resonance signals at frequencies higher than 500 GHz where measurements were performed but no absorption was detected. Model 1 and Model 3 both describe the phase diagram to a very good degree even though the assumed anisotropy is a different one. The uniaxial anisotropy in Model 1 assumes one zero-field splitting gap of $\Delta = 272(2)\,\mathrm{GHz}$. In contrast, the orthorhombic anisotropy in Model 3 involves two zero-field splitting gaps $\Delta_1 = 258(3)\,\mathrm{GHz}$ and $\Delta_2 = 286(4)\,\mathrm{GHz}$. According to this model, there are two resonance branches near to this model, one for magnetic fields along the second-easy axis and one for fields parallel to the hard axis, with a similar field dependence. The resonance signals assigned to these branches appear at magnetic fields with less than 1 T difference at the same frequency and are therefore very hard to resolve experimentally. In the uniaxial case these branches are degenerate since the second-easy and hard axis are equivalent and there is only a distinction between fields along the easy axis and the axis perpendicular to the easy axis. This

explains why both Model 1 and Model 3 describe the frequency vs. field diagram reasonably well despite the different magnetic anisotropies assumed.

Model 1 and Model 3 both yield an isotropic g-value which amounts to 2.10(1) for Model 1 and 2.07(1) for Model 3. This agrees with the high temperature value $g_{\mathrm{Curie}} = 2.2(1)$ obtained from a Curie-Weiss fit of the static magnetic susceptibility $\chi(T)$. Isotropic g-values are typical for Ni^{2+} ions in a slightly distorted octahedral crystal field [36] but $g \approx 2.1$ is lower than usually measured values around 2.2 for Ni^{2+} ions [30].

The parameter $\alpha = 1 - \chi_{\parallel}/\chi_{\perp}$ is found to be $\alpha = 0.38(4)$ for Model 1 and $\alpha = 0.40(4)$ for Model 3. This implies $\chi_{\parallel} \neq 0$, different from what is expected for a perfect antiferromagnet at zero temperature, and suggests significant thermal or quantum fluctuations at 2 K.

A theoretical prediction of the resonance branches with $\alpha = 0.4$ and D, E and J based on magnetisation features detected in [10] provides a good description of the field dependence of the resonance branches. This emphasises the importance of thermal and quantum fluctuations in the system and supports the validity of Model 3.

The measured temperature dependence of resonance signals at the fixed frequency $f = 213.8\,\mathrm{GHz}$ confirms that the recorded absorption features are antiferromagnetic resonances because they vanish at the ordering temperature $T_N = 6\,\mathrm{K}$. In the paramagnetic regime above T_N, the g-factor shows a shift of its value up to $T = 50\,\mathrm{K}$. This indicates the development of internal fields and a contribution of short-range spin correlations. Above 50 K, the g-factor is approximately constant at $g = 2.31(1)$. The linewidth demonstrates critical broadening behaviour for $T \to T_N$ upon cooling. This suggests the evolution of spin-spin correlations and the presence of AFM fluctuations. For $T \geq 50\,\mathrm{K}$, the linewidth does not show significant temperature dependence which coincides with the constant g-value in this temperature range.

The second material investigated is the $S = 1/2$ chain $PbCuSeO_4(OH)_2$. Measurements of the isothermal magnetisation $M(B)$ and the static susceptibility $\chi(T)$ [46] reveal a spin-flop field at $B_{\mathrm{SF}} = 2.8\,\mathrm{T}$ and two transition temperatures at $T_{N1} = 4.3\,\mathrm{K}$ and $T_{N2} = 4.8\,\mathrm{K}$. Both values agree with measurement results from our collaborators [45].

The fixed powder sample was studied by X-band ESR at temperatures between 5 and 200 K. The recorded spectra were fitted with six different functions. The fit function considering one asymmetric Lorentzian feature with constant background (Fit 4) was found to give the best result for $T < 130\,\mathrm{K}$ while Fit 6, including one symmetric and one asymmetric absorption signal with constant background, is required to describe the recorded spectra at $T > 130\,\mathrm{K}$ appropriately. Only parameters at $T < 100\,\mathrm{K}$ are considered trustworthy because Fit 4 can only be used for $T < 130\,\mathrm{K}$ and Fit 6 yields an unrealistic g-value for the second resonance with $g > 3$ at temperatures above 100 K.

The single resonance line L_1 in Fit 4 demonstrates a temperature dependence of the

intensity which follows a Curie-Weiss law for high temperatures but does not show a correlation maximum as expected from susceptibility measurements. The effective g-factor is approximately constant over the considered temperature range with a value of $g = 2.02$ which is below the expected value of 2.1 [17]. The temperature independence of the g-factor excludes the development of internal magnetic fields. No critical broadening of the linewidth was observed which is untypical for low dimensional systems approaching the ordering temperature. Instead, the linewidth increases slightly from 30 to 8 K which suggests the development of short-range correlations in this temperature range.

Considering two resonance features $L_{2,1}$ and $L_{2,2}$ (Fit 6), does not alter the behaviour of $L_{2,1}$ compared to L_1. Only the linewidth is shifted to lower values but its temperature dependence is qualitatively the same. $L_{2,2}$ has a much lower intensity than $L_{2,1}$. It follows a Curie-Weiss law at elevated temperatures and develops a correlation maximum at 9 K, above the ordering temperature. The g-value is determined as $g = 2.2$ which is smaller than the perpendicular component of typically measured values $g_\perp \sim 2.4$. The linewidth of resonance 2 is significantly lower than that of resonance 1 but it shows the same temperature dependence indicating an ordered state above T_N.

In principle, the linewidth of the resonance absorption is too broad to capture the entire signal with X-band ESR spectroscopy measuring at a fixed frequency $f = 9.6$ GHz and at magnetic fields up to 1.2 T. This led to problems in the analysis of the spectra, especially the background correction was found to be difficult. Therefore, the obtained results must be taken cautiously and further investigation of the sample is needed to review the observed temperature dependence of the intensity, the linewidth as well as the g-factor. The analysis can be improved by measurements in the HF-ESR setup with variable frequencies up to 1000 GHz and magnetic fields up to 16 T. These field are large enough to detect the entire resonance signal. Another advantage of HF-ESR is that an anisotropic g-factor can be more easily resolved due to the larger energy difference of the component of the g-factor at high magnetic fields and large microwave frequencies.

In summary, the analysis of the experimental data of $Sr_2Ni(SeO_3)_2Cl_2$ has shown that HF-ESR spectroscopy is a valuable tool to investigate antiferromagnetic resonance modes and determine the magnetic anisotropy parameters of magnetic compounds. Finding orthorhombic anisotropy in the Ni-compound supports the previous classification as a XY-AFM. X-band ESR spectroscopy of $PbCuSeO_4(OH)_2$ revealed information about the development of short-range correlations in the disordered phase. Further investigation by means of HF-ESR spectroscopy is needed to verify the discovered temperature dependence and to establish magnetic anisotropy parameters.

A Appendix

A.1 Analysis of HF-ESR Data of $Sr_2Ni(SeO_3)_2Cl_2$ by means of an Anisotropic g-factor

Model 1: Uniaxial Anisotropy

The fit parameters obtained for a two-sublattice antiferromagnetic model with uniaxial anisotropy (model 1) which considers isotropic as well as anisotropic g-factors are summarised in table A.1. The parameters α and Δ for isotropic and anisotropic g coincide within the error bar. The isotropic g-factor agrees with $g_{\parallel}$ for magnetic fields parallel to the easy axis whereas $g_{\perp}$ for fields perpendicular to the easy axis is slightly larger than g_{iso}.

Model 1	α	Δ_{iso} [T]	g_{iso}	$g_{\parallel}$	$g_{\perp}$
Isotropic g	0.38(4)	9.3(1)	2.10(1)	-	-
Anisotropic g	0.32(4)	9.1(1)	-	2.09(1)	2.13(1)

Table A.1: Model 1: Fit parameters for a two-sublattice AFMR model of $Sr_2Ni(SeO_3)_2Cl_2$ with uniaxial anisotropy.

The obtained resonance branches are represented in fig. A.1 by solid lines for isotropic and by dashed lines for anisotropic g-values. The biggest difference between resonance branches for an isotropic and an anisotropic g-factor is observed for f_{AF^-} and f_{AF^+}. Nevertheless, fitting the recorded resonance features by means of an anisotropic g-factor does not provide a better description of the experimental data.

Model 3: Orthorhombic Anisotropy D $\gg$ E

The fit parameters obtained for a two-sublattice antiferromagnetic model assuming orthorhombic anisotropy with $D \gg E$ (model 3) which considers isotropic as well as anisotropic g-factors are summarised in table A.2. The parameters α, C_1 and C_2 for an isotropic g-factor agree with those for an anisotropic g-value within the error bar. The isotropic g-factor g_{iso} coincides with the three components of the anisotropic g-factor.

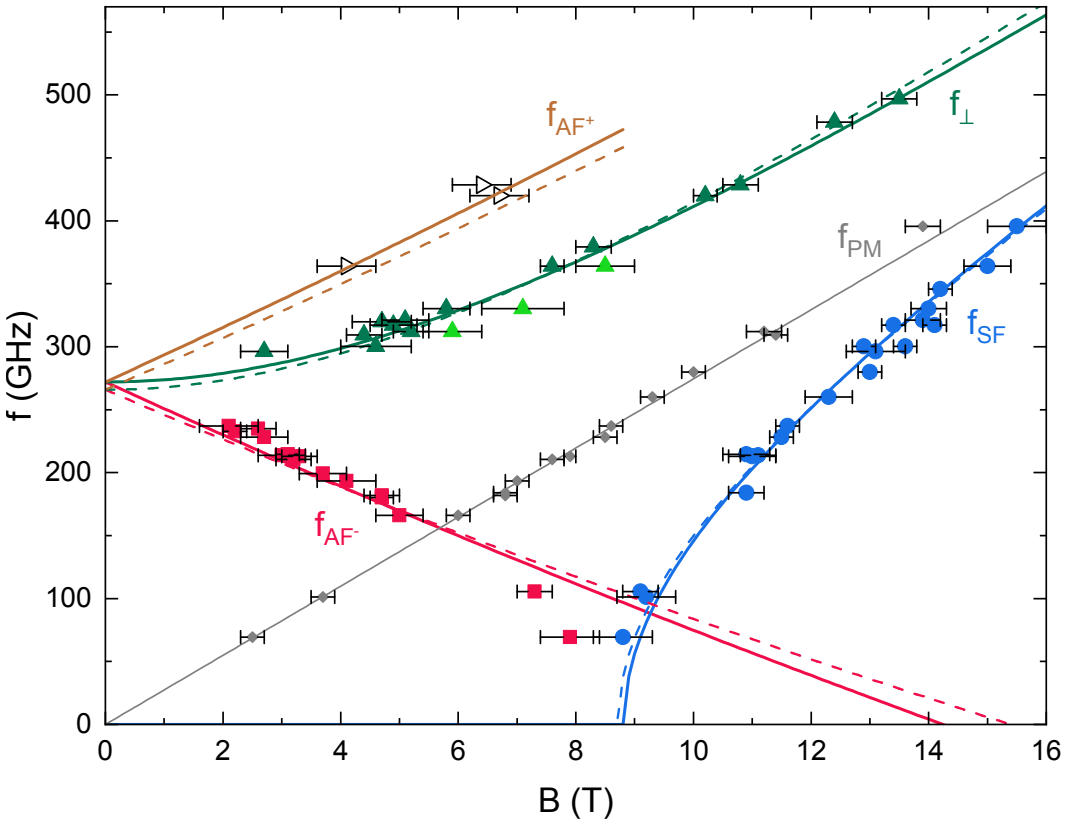


Figure A.1: Model 1: Frequency vs. field diagram of $Sr_2Ni(SeO_3)_2Cl_2$ constructed from HF-ESR data recorded at $T = 2\,\mathrm{K}$. Assuming a two-sublattice AFM with uniaxial anisotropy, the observed branches were attributed to f_{AF^-}, f_{SF} and $f_\perp$. The branch f_{AF^+} is a computed from obtained fit parameters while f_{PM} describes a paramagnetic impurity in the sample.

Model 3	α	C_1 [T^2]	C_2 [T^2]	g_{iso}	g_{easy}	$g_{2^{\mathrm{nd}}\mathrm{easy}}$	g_{hard}
Isotropic	0.40(4)	79(2)	98(3)	2.07(1)	-	-	-
Anisotropic	0.42(5)	79(2)	100(5)	-	2.07(1)	2.07(4)	2.06(2)

Table A.2: Model 3: Fit parameters for a two-sublattice AFMR model of $Sr_2Ni(SeO_3)_2Cl_2$ with orthorhombic anisotropy $D \gg E$.

The obtained resonance branches are represented in fig. A.2 by solid lines for isotropic and by dashed lines for anisotropic g-values. The biggest difference between resonance branches for an isotropic and an anisotropic g-factor is observed for f_{AF^-} and f_{AF^+} whereas the resonance branches f_{SF}, $f_{2^{\mathrm{nd}}\mathrm{easy}}$ and f_{hard} do not deviate for the different g-factors. Fitting the recorded resonance features by means of an anisotropic g-factor does not provide a better description of the experimental data.

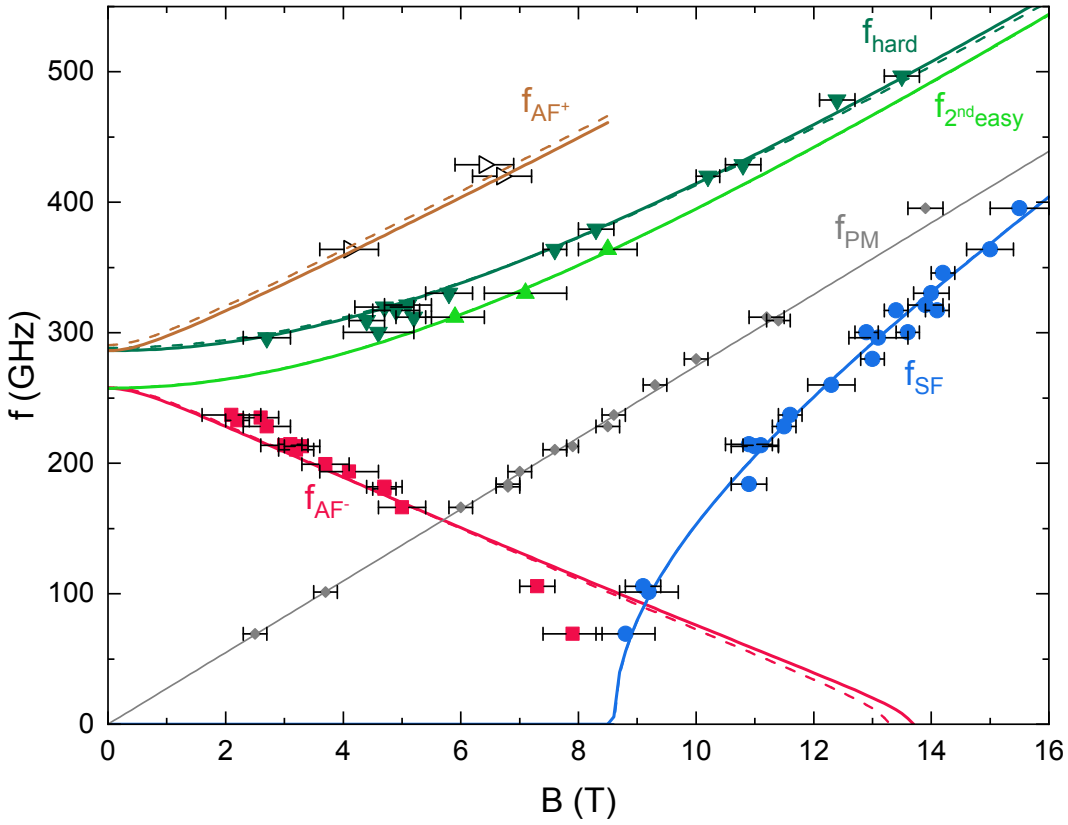


Figure A.2: Model 3: Frequency vs. field diagram of $Sr_2Ni(SeO_3)_2Cl_2$ constructed from HF-ESR data recorded at $T = 2\,\mathrm{K}$. Assuming a two-sublattice AFM with uniaxial anisotropy, the observed branches were attributed to f_{AF^-}, f_{SF} and $f_{\perp}$. The branch f_{AF^+} is a computation from obtained fit parameters while f_{PM} describes a paramagnetic impurity in the sample.

B Bibliography

[1] A. N. Vasiliev et al. *Low-Dimensional Magnetism*. CRC Press, 2019.

[2] JP Renard, LP Regnault, and M Verdaguer. *Magnetism: Molecules to Materials I - Models and Experiments*. Wiley-VCH, 2001.

[3] Daniel I Khomskii. *Basic aspects of the quantum theory of solids: order and elementary excitations*. Cambridge university press, 2010.

[4] Alexander Vasiliev et al. "Milestones of low-D quantum magnetism". In: *npj Quantum Materials* 3.1 (2018), pp. 1–13.

[5] Martin W Zwierlein et al. "Direct observation of the superfluid phase transition in ultracold Fermi gases". In: *nature* 442.7098 (2006), pp. 54–58.

[6] Jinsheng Wen et al. "Experimental identification of quantum spin liquids". In: *npj Quantum Materials* 4.1 (2019), pp. 1–9.

[7] F. D. M. Haldane. "Nonlinear Field Theory of Large-Spin Heisenberg Antiferromagnets: Semiclassically Quantized Solitons of the One-Dimensional Easy-Axis Néel State". In: *Phys. Rev. Lett.* 50 (15 Apr. 1983), pp. 1153–1156. DOI: 10.1103/PhysRevLett.50.1153.

[8] The Nobel Prize. *MS Windows NT Kernel Description*. 2016. URL: https://www.nobelprize.org/prizes/physics/2016/summary/ (visited on 06/20/2022).

[9] J. P Renard et al. "Presumption for a Quantum Energy Gap in the Quasi-One-Dimensional $S = 1$ Heisenberg Antiferromagnet $Ni(C_2H_8N_2)_2NO_2(ClO_4)$". In: *Europhysics Letters (EPL)* 3.8 (Apr. 1987), pp. 945–952. DOI: 10.1209/0295-5075/3/8/013.

[10] E. S. Kozlyakova et al. "Quasi-1D XY antiferromagnet $Sr_2Ni(SeO_3)_2Cl_2$ at Sakai-Takahashi phase diagram". In: *Scientific Reports* 11.1 (2021), pp. 1–8. DOI: 10.1038/s41598-021-94390-3.

[11] Patrik Fazekas. *Lecture notes on electron correlation and magnetism*. Vol. 5. World scientific, 1999.

[12] Daniel Khomskii. *Transition metal compounds*. Cambridge University Press, 2014.

[13] Ferdinand Lipps. "Electron spins in reduced dimensions: ESR spectroscopy on semiconductor heterostructures and spin chain compounds". PhD thesis. Dresden, Technische Universität Dresden, Diss., 2011, 2011.

[14] A. U. B. Wolter et al. "Magnetic properties and exchange integrals of the frustrated chain cuprate linarite $PbCuSO_4(OH)_2$". In: *Phys. Rev. B* 85 (1 Jan. 2012), p. 014407. DOI: 10.1103/PhysRevB.85.014407.

[15] Sergio M Rezende, Antonio Azevedo, and Roberto L Rodríguez-Suárez. "Introduction to antiferromagnetic magnons". In: *Journal of Applied Physics* 126.15 (2019), p. 151101.

[16] Jamie Brambleby et al. "Combining microscopic and macroscopic probes to untangle the single-ion anisotropy and exchange energies in an $S = 1$ quantum antiferromagnet". In: *Phys. Rev. B* 95 (13 Apr. 2017), p. 134435. DOI: 10.1103/PhysRevB.95.134435.

[17] Anatole Abragam and Brebis Bleaney. *Electron paramagnetic resonance of transition ions*. Oxford University Press, 2012.

[18] Stephen Blundell. *Magnetism in condensed matter*. 2003.

[19] Charles P Poole. *Electron spin resonance: a comprehensive treatise on experimental techniques*. Courier Corporation, 1996.

[20] Norberto Majlis. *The Quantum Theory Of Magnetism*. World Scientific Publishing Company, 2007.

[21] Claude Berthier, Laurent P Levy, et al. "High Magnetic Fields: Applications in Condensed Matter Physics and Spectroscopy". In: (2001).

[22] George Edward Pake, Thomas Leo Estle, et al. *Physical principles of electron paramagnetic resonance*. Mass., WA Benjamin, Advanced Book Program, 1973.

[23] Alessandro Bencini and Dante Gatteschi. *EPR of exchange coupled systems*. Courier Corporation, 2012.

[24] Sam Mugiraneza and Alannah M Hallas. "Tutorial: a beginner's guide to interpreting magnetic susceptibility data with the Curie-Weiss law". In: *Communications Physics* 5.1 (2022), pp. 1–12.

[25] Y. Iwasaki et al. "Effective $S = 2$ antiferromagnetic spin chain in the salt (o-MePy-V)$FeCl_4$". In: *Phys. Rev. B* 97 (8 Feb. 2018), p. 085113. DOI: 10.1103/PhysRevB.97.085113.

[26] Masashi Hase, Masayuki Hagiwara, and Koichi Katsumata. "Observation of an antiferromagnetic resonance in the spin-Peierls compound $CuGeO_3$ doped with Zn". In: *Phys. Rev. B* 54 (6 Aug. 1996), R3722–R3725. DOI: 10.1103/PhysRevB.54.R3722.

[27] Lena Spillecke. "High-frequency/ High-field Electron Paramagnetic Resonance Investigations on Metal-Organic Molecular Compounds". PhD thesis. Heidelberg, Ruprecht Karls Universität Heidelberg, Diss., 2021, 2021.

[28] Neil W Ashcroft, N David Mermin, et al. *Solid state physics*. 1976.

[29] Koichi Momma and Fujio Izumi. "*VESTA3* for three-dimensional visualization of crystal, volumetric and morphology data". In: *Journal of Applied Crystallography* 44.6 (Dec. 2011), pp. 1272–1276. DOI: 10.1107/S0021889811038970.

[30] J. Krzystek, Andrew Ozarowski, and Joshua Telser. "Multi-frequency, high-field EPR as a powerful tool to accurately determine zero-field splitting in high-spin transition metal coordination complexes". In: *Coordination Chemistry Reviews* 250.17 (2006). 20th International Conference on Coordination and Bioinorganic Chemistry, pp. 2308–2324. ISSN: 0010-8545. DOI: https://doi.org/10.1016/j.ccr.2006.03.016.

[31] Gordon A. Bain and John F. Berry. "Diamagnetic Corrections and Pascal's Constants". In: *Journal of Chemical Education* 85.4 (2008), p. 532. DOI: 10.1021/ed085p532.

[32] George Rado. *Magnetism V1*. Vol. 1. Elsevier, 2012.

[33] Johannes Werner. "Experimentelle Untersuchungen der Magnetisierung und der Elektronenspinresonanz an Übergansgsmetallverbindungen mit konkurrierenden Wechselwirkungen". PhD thesis. Heidelberg, Ruprecht-Karls-Universität Heidelberg, Diss., 2019, 2019.

[34] Takeo Nagamiya. "Theory of Antiferromagnetism and Antiferromagnetic Resonance Absorption, I". In: *Progress of Theoretical Physics* 6.3 (June 1951), pp. 342–349. ISSN: 0033-068X. DOI: 10.1143/ptp/6.3.342.

[35] F. Keffer and C. Kittel. "Theory of Antiferromagnetic Resonance". In: *Phys. Rev.* 85 (2 Jan. 1952), pp. 329–337. DOI: 10.1103/PhysRev.85.329.

[36] J. Werner et al. "Anisotropy-governed competition of magnetic phases in the honeycomb quantum magnet $Na_3Ni_2SbO_6$ studied by dilatometry and high-frequency ESR". In: *Phys. Rev. B* 95 (21 June 2017), p. 214414. DOI: 10.1103/PhysRevB.95.214414.

[37] K. Dey et al. "Magnetic phase diagram and magnetoelastic coupling of $NiTiO_3$". In: *Phys. Rev. B* 101 (19 May 2020), p. 195122. DOI: 10.1103/PhysRevB.101.195122.

[38] Shin-ichi Shinozaki et al. "Antiferromagnetic order in single crystals of the $S = 2$ quasi-one-dimensional chain $MnCl_3$(bpy)". In: *Phys. Rev. B* 93 (1 Jan. 2016), p. 014407. DOI: 10.1103/PhysRevB.93.014407.

[39] A. I. Kurbakov et al. "Zigzag spin structure in layered honeycomb $Li_3Ni_2SbO_6$: A combined diffraction and antiferromagnetic resonance study". In: *Phys. Rev. B* 96 (2 July 2017), p. 024417. DOI: 10.1103/PhysRevB.96.024417.

[40] Changhyun Koo et al. "Static and Dynamic Magnetic Response of Fragmented Haldane-like Spin Chains in Layered $Li_3Cu_2SbO_6$". In: *Journal of the Physical Society of Japan* 85.8 (2016), p. 084702. DOI: 10.7566/JPSJ.85.084702.

[41] J. Werner et al. "Magnetic anisotropy and the phase diagram of chiral $MnSb_2O_6$". In: *Phys. Rev. B* 94 (10 Sept. 2016), p. 104408. DOI: 10.1103/PhysRevB.94.104408.

[42] E. Schulze et al. "EPR studies of the triangular-lattice antiferromagnet Cs_2CuBr_4". In: *Low Temperature Physics* 43.11 (2017), pp. 1311–1314. DOI: 10.1063/1.5010318.

[43] M. M. Markina. private correspondence.

[44] S. K. Gotovko et al. "Electron spin resonance in spiral antiferromagnet linarite: Theory and experiment". In: *Phys. Rev. B* 100 (17 Nov. 2019), p. 174412. DOI: 10.1103/PhysRevB.100.174412.

[45] A.N. Vasiliev. private correspondence.

[46] D. Knauer. private correspondence.

[47] Leon Balents. "Spin liquids in frustrated magnets". In: *Nature* 464.7286 (2010), pp. 199–208.

[48] Janhavi P Joshi and SV Bhat. "On the analysis of broad Dysonian electron paramagnetic resonance spectra". In: *Journal of Magnetic Resonance* 168.2 (2004), pp. 284–287.

[49] F. Theuss. "Mixed Spin-Chains in $ACuFe_2(VO_4)_3$ (A=Na, Li) studied by Electron Spin Resonance and Static Magnetization". MA thesis. University of Heidelberg, 2019.

[50] E. A. Zvereva et al. "Zigzag antiferromagnetic quantum ground state in monoclinic honeycomb lattice antimonates $A_3Ni_2SbO_6$ (A = Li, Na)". In: *Phys. Rev. B* 92 (14 Oct. 2015), p. 144401. DOI: 10.1103/PhysRevB.92.144401.

[51] Melvin Linzer. "Line Parameters of Lorentzian Curves Containing Arbitrary Mixtures of Absorption and Dispersion". In: *Journal of Applied Physics* 40.1 (1969), pp. 372–376.

[52] Chen Sun and Nikolai A Sinitsyn. "Exact transition probabilities for a linear sweep through a Kramers-Kronig resonance". In: *Journal of Physics A: Mathematical and Theoretical* 48.50 (2015), p. 505202.

[53] V. A. Ivanshin et al. "ESR study in lightly doped $La_{1-x}Sr_xMnO_3$". In: *Phys. Rev. B* 61 (9 Mar. 2000), pp. 6213–6219. DOI: 10.1103/PhysRevB.61.6213.

Erklärung:

Ich versichere, dass ich diese Arbeit selbstständig verfasst habe und keine anderen als die angegebenen Quellen und Hilfsmittel benutzt habe.

Heidelberg, den 01.07.2022 ..... Paula Felk .....

Acknowledgments

At the end of my thesis I would like to thank everyone who made this project possible and supported me during the 12 months of work.

First of all, I would like to particularly thank Prof. Dr. Rüdiger Klingeler for giving me the opportunity to carry out my Master's thesis in his research group. His open-door policy and many discussions without time pressure introduced me to scientific working in a friendly and social atmosphere. He was always available to answer my questions and gave me new ideas on how to proceed my research. Furthermore, I would like to thank Prof. Dr. Maurits Haverkort for agreeing to be the second supervisor of this thesis.

A special thank you goes to Martin Jonák who guided me through my first measurements and provided me with the required background knowledge to understand my experimental results. I enjoyed the countless scientific and philosophic discussions during our evening snack breaks (standing on the balcony to get some change of pace from sitting too much).

I would like to thank my office mate Dr. Changhyun Koo who was always ready to answer any kind of questions that popped into my head. Moreover, I would like to thank him for turning on the air conditioner during the summer months so that I could enter a nicely cooled room and start working productively right away.

Furthermore, a note of gratitude goes to Jan, Lukas, Rahel, Kevin and Ahmed for the pleasant lunch breaks and 5 p.m. bakery happy hour with conversations about sometimes physics but even more often non-physical topics. Moreover, I would like to thank all the present and former members of F25 for the friendly and helpful atmosphere they created.

At last, I thank my friends and especially my family who supported me throughout my whole studies. They always managed to cheer me up when I needed diversion from a busy work day and helped me to gain new energy.